^{77}Se Nuclear Magnetic Resonance Study of the Topological Insulator Bi$_2$Se$_3$

Von der Fakultät für Physik und Geowissenschaften
der Universität Leipzig
genehmigte

DISSERTATION

zur Erlangung des akademischen Grades

doctor rerum naturalium
(Dr. rer. nat.)

vorgelegt

von M.Sc. Nataliya M. Georgieva
geboren am 30.11.1986 in Razlog, Bulgarien

Gutachter: Prof. Dr. Jürgen Haase
            Prof. Dr. Jürgen Senker

Tag der Verleihung: 18.11.2019

Bibliographische Beschreibung

Georgieva, Nataliya Metodieva

[77]Se Nuclear Magnetic Resonance Study of the Topological Insulator Bi_2Se_3

Universität Leipzig, Dissertation

87 S.*, 66 Lit.*, 31 Abb., 10 Tab., 7 Anlagen.

Referat

Topologische Isolatoren stellen eine neue Materialklasse dar, die sich insbesondere durch eine isolierende Bandlücke im Inneren und gleichzeitig leitenden elektronischen Zuständen an der Oberfläche auszeichnet. Die als thermoelektrischer Halbleiter bekannte Verbindung Bi_2Se_3 wurde vor einem Jahrzehnt als Mustersystem eines topologischen Isolators identifiziert. Die vorliegende Arbeit ist eine Studie zur kernmagnetischen Resonanz (NMR) am Selenisotop [77]Se in $Cu_xBi_2Se_3$-Einkristallen $(0{,}00 \leq x \leq 0{,}17)$, Bi_2Se_3-Pulver und nanometergroßen Bi_2Se_3-Teilchen. Erstmals können zwei Se-Signale unterschieden und eindeutig den beiden chemisch ungleichen Gitterpositionen von Se zugeordnet werden. Eine unerwartet starke, durch Elektronen vermittelte, indirekte Kopplung zwischen den Atomkernen wird anhand großer, feldunabhängiger Linienbreiten postuliert. Die gemessenen ungewöhnlichen Spin-Echo-Zerfälle sind vermutlich eine mittelbare Folge davon. Während bei dem Pulver das Spektrum und die longitudinale Relaxation mit den Einkristalldaten übereinstimmen, wurden bei den Nanoteilchen Signale mit zwei- bis achtmal schnellerer longitudinaler Relaxation separiert. Einfache Modelle werden diskutiert, zum Verständnis der Daten in diesen Systemen mit starker Spin-Bahn-Kopplung, die bis heute kaum mittels NMR verstanden sind.

Abstract

Topological insulators are a novel class of materials characterized by an insulating bulk and simultaneous metallic electronic surface states. A decade ago, Bi_2Se_3 – a well-known thermoelectric semiconductor – was identified as a model topological insulator. This thesis presents a thorough nuclear magnetic resonance (NMR) study of [77]Se in $Cu_xBi_2Se_3$ $(0.00 \leq x \leq 0.17)$ single crystals, bulk Bi_2Se_3 powder, and nanometer-sized Bi_2Se_3 particles. For the first time, two Se signals could be identified and unambiguously assigned to the two inequivalent Se sites expected from the chemical structure. An unexpectedly strong electron-mediated indirect internuclear coupling is postulated based on the large field-independent NMR linewidths. The measured peculiar spin-echo decays are most likely a mediate consequence of it. For the bulk powder, the spectrum and longitudinal relaxation were found to agree with the single crystal data; but for the nanoparticles, signals with two- to eight-times faster longitudinal relaxation could be distinguished. Simple models are developed to discuss the results in these strongly spin-orbit coupled systems, for which a general NMR understanding is still missing.

---

*   ... S. (Seitenzahl insgesamt)

   ... Lit. (Anzahl der im Literaturverzeichnis ausgewiesenen Literaturangaben)

Contents

List of abbreviations

2D, 3D	two-dimensional, three-dimensional
AC	alternating current
ARPES	angle-resolved photoemission spectroscopy
BM	ball-milled
CW	continuous wave
EPR	electron paramagnetic resonance
FC	field-cooling
FID	free induction decay
MAS	magic angle spinning
MBE	molecular beam epitaxy
MG	mortar-ground
NMR	nuclear magnetic resonance
ppm	parts per million
PPMS	physical property measurement system
PXRD	powder X-ray diffraction
Q-factor	quality factor
QL	quintuple layer
SNR	signal-to-noise ratio
SOC	spin-orbit coupling
STM	scanning tunneling microscopy
TEM	transmission electron microscopy
TI	topological insulator
TSS	topological surface states
XRD	X-ray diffraction
ZFC	zero-field-cooling

Chapter 1

Introduction

Topological phases of matter constitute a type of order in condensed matter physics, rather distinct from the conventional order types described in terms of symmetry breaking [Has11]. Their realization in real materials and at ambient conditions has induced a huge interest in the solid state physics community over the past decade [Fen12; Fu07b; Has10; Qi11; Sán16]. Three-dimensional topological insulators (3D TIs) have been predicted and experimentally proven in conventional materials, which have inverted band structures due to spin-orbit coupling [And13]. The nontrivial topology of bulk electronic wavefunctions leads to the characteristic feature of 3D TIs: the existence of gapless topological surface states (TSS) in the presence of a bulk band gap. These special metallic TSS, consisting of an odd number of massless Dirac cones, have unusual properties like spin-momentum locking and robustness to nonmagnetic disorder, hence promising potential applications in spintronics [Has11].

The Bi_2Se_3 class of 3D TIs, i.e., Bi_2Se_3, Bi_2Te_3, and Sb_2Te_3, has attracted a lot of attention for being stoichiometric materials, easy to synthesize as single crystals and having the simplest possible surface states (single Dirac cone) [And13]. Among them, Bi_2Se_3 stands out by a nearly idealized Dirac cone and a large bulk band gap of $0.3\,eV$, and is therefore considered a model system. In reality, Bi_2Se_3 tends to form natural defects, mainly Se vacancies acting as electron donors and thereby making the bulk of the material conducting. Intercalation of Cu atoms into the system raises the charge carrier density further and moreover, leads to superconductivity at low temperatures [Fra13]. This effect is potentially interesting since the interface between a TI and a superconductor is expected to host Majorana fermions, the controllable realization of which would start a revolution in quantum computing [Son17]. A short historical review on 3D TIs and a closer look at the properties of Bi_2Se_3 and Bi_2Te_3, mostly determined from angle-resolved photoemission spectroscopy (ARPES), scanning tunneling microscopy (STM) and transport measurements, is given in Chapter 2.

In this thesis a different experimental approach to the electronic properties of 3D TIs is considered: nuclear magnetic resonance (NMR) spectroscopy. NMR is a valuable method for probing the electronic and chemical properties of materials locally. NMR parameters like frequency shift, linewidth, longitudinal and transversal relaxation times can be sensitive to the electronic and nuclear surrounding and give us clues of what happens in the bulk of materials. Requisite NMR concepts are introduced in Chapter 3. Signals from different regions in the sample, e.g., surface and bulk, can be observed, given that the number of nuclei in each region is sufficiently large. Moreover, NMR can be applied at ambient

conditions and on samples of various shapes and purity, in contrast to the surface-sensitive techniques ARPES and STM.

At the start of this research work we put the question: What can we learn about the bulk and surface electronic properties of 3D TIs by studying the model compound Bi_2Se_3 with NMR? In particular, the following issues had to be addressed.

1. Understand the bulk by performing the first ^{77}Se NMR of Bi_2Se_3 single crystals with different Cu- (and hence electron) doping.

2. Subsequently search for surface ^{77}Se NMR signals in a sample having increased surface-to-volume ratio.

While at the beginning of this work (end of 2011) there were no literature sources on NMR of 3D TIs, meanwhile several studies have been published. A detailed review on NMR of Bi_2Se_3 and Bi_2Te_3 can be found in Chapter 4. Here we summarize briefly some main findings and open questions. From 2012 to 2015 there have been four reports on ^{125}Te NMR of Bi_2Te_3 [Kou13; Kou14; Pod15; Tay12], four on ^{209}Bi NMR of Bi_2Se_3 [Muk15; Nis13; Nis14; You12] and one reported study on ^{77}Se NMR of Bi_2Se_3 powder [Tay12]. While all of these show that NMR longitudinal relaxation reflects the conductivity of the bulk, they leave many questions unanswered. For example, two inequivalent selenium (tellurium) sites in the crystal lattice should give rise to two distinct ^{77}Se (^{125}Te) NMR signals. These, however, have not been resolved or discussed, while signals have been ascribed to surface nuclei. Furthermore, on the ^{209}Bi NMR side special lineshapes, spin echo decays, and angular dependent intensities are not understood. Some of these issues could be solved within this thesis, parts of which have been published in 2016 [Geo16] (some statements from the publication have been duplicated here where appropriate). Two important findings of this report on ^{77}Se NMR of bulk Bi_2Se_3 samples are (i) the unambiguous assignment of signals due to distinct selenium sites and (ii) the discovery of an unexpectedly strong indirect internuclear coupling mediated by electrons. The latter finding, together with quadrupolar effects, is the likely reason for the peculiar ^{209}Bi NMR results. Two ensuing $^{77}Se/^{125}Te$ NMR studies have also attributed signals to distinct Se/Te sites [Ant17a; Mat16]. None of these experimental studies offers, however, an understanding of the different contributions to the measured frequency shift. Only recently, a tight-binding calculation of various, carrier-density dependent contributions to the NMR shift in bulk Bi_2Se_3 and Bi_2Te_3 [Bou16] has shown that these shifts are site specific and rather nontrivial. Much more experimental work is needed to verify the theoretical understanding.

Results from our research work are considered in the last two chapters of this thesis. In Chapter 5 our aforementioned published ^{77}Se NMR results are presented in detail, together with unpublished data on various $Cu_xBi_2Se_3$ single crystals. The results are moreover being discussed in the context of theoretical predictions and conclusions drawn from experiments in the literature.

With the created understanding of the bulk NMR, a foundation for studying TSS with NMR has been set. Chapter 6 describes an attempt in this direction, for which a nanocrystalline Bi_2Se_3 powder sample has been produced and studied with ^{77}Se NMR in comparison to bulk Bi_2Se_3 powder. Significant differences in the spectrum and longitudinal relaxation time point to the existence of a fast-relaxing species of ^{77}Se nuclei in the sample with increased surface-to-volume ratio. Although we were able to estimate that up to 80% of all nuclei are fast-relaxing, it remains an open question whether this is due to surface states, altered bulk band structure, or crystal deformation upon milling of the sample.

Chapter 2

Three-dimensional topological insulators

A three-dimensional (3D) topological insulator (TI) has its bulk band gapped at the Fermi level but exhibits gapless topological surface states (TSS) at all of its surfaces [Fu07b]. The surface bands in momentum space consist of two-dimensional (2D) Dirac cones [Fra13], cf. Fig. 2.1. Here we consider only strong 3D TIs, i.e., materials with an odd number of Dirac cones, according to the topological classification of time-reversal symmetry [Has10].
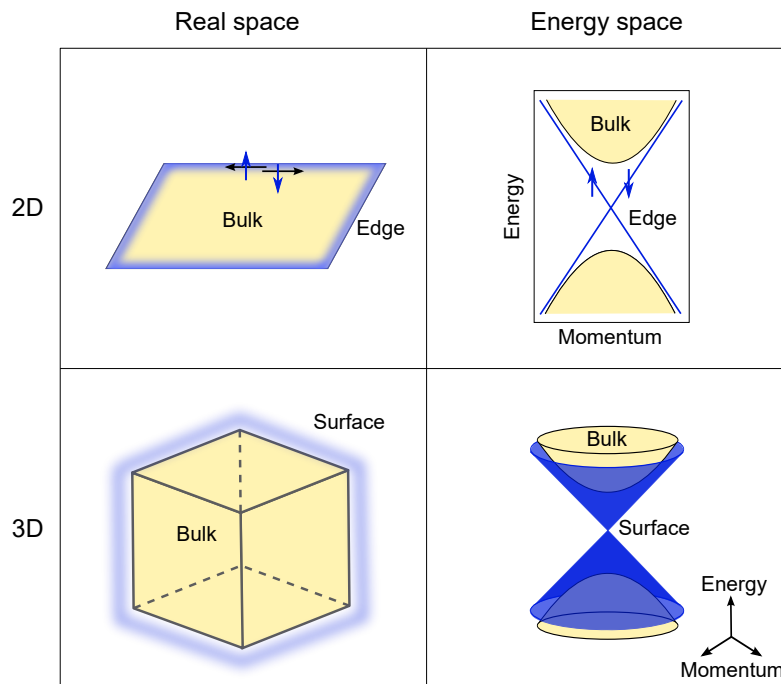

Figure 2.1: One-dimensional edge (top) and two-dimensional surface states (bottom) of a 2D and a 3D topological insulator, respectively, and the corresponding energy dispersions.

2.1 Early discoveries

The $Bi_{1-x}Sb_x$ alloy with x between ~ 0.07 and ~ 0.22 is the first strong 3D TI material to be theoretically proposed [Fu07a] and experimentally proven [Hsi08]. However, this material has rather complex TSS and a small bulk band gap ($< 100\,\mathrm{meV}$). Moreover, the random distribution of Bi and Sb atoms significantly reduces the electron mobility. Soon after the discovery of $Bi_{1-x}Sb_x$, the family of stoichiometric crystals Bi_2Se_3, Bi_2Te_3, and Sb_2Te_3 was identified as a new family of 3D TI materials and proven to be superior for having ordered lattice structures, relatively large bulk gaps, and surface states composed of only a single Dirac cone [Fra13]. These materials furthermore attract lasting scientific interest with their very promising thermoelectric properties [She17; Sun15; Zha15]. For more detailed information the reader is referred to the textbook [Fra13].

2.2 Model systems Bi_2Se_3 and Bi_2Te_3

Bi_2Se_3 and Bi_2Te_3 were suggested to be 3D TIs with a single Dirac cone in 2009 by Zhang et al. [Zha09], cf. Fig. 2.2 for the calculated bulk and surface energy dispersions. Strong spin-orbit coupling (SOC) is responsible for the band inversion at the Γ point in these materials [Fra13]. Soon after the theoretical prediction, angle-resolved photoemission spectroscopy (ARPES) measurements showed that Bi_2Se_3 and Bi_2Te_3 crystals indeed exhibit TSS at the Γ point in the bulk band gap [Che09; Xia09]. Among them, Bi_2Se_3 is considered to be the most promising for applications, for having the larger band gap of $0.3\,\mathrm{eV}$ (much larger than room temperature) [She18].

Both, Bi_2Se_3 and Bi_2Te_3, have the same rhombohedral crystal structure with space group $D_{3d}^5(R\bar{3}m)$ with five atoms in one unit cell. Figure 2.3 depicts the crystal structure of Bi_2Se_3. It consists of stacked, van der Waals bonded quintuple layers (QLs) of five atomic sheets each, with the c-axis normal to the layers. Each QL contains two equivalent "outer" Se atoms (Se_{out}), two equivalent Bi atoms, and another "inner" Se atom (Se_{in}) located at the center of inversion (the unit cell comprises 3 QL) [Zha09].

While the surface sensitive techniques ARPES and scanning tunneling microscopy (STM) have contributed a great deal to testing and confirming the theoretical predictions for

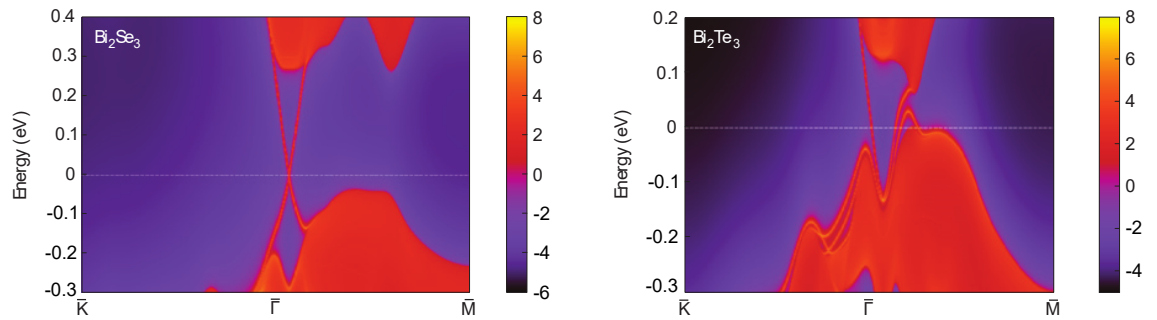**Figure 2.2:** Calculated energy and momentum dependence of the local density of states on the [111] surface for Bi_2Se_3 (left) and Bi_2Te_3 (right). The warmer colors represent higher local density of states. The dashed white line represents the Fermi energy level in undoped Bi_2Se_3 and Bi_2Te_3. The surface states span the bulk band gap in the vicinity of the Γ point (from Ref. [Zha09]).
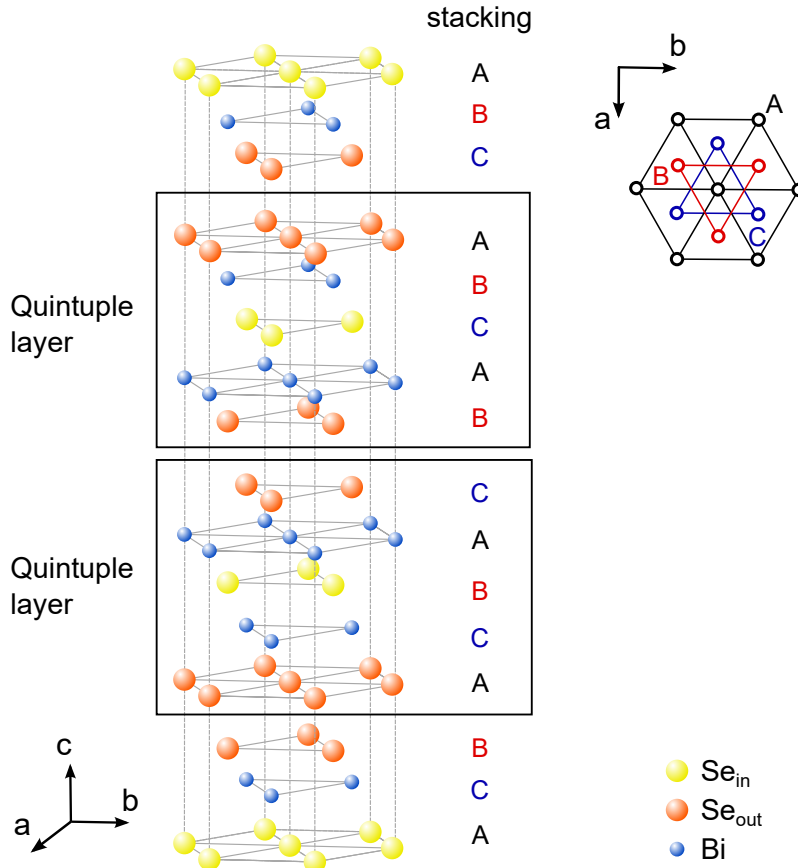
Figure 2.3: Crystal structure of Bi_2Se_3.

Bi_2Se_3 and Bi_2Te_3 (e.g., the existence of a single Dirac cone, the observed left-handed helical spin texture of the massless Dirac fermion, and the confirmation of absence of backscattering for time-reversal invariant impurities), the transport properties of the TSS in these two materials are much harder to extract, due to the large residual bulk carriers and sample quality [Fra13]. Bi_2Se_3 is naturally electron-doped due to Se vacancies, and Bi_2Te_3 is either n- or p-type due to Bi-Te antisite defects.

Typical charge carrier densities of Bi_2Se_3 are 2×10^{17} to 2×10^{19} cm^{-3} [Ana10; Hor09; Nis13; Wan10] with the Fermi level lying in the bulk conduction band [Fra13]. By intercalating Cu atoms in the van der Waals gaps of Bi_2Se_3, the bulk charge carrier density can be further increased to $\sim 10^{20}$ cm^{-3}. Very surprisingly, the electron density of $Cu_xBi_2Se_3$ was found to be almost independent of the intercalated Cu concentration x (in the range 0.09-0.64) [Fra13]. For $Cu_xBi_2Se_3$ with Cu doping levels of x$\approx$0.09-0.64, a superconducting phase has been observed with T_c varying from $\sim$3.8 K at x = 0.12 down to $\sim$2.2 K at x$\approx$0.64 [Fra13]. Magnetization and transport measurements have identified $Cu_xBi_2Se_3$ as a type-II superconductor with $B_{c1} \approx 0.4$ mT and $B_{c2} \approx 1.7$ T (3-4.6 T) for fields parallel (perpendicular) to the c-axis of the crystal [Fra13]. Moreover, $Cu_xBi_2Se_3$ might be a topological superconductor [Fu10].

Decreasing the bulk charge carrier density of Bi_2Se_3 has been achieved by chemical doping (e.g., with Ca^{2+} or Sb^{3+} substituting for Bi^{3+}), by optimizing the growth conditions (Se-enrichment), and by molecular beam epitaxy (MBE) growth of high-quality thin films

[And13]. MBE-grown Bi_2Se_3 thin films with reduced carrier density and increased mobility have been recently reported by Wang et al. [Wan18]. For Bi_2Te_3 "it is difficult to obtain samples with low n" [And13].

2.3 Other 3D TI materials

A huge computational and experimental effort has been put into the search for new and better 3D TIs in the past decade. Here, some of the found systems will be mentioned, without claiming completeness.

For a review on topological insulator materials discovered before May 2013, see the references [And13] and [Fra13]. Among them, the ternary materials Bi_2Te_2Se [Ren10] and $TlBiX_3$ (X = Te/Se) should be mentioned.

Some more recent reports on topological insulators with improved bulk insulating behavior will be named here. In 2016 Lee et al. [Lee16] reported on highly crystalline Sb_2Te_2Se single crystals being a robust p-type semiconductor with an isolated Dirac cone.

A bulk insulator TI, having a surface state Dirac point energy well isolated from the bulk valence and conduction bands, displaying quantum oscillations from the surface state electrons, which can be grown as large, high-quality bulk single crystals was found in lightly Sn-doped $Bi_{1.1}Sb_{0.9}Te_2S$ grown by the vertical Bridgman method by Kushwaha et al. [Kus16].

Another prominent bulk insulating topological insulator is $(Bi_{1-x}Sb_x)_2Te_3$ [Urk17], for which proper tuning of the concentration x allowed the observation of the surface quantum Hall effect [Yos15].

A bulk insulating state was achieved also by optimizing the composition of the 3D TI $Pb(Bi_{1-x}Sb_x)_2Te_4$ in [Hat17], showing a n- to p-type transition in bulk conduction at x ≈ 0.80.

Recently, new 3D TI classes have been predicted in the double perovskites A_2TePoO_6 (A = Ca, Sr, Ba) [Lee17] and A_2BiXO_6 (A = Ca, Sr, Ba; X = Br, I) [Pi17] with bulk band gaps up to $0.4\,eV$ and $0.55\,eV$, respectively, however, no experimental evidence is currently known to the author.

Chapter 3

NMR concepts

In this chapter some necessary concepts of nuclear magnetic resonance (NMR) in solids will be described. For a deeper understanding of the physics behind NMR and its technical realization, the reader is referred to the books of Abragam [Abr61] and Slichter [Sli10].

3.1 Nuclear spin in a magnetic field

Nuclear magnetic resonance makes use of the property of many nuclei to possess a nonzero spin quantum number I[1]. Such nuclei have a magnetic moment

$$\boldsymbol{\mu} = \gamma \, \boldsymbol{\mathfrak{J}} \tag{3.1}$$

aligned with the spin angular momentum $\boldsymbol{\mathfrak{J}}$. The nucleus-specific constant γ is called the gyromagnetic ratio. A magnetic field $\boldsymbol{B_0}$ produces a torque on the magnetic moment $\boldsymbol{\mu}$, and due to the corresponding angular momentum $\boldsymbol{\mathfrak{J}}$, the nuclear spin will not align to the magnetic field direction like a compass needle, but will rather precess around it like a gyroscope. The equation of motion is obtained by setting the torque equal to the rate of change of angular momentum

$$\frac{\mathrm{d}\boldsymbol{\mathfrak{J}}}{\mathrm{d}t} = \boldsymbol{\mu} \times \boldsymbol{B_0}. \tag{3.2}$$

Substituting for $\boldsymbol{\mathfrak{J}}$ one obtains the equation of motion of the magnetic moment

$$\frac{\mathrm{d}\boldsymbol{\mu}}{\mathrm{d}t} = \boldsymbol{\mu} \times \gamma \boldsymbol{B_0}. \tag{3.3}$$

The angular frequency of this precession is $\omega_0 = \gamma B_0$ and is called the Larmor frequency.

In a quantum mechanical description $\boldsymbol{\mu}$ and $\boldsymbol{\mathfrak{J}}$ are operators and the interaction of the magnetic moment and the magnetic field is described by the Zeeman Hamiltonian

$$\mathcal{H}_{\mathrm{Z}} = -\boldsymbol{\mu} \cdot \boldsymbol{B_0} = -\gamma \, \boldsymbol{\mathfrak{J}} \cdot \boldsymbol{B_0} = -\gamma \hbar I_z B_0. \tag{3.4}$$

Here we have assumed that the magnetic field is applied along the z-axis and have introduced the dimensionless spin operator $\boldsymbol{I} = \boldsymbol{\mathfrak{J}}/\hbar$. The eigenvalues of this Hamiltonian are the

---

1   The spin quantum number I can take integer or half-integer values ≥ 0.

energy levels

$$E_m = -\gamma\hbar B_0 m \tag{3.5}$$

with $m = I, I-1, ..., -I$ being the eigenvalues of the operator I_z. The Zeeman energy splitting of the levels is equal to $\gamma\hbar B_0 = \hbar\omega_0$. Interestingly, the angular frequency needed to induce transitions between neighboring energy levels is identical to the Larmor frequency of precession introduced above.

The quantum mechanical equation of motion of the magnetic moment $\boldsymbol{\mu}$ can be obtained by applying the Heisenberg equation to each of its components μ_j ($j = x,y,z$) and taking advantage of the commutation relations of the components of angular momentum I_j.

$$\frac{\mathrm{d}\boldsymbol{\mu}}{\mathrm{d}t} = \frac{i}{\hbar}[\mathcal{H}_\mathrm{Z},\boldsymbol{\mu}] = \boldsymbol{\mu} \times \gamma\boldsymbol{B_0}. \tag{3.6}$$

Note that this equation holds not only for static but also for time-dependent fields.

So far we have seen that a nuclear spin probes the local[1] magnetic field with its precession frequency. In order to gain information about it, we need to perturb the system so that transitions between the Zeeman levels are induced. Such interaction must be time-dependent, in order to conserve the energy of the system and has to have matrix elements connecting the energy levels. Commonly such a perturbation is created by an alternating field $\boldsymbol{B_1}(t) = \boldsymbol{B_1^0}\cos(\omega_1 t)$ applied perpendicular to the static one[2]. If we assume $\boldsymbol{B_1}$ parallel to the x-axis, then we get the perturbing Hamiltonian

$$\mathcal{H}_\mathrm{pert} = -\gamma\hbar I_x B_1^0 \cos(\omega_1 t). \tag{3.7}$$

It is proportional to I_x which has nonvanishing matrix elements $\langle m' \mid I_x \mid m \rangle$ only between levels with $m' = m \pm 1$.

3.2 Effect of an alternating magnetic field

Let us look at the effect of a linearly polarized alternating magnetic field applied along the x-axis $\boldsymbol{B_x}(t) = B_x\cos(\omega_1 t)\boldsymbol{e_x}$ on the nuclear magnetic moment. It is best to decompose it into two circularly polarized components $\boldsymbol{B_1^+}(t)$ and $\boldsymbol{B_1^-}(t)$ with opposite angular frequencies $+\omega_1$ and $-\omega_1$, respectively:

$$\boldsymbol{B_1^\pm}(t) = B_1\left(\cos(\pm\omega_1 t)\boldsymbol{e_x} + \sin(\pm\omega_1 t)\boldsymbol{e_y}\right) \tag{3.8}$$

$$\Rightarrow \boldsymbol{B_x}(t) = \boldsymbol{B_1^+}(t) + \boldsymbol{B_1^-}(t) = 2B_1\cos(\omega_1 t)\boldsymbol{e_x}. \tag{3.9}$$

---

1   In reality, a nuclear spin is not isolated and it will sense not only the applied magnetic field but also local fields due to surrounding nuclei and electrons.

2   Such an oscillating field is normally created by applying an alternating current to a coil wound around any direction having a component perpendicular to the direction of the static field.

The time evolution of the nuclear magnetic moment in the presence of both the alternating and the static field is given by the equation of motion

$$\frac{\mathrm{d}\boldsymbol{\mu}}{\mathrm{d}t} = \boldsymbol{\mu} \times \gamma \left[\boldsymbol{B_0} + \boldsymbol{B_1^{\pm}}(t) \right]. \tag{3.10}$$

We can remove the time dependence of the $\boldsymbol{B_1^{\pm}}$ by introducing a coordinate system rotating around the z-axis with $\pm\omega_1$. We denote it with a prime and choose its x'-axis along the $\boldsymbol{B_1^{\pm}}$ direction. The time derivatives of the magnetic moment in the rotating frame and in the laboratory frame are related as follows:

$$\left(\frac{\mathrm{d}\boldsymbol{\mu}}{\mathrm{d}t} \right)' = \frac{\mathrm{d}\boldsymbol{\mu}}{\mathrm{d}t} - (\pm\omega_1)\boldsymbol{e_z} \times \boldsymbol{\mu}. \tag{3.11}$$

Combining the equations (3.10) and (3.11) we obtain the equation of motion in the rotating frame

$$\left(\frac{\mathrm{d}\boldsymbol{\mu}}{\mathrm{d}t} \right)' = \boldsymbol{\mu} \times \gamma \left[\left(B_0 + \frac{\pm\omega_1}{\gamma} \right) \boldsymbol{e_z} + B_1 \boldsymbol{e_{x'}} \right]. \tag{3.12}$$

In the rotating frame, the magnetic moment experiences a static effective field with an x'-component of B_1 and a z-component of $B_0 \pm \omega_1/\gamma$. In the case of a positive γ, the z-component vanishes when the resonant condition $B_0 - \omega_1/\gamma = 0$ is fulfilled. In such case, the magnetic moment will precess around the x'-axis as long as B_1 is applied. Therefore, a magnetic moment originally aligned with the z-axis will rotate in the $y'z$-plane by an angle $\theta_{\mathrm{pulse}} = \gamma B_1 \tau_{\mathrm{pulse}}$ within a pulse duration τ_{pulse}. If $\theta_{\mathrm{pulse}} = \pi$ the magnetic moment will be inverted to the $-z$ direction and we have a so-called π-pulse. After a $\pi/2$-pulse ($\theta_{\mathrm{pulse}} = \pi/2$), on the other hand, the magnetic moment will precess in the $x'y'$-plane with the Larmor angular frequency $\omega_0 = \gamma B_0$. In most NMR experiments an alternating magnetic field is produced by a coil wound around an axis in the xy-plane. After a $\pi/2$-pulse is applied, the precession of magnetic moments in the xy-plane induces a measurable voltage in the same coil via Faraday induction.

3.3 Ensemble of spins

In real experiments, we deal of course not with a single nuclear spin, but with a sample containing an ensemble of spins, which are not isolated, but rather coupled with each other and with their surrounding. We will assume that the applied external field B_0 is always big enough so that the corresponding Zeeman interaction is the main Hamiltonian and the coupling Hamiltonians can be considered as perturbations. Let us first take a look at an ensemble of noninteracting spins, coupled to a thermal bath.

What we probe in an NMR experiment is the total magnetization of all nuclei, which is a sum of all expectation values of magnetic moments. For a system of N noninteracting spins in thermal equilibrium, the total magnetization $\boldsymbol{M}$ is aligned with the external field $\boldsymbol{B_0}$, i.e., $\boldsymbol{M} = M_{z0}\boldsymbol{e_z}$. Applying Boltzmann statistics one can calculate the z-component

of the magnetization as follows:

$$M_{z0} = N \langle \mu_z \rangle_{stat} = N \gamma \hbar \frac{\sum_{m=-I}^{I} m \exp(-E_m/k_B T)}{\sum_{m=-I}^{I} \exp\left(-E_m/k_B T\right)}. \tag{3.13}$$

Since the Zeeman energy is typically much smaller than the thermal energy, the high-temperature approximation is valid and equation (3.13) can be simplified to become the well known Curie formula

$$M_{z0} = \frac{N \hbar^2 \gamma^2 I(I+1) B_0}{3 k_B T}. \tag{3.14}$$

3.4 Longitudinal relaxation

After a pulse is applied to a spin system, the total magnetization is no longer parallel to the z-axis and the system is out of thermal equilibrium. Since the spin system is not isolated, it will give off the additional energy to some accepting agent and thereby relax back to thermal equilibrium with time. This process is called longitudinal relaxation and is typically an exponential process described by a characteristic longitudinal relaxation time T_1. The time dependence of the z-component of the magnetization can be derived from the Bloch equations and is given by

$$M_z(t) = M_{z0} \left(1 - q \exp\left(-t/T_1\right)\right), \tag{3.15}$$

where M_{z0} is the thermal equilibrium value defined in the previous section and q depends on the tipping angle of the pulse. In the case of a π-pulse ($\pi/2$-pulse), $q = 2$ ($q = 1$) and the z-magnetization immediately after the pulse, i.e., at $t = 0$, is equal to $-M_{z0}(0)$ - a so-called perfect inversion (saturation).

There are various mechanisms by which the spins can give off energy and come back to thermal equilibrium. Since spontaneous emission is very unlikely[1], spin transitions are mostly due to stimulated emission of energy. For that to occur, some fluctuating magnetic field at the precession frequency of the spin is needed[2]. Such magnetic field fluctuations can be caused by atomic movement in an anisotropic field, e.g., lattice vibrations in a crystal. Phonons, however, are quite inefficient in inducing nuclear spin transitions for having a much higher frequency than the Larmor frequency. Another, more effective, relaxation mechanism is the coupling of nuclear spins to electronic magnetic moments, e.g., dipole-dipole coupling to unpaired electronic spins in paramagnetic centers, or spins of itinerant electrons. A further, very effective, relaxation mechanism (leading to short relaxation times) is the hyperfine interaction between the nuclear spins and the spins of s-like itinerant electrons. Mostly, several mechanisms are present simultaneously, each having their own characteristic T_1 and temperature dependence.

---

[1] The probability for spontaneous emission is proportional to the third power of frequency and is hence insignificantly small at typical Zeeman level splittings (radio frequency range).

[2] In the case of quadrupolar nuclei with $I > 1/2$ transitions can also be induced by the interaction of a fluctuating electric field gradient with the nuclear electric quadrupole moment.

3.5 Transversal relaxation

So far, we have assumed that all nuclear spins in the ensemble feel the same static magnetic field and do not interact with each other. In reality, field inhomogeneities of the order of at least a few parts per million (ppm) are mostly present. Moreover, the local magnetic field at a nuclear site is modified due to couplings to the surrounding nuclei and electrons. The result is a distribution of local fields, and hence of Larmor frequencies, in the ensemble leading to a specific shape and width of the NMR line. Immediately after a $\pi/2$-pulse is applied, all spins in the ensemble are coherent and the transversal magnetization is maximal. However, with time, the distribution of local magnetic fields leads to dephasing of the spins and one measures a so-called free induction decay (FID) of the transversal magnetization. For short times (of the order of the decay constant) the FID can be mostly well described by an exponential decay function

$$g_{\mathrm{e}}(t) = \exp\left(-\frac{t}{T_2^*}\right) \tag{3.16}$$

or a Gaussian function

$$g_{\mathrm{G}}(t) = \exp\left(-\frac{t^2}{2T_{2\mathrm{G}}^{*\,2}}\right), \tag{3.17}$$

where T_2^* and $T_{2\mathrm{G}}^*$ are the corresponding decay constants. The NMR line $G(\omega)$ can be obtained by Fourier transforming the FID from the time domain into the frequency domain:

$$G(\omega) = \int_0 g(t)\cos\left(\omega t\right)\mathrm{d}t. \tag{3.18}$$

The Fourier transforms of $g_{\mathrm{e}}(t)$ and $g_G(t)$ are a Lorentzian

$$G_{\mathrm{L}}(\omega) = \frac{\frac{2}{T_2^*}}{\omega^2 + \left(\frac{1}{T_2^*}\right)^2} \tag{3.19}$$

and a Gaussian function of frequency

$$G_{\mathrm{G}}(\omega) = \sqrt{2\pi}T_{2\mathrm{G}}^* \exp\left(-\frac{T_{2\mathrm{G}}^{*2}\omega^2}{2}\right), \tag{3.20}$$

respectively.

3.5.1 Spin-spin interactions

Spin-spin interactions make a major contribution to the transversal relaxation of nuclear spins in solids. On one hand, the nuclear spins interact directly with each other via the dipole-dipole coupling of their magnetic moments. On the other hand, indirect internuclear coupling mediated by electrons can play a major role in some materials. We will deal with indirect internuclear couplings in bigger detail in Chapter 5 and will now consider the dipole-dipole coupling Hamiltonian.

Dipole-dipole coupling

The direct dipole-dipole coupling between two nuclear spins is always present and leads to a broadening of the NMR line. The dipolar coupling Hamiltonian for an ensemble of N nuclear spins is

$$\mathcal{H}_{\text{dip}} = \frac{\mu_0 \hbar^2}{8\pi} \sum_{i,j \neq i}^{N} \gamma_j \gamma_k \left[\frac{\boldsymbol{I}_i \cdot \boldsymbol{I}_j}{r_{ij}^3} - \frac{3(\boldsymbol{I}_i \cdot \boldsymbol{r}_{ij})(\boldsymbol{I}_j \cdot \boldsymbol{r}_{ij})}{r_{ij}^5} \right], \tag{3.21}$$

where $\boldsymbol{r}_{ij}$ is the vector connecting the positions of the nuclear spins $\boldsymbol{I}_i$ and $\boldsymbol{I}_j$ in the crystal lattice. The dipole-dipole-coupling-induced second moment of the NMR line of the nuclear spin species I_i has been computed by Van Vleck [Van48] for like spins (i.e., having the same γ):

$$\langle \Delta\omega^2 \rangle_i^{\text{like}} = \frac{3}{4}\gamma_i^4 \left(\frac{\mu_0}{4\pi}\right)^2 \hbar^2 I_i(I_i + 1) \sum_j \frac{\left(1 - 3\cos^2\theta_{ij}\right)^2}{r_{ij}^6}, \tag{3.22}$$

and for unlike spins (i.e., having different γs or significantly different precession frequencies[1]):

$$\langle \Delta\omega^2 \rangle_i^{\text{unlike}} = \frac{1}{3}\gamma_i^2 \gamma_j^2 \left(\frac{\mu_0}{4\pi}\right)^2 \hbar^2 I_j(I_j + 1) \sum_j \frac{\left(1 - 3\cos^2\theta_{ij}\right)^2}{r_{ij}^6}. \tag{3.23}$$

Here θ_{ij} is the angle between the vector $\boldsymbol{r}_{ij}$ connecting two spins and the magnetic field vector $\boldsymbol{B_0}$.

The second moment of a measured resonance curve described by a normalized function $G(\omega)$ can be computed by

$$\langle \Delta\omega^2 \rangle = \int \omega^2 G(\omega) \mathrm{d}\omega \tag{3.24}$$

and compared with the theoretical second moment due to dipole-dipole interaction (cf. Chap. 5).

Dipolar broadened lines can be narrowed by the method called magic angle spinning (MAS), where the sample is being rotated around a fixed axis. In this case the angular factor $1 - 3\cos^2\theta_{ij}$ in the second moment expressions above should be replaced by the time average

$$(1 - 3\cos^2\theta_{ij})_{\text{avg}} = (1 - 3\cos^2\theta') \left(\frac{3\cos^2\gamma_{ij} - 1}{2}\right), \tag{3.25}$$

where θ' is the angle between $\boldsymbol{B_0}$ and the rotation axis, and γ_{ij} is the angle between the

---

1   In real samples nuclei having the same γ are often placed in different electronic environments which might lead to significant differences in the local magnetic fields and hence in the precession frequencies.

rotation axis and $\boldsymbol{r}_{ij}$. If one chose $\theta' = \theta_{\mathrm{m}}$, where

$$1 - 3\cos^2\theta_{\mathrm{m}} = 0, \tag{3.26}$$

the time-averaged dipolar coupling would vanish[1]. The angle θ_{m} is known as the magic angle.

3.5.2 The method of spin echoes

The decay of the transversal magnetization due to a distribution of static fields is not irreversible. This was found in a breakthrough experiment by Hahn, in which applying a π-pulse at time τ after the $\pi/2$-pulse leads to the build-up of an echo at 2τ [Abr61], i.e., refocusing in phase of all the individual moments and restoring of the full transversal magnetization that was created by the first pulse.

A complete reversibility is given only if the spins do not interact with each other. Since they do, in reality the echo maximum decays with τ due to the homonuclear[2] spin-spin interactions, which cannot be refocused by the π-pulse. Moreover, if the distribution of fields that causes the transversal relaxation is not static, but changes on the time scale of the spin-echo experiment, this would also lead to a decay of the spin-echo.

One can observe the spin-echo decay by measuring the magnitude M_{SE} of the spin echo at different τs. Often the decay is well described by an exponential

$$M_{\mathrm{SE}}(2\tau) = M_{\mathrm{SE}}(0)\exp\left(-\frac{2\tau}{T_2}\right) \tag{3.27}$$

or a Gaussian-like decay function of time

$$M_{\mathrm{SE}}(2\tau) = M_{\mathrm{SE}}(0)\exp\left(-\frac{(2\tau)^2}{2T_{2\mathrm{G}}^2}\right), \tag{3.28}$$

with spin-echo decay constants T_2 and $T_{2\mathrm{G}}$, respectively.

3.6 NMR shift tensor

So far we have considered the interactions between the nuclear spins and the surrounding electrons only as a mechanism for longitudinal relaxation, or as a mediator of indirect internuclear coupling. An important ubiquitous effect of the presence of electrons in the sample is the modification of the local field at the nuclear site. As mentioned before, the local magnetic field is probed by the precession frequency of the nuclear spin and hence, useful information (about the coordination symmetry of the atom and the properties of itinerant electrons) can be gained by measuring the frequency shift (and its angular dependence). For convenience, a field-independent NMR shift K is defined with respect to a standard reference sample with a resonance frequency ω_{ref}, measured under the same

---

1   This is true for any coupling having an angular dependence $1 - 3\cos^2\theta_{ij}$.
2   Among all of the spins that are inverted by the π-pulse.

experimental conditions as the resonance frequency of the sample ω_{sample}:

$$K = \frac{\omega_{\text{sample}} - \omega_{\text{ref}}}{\omega_{\text{ref}}} \times 10^6. \tag{3.29}$$

This definition is meaningful since the additional magnetic field induced by the electrons $\boldsymbol{B}_{\text{ind}}$ is proportional to the applied field $\boldsymbol{B_0}$, i.e.,

$$\boldsymbol{B}_{\text{ind}} = \boldsymbol{\delta} \boldsymbol{B_0}, \tag{3.30}$$

with $\boldsymbol{\delta}$ being a second-rank tensor, which can be diagonalized in the so-called principal-axis system (with the diagonal entries δ_{XX}, δ_{YY} and δ_{ZZ}). The Zeeman interaction Hamiltonian of the nucleus in $\boldsymbol{B}_{\text{ind}}$ is then

$$\begin{aligned}\mathcal{H}_{\text{S}} &= -\gamma\hbar\boldsymbol{I} \cdot (\boldsymbol{\delta}\boldsymbol{B_0}) \\ &= -\gamma\hbar I_z B_0 \left[\delta_{\text{iso}} + \frac{\delta_{\text{aniso}}}{2}\left(3\cos^2\beta_{\text{E}} - 1 + \eta\sin^2\beta_{\text{E}}\cos 2\alpha_{\text{E}}\right)\right]\end{aligned} \tag{3.31}$$

with $\delta_{\text{iso}} = \frac{1}{3}(\delta_{\text{XX}} + \delta_{\text{YY}} + \delta_{\text{ZZ}})$, $\delta_{\text{aniso}} = \delta_{\text{ZZ}} - \delta_{\text{iso}}$, and $\eta = \frac{\delta_{\text{XX}} - \delta_{\text{YY}}}{\delta_{\text{aniso}}}$ (if $|\delta_{\text{ZZ}} - \delta_{\text{iso}}| \geq |\delta_{\text{YY}} - \delta_{\text{iso}}| \geq |\delta_{\text{XX}} - \delta_{\text{iso}}|$)[1]. Hence, the frequency shift $\Delta\omega$ due to $\boldsymbol{B}_{\text{ind}}$ is given by

$$\Delta\omega(\alpha_{\text{E}},\beta_{\text{E}}) = \omega_0 \left[\delta_{\text{iso}} + \frac{\delta_{\text{aniso}}}{2}\left(3\cos^2\beta_{\text{E}} - 1 + \eta\sin^2\beta_{\text{E}}\cos 2\alpha_{\text{E}}\right)\right], \tag{3.32}$$

depending on the Euler angles α_{E} and β_{E} relating the principal-axis system to the laboratory frame where $z \parallel \boldsymbol{B_0}$. By measuring the angular dependence of the NMR shift K (via changing the orientation of a single crystal in the applied field), one can obtain the parameters describing the NMR shift tensor: the isotropic shift K_{iso}, the shift anisotropy K_{aniso}, and the asymmetry parameter η.

In ideal powder samples, all angles (α_{E}, β_{E}) are distributed randomly, giving rise to a spread of resonant frequencies, i.e., a broadening of the powder spectrum in comparison to the single crystal spectrum. The intensity pattern of the powder spectrum can be calculated [Sli10]. It contains quite characteristic singularities from which K_{iso}, K_{aniso} and η can also be deduced.

3.6.1 Chemical and Knight shift contributions

The valence and itinerant electrons contribute independently to the local magnetic field at the nucleus and the corresponding NMR shift contributions are called chemical and Knight shift, respectively.

Chemical shift

The origin of the chemical shift is twofold: first, the motion of the electronic charges, and second the polarization of the electronic shells (of the valence electrons) in the external field B_0.

---

[1] In the case of axial symmetry $\delta_{\text{XX}} = \delta_{\text{YY}} \neq \delta_{\text{ZZ}}$, i.e., $\eta = 0$, and in the case of cubic symmetry additionally $\delta_{\text{aniso}} = 0$.

Knight shift

The Knight shift is named after Walter D. Knight, who first observed the phenomenon in 1956. It originates from the magnetic-field-induced spin polarization and orbital currents of the itinerant electrons. The latter produce an additional magnetic field at the nucleus, leading to an *orbital* Knight shift, and the former acts directly on the nucleus via the *contact* and *dipolar* interactions, and indirectly through the *core polarization* effect.

Chapter 4

NMR in Bi_2Se_3 and Bi_2Te_3 – a review

At the beginning of this work (end of 2011), there were no literature sources on NMR in topological insulator materials. Since then several studies, mainly on Bi_2Se_3 and Bi_2Te_3, have been published, cf. Tab. 4.1. The investigated samples have various doping levels and material forms: bulky single crystals, mortar-and-pestle powders, as well as nanoparticles with much bigger surface-to-volume ratio. The studies show that the measured NMR parameters, i.e., frequency shifts, longitudinal relaxation, spin-echo decay, lineshape, and linewidth are sensitive to the electronic properties and that with NMR one can gain information about the presence of defects, the penetration depth, site-specific spin susceptibilities, hyperfine coupling strengths and more. Predominantly, information about the bulk properties was obtained due to the fact that the number of nuclei in the bulk outweighs the number of nuclei near the surface. Moreover, significant differences in the NMR spectra and T_1s of nanosized samples (having large surface-to-volume ratios) with respect to bulky samples show that NMR can distinguish surface and bulk properties, even

Table 4.1: Published NMR experimental studies on TI materials of different physical forms: powder (p), single crystal (sc) and nanoparticles (np). * X = Te/Se/S.

Year	Publication	Material	Form	Nucleus
2012	Taylor et al. [Tay12]	Bi_2Se_3, Bi_2Te_3	p	^{77}Se, ^{125}Te
	Young et al. [You12]	Bi_2Se_3	sc	^{209}Bi
2013	Koumoulis et al. [Kou13]	Bi_2Te_3	np	^{125}Te
	Nisson et al. [Nis13]	Bi_2Se_3	sc	^{209}Bi
2014	Koumoulis et al. [Kou14]	$Bi_xSb_{2-x}Te_3$, $Bi_2Te_2X^*$	p	^{125}Te
	Nisson et al. [Nis14]	Bi_2Se_3	np, p, sc	^{209}Bi
2015	Mukhopadhyay et al. [Muk15]	Bi_2Se_3	sc	^{209}Bi
	Podorozhkin et al. [Pod15]	Bi_2Te_3	sc	^{125}Te
2016	Georgieva et al. [Geo16]	Bi_2Se_3, $Cu_{0.15}Bi_2Se_3$	sc, p	^{77}Se
	Matano et al. [Mat16]	$Cu_{0.3}Bi_2Se_3$	sc	^{77}Se
	Levin et al. [Lev16]	Bi_2Te_3	sc	^{125}Te
2017	Antonenko et al. [Ant17b]	Bi_2Te_3	sc	^{125}Te
	Antonenko et al. [Ant17a]	Bi_2Te_3	sc, p	^{125}Te
2018	Antonenko et al. [Ant18]	Bi_2Se_3	sc	^{77}Se
	Choi and Lee [Cho18]	Bi_2Se_3	np	^{77}Se

in defect-rich samples with large bulk conductivity.

The nuclei under investigation were ^{209}Bi, ^{125}Te and ^{77}Se. Their NMR properties are summarized in Tab. 4.2. ^{77}Se and ^{125}Te are both spin-1/2 nuclei with relatively low natural abundances of less than 7.7%. The two distinct (outer and inner) sites occupied by Se or Te atoms are expected to give rise to two different ^{77}Se or ^{125}Te NMR signals, respectively. ^{209}Bi, on the other hand, is 100% abundant and occupies a single lattice site, which should cause a single NMR line. However, as a spin-9/2 nucleus, ^{209}Bi possesses a quadrupole moment, cf. Tab. 4.2, and given that the lattice symmetry is non-cubic, the ^{209}Bi NMR signal is likely quadrupolarly split into 9 lines.

Here, a review on the current state of the art is given, in order to set up a framework for comparison and assessment of the experimental results presented in the following chapters. Firstly we will consider experimental ^{77}Se and ^{125}Te, and thereafter ^{209}Bi NMR; secondly we will review theories of NMR in Bi_2Se_3 and Bi_2Te_3; and finally open questions and tasks for the future will be identified.

4.1 ^{77}Se and ^{125}Te

The first publications on ^{77}Se and ^{125}Te NMR of Bi_2Se_3 and Bi_2Te_3 include solely powder samples studied at applied static magnetic fields of ∼7.05 T [Kou13; Kou14; Tay12]. Taylor et al. [Tay12] and Koumoulis et al. [Kou14] show spectra of bulky powder samples and study their longitudinal relaxation as a function of temperature. Spectra of Bi_2Se_3 and Bi_2Te_3 powders from [Tay12] are depicted in Fig. 4.1(a) and (g), respectively. In [Kou14] the Bi_2Te_3 data from [Tay12] is compared to ^{125}Te NMR of $Bi_xSb_{2-x}Te_3$ (x = 0, 0.5), Bi_2Te_2Se and Bi_2Te_2S. Although the existence of two inequivalent Se (Te) crystal sites in Bi_2Se_3 (Bi_2Te_3) is mentioned by the authors, it is ignored in the interpretation of the spectra. When more spectral components are distinguished, they are attributed to distinct local defect concentrations, rather than to different local environments of the distinct lattice sites. The temperature dependence of the ^{125}Te T_1 in [Tay12] reveals "thermally activated relaxation arising from interaction with charge carriers" above 320 K and "a Korringa-law behavior" in the low-temperature range (173-250 K). The latter finding is rather questionable since the data points are too few and their uncertainty is too big. Activation energies and Korringa products extracted from the ^{125}Te relaxation data in [Kou14] have been used as a basis for conclusions on the bulk conductivity and defect concentrations of the various samples, asserting that the Bi_2Te_2Se compound is the best TI among the materials investigated therein.

A first attempt at studying a TI surface with NMR was made in another study by Koumoulis et al. [Kou13], comparing the ^{125}Te NMR of ball-milled Bi_2Te_3 powders (having

Table 4.2: Nuclear spin I, gyromagnetic ratio γ, quadrupole moment Q and natural abundance of stable NMR active isotopes.

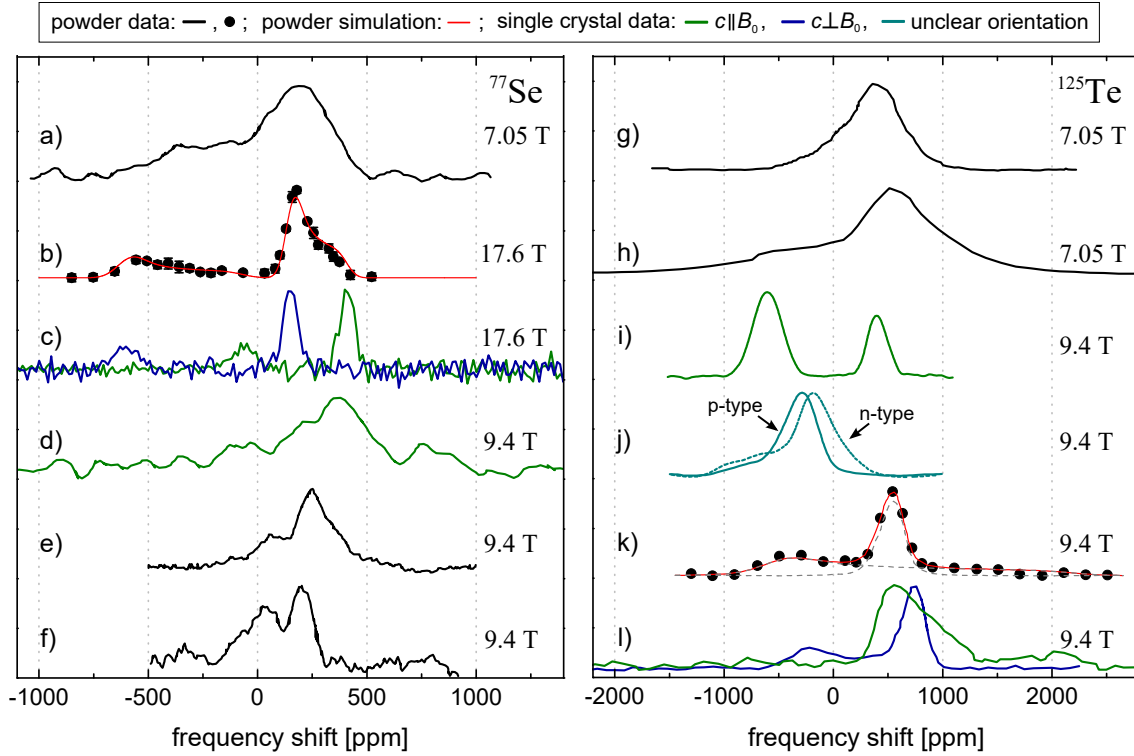| isotope	I	$\gamma/2\pi$ [MHz/T]	Q [barn]	abundance [%]
^{77}Se	1/2	8.1573046		7.63
^{125}Te	1/2	−13.545423		7.139
^{209}Bi	9/2	6.9630	−0.37	100

Figure 4.1: Normalized ^{77}Se (left) and ^{125}Te (right) spectra of Bi_2Se_3 and Bi_2Te_3 adapted from publications by (a,g) Taylor et al. [Tay12], (b,c) Georgieva et al. [Geo16], (d) Antonenko et al. [Ant18], (e,f) Choi and Lee [Cho18], (h) Koumoulis et al. [Kou13], (i) Podorozhkin et al. [Pod15], (j) Levin et al. [Lev16] and (k,l) Antnoneko et al. [Ant17a]. The presented samples are bulky powders and single crystals (see legend) except for the spectra (e) and (h), corresponding to Bi_2Se_3 and Bi_2Te_3 nanoparticles, respectively, and (f), corresponding to a mixed sample of Bi_2Se_3 and Al_2O_3 nanoparticles with a molar ratio $Bi_2Se_3{:}Al_2O_3$ of 4:3. All spectra were acquired at ambient conditions and various applied magnetic field strengths (see graphs) and for (e) and (f) a MAS rate of 10 kHz was used. Shifts are given with respect to $(CH_3)_2X$ (X=Se/Te).

various grain sizes in the nanometer-range) to the data from the bulky Bi_2Te_3 powder. With decreasing grain size the relaxation rate $1/T_1$ increased abruptly below 33 nm and a shoulder peak appeared in the spectrum at 55 nm. Fig. 4.1(h) displays the ^{125}Te spectrum of the 19 nm sample, which showed a constant Korringa product in the range 140-420 K.[1] These indicators of an abrupt increase of metallicity with decreasing particle size have been interpreted to be more likely a surface effect rather than due to increasing bulk damage since the latter would lead to gradual changes of the NMR parameters.

The first single crystal Bi_2Te_3 NMR data were published by Podorozhkin et al. [Pod15]. Two separate ^{125}Te NMR signals at $\sim$+400 ppm and $\sim$-600 ppm have been recorded,

---

1 This behavior is in contrast to the mostly thermally activated relaxation found for the bulky Bi_2Te_3 powder, whose spectrum is depicted in Fig. 4.1(g).

cf. Fig. 4.1(i), and assigned based on comparison to the 19 nm sample from [Kou13], cf. Fig. 4.1(h), to bulk and surface nuclei, respectively. The peculiar intensity ratio of the signals has not been discussed and only the "bulk" signal has been investigated further. A significant shift decrease and linewidth increase thereof were found with decreasing temperature from 295 K down to 10 K. The angular dependence of the shift of the "bulk" signal was measured at room temperature and, since it does not agree with the local symmetry of any of the Te sites, the question arises whether the single crystal was oriented properly in the external magnetic field as it is claimed ($c \parallel B_0$).

For the first time, signals due to the two inequivalent ^{77}Se sites have been unambiguously assigned and thoroughly characterized in a publication by Georgieva et al. [Geo16], which is a part of this thesis. In that work single crystal Bi_2Se_3 and $Cu_{0.15}Bi_2Se_3$ samples have been investigated with ^{77}Se NMR at the relatively high external field strength of 17.6 T. Figure 4.1(c) depicts the weaker ^{77}Se signal corresponding to Se_{in} and the two-times stronger signal due to Se_{out} (measured for two orientations of Bi_2Se_3 in the magnetic field). Additionally, the ^{77}Se spectrum of bulky Bi_2Se_3 powder has been measured and simulated based on the single crystal data, cf. Fig. 4.1(b). The fact that the single crystal and powder data agree and that the penetration depth of the radiofrequency field has been determined to 80 µm lead to the conclusion that the measured signals are due to bulk (rather than surface) nuclei.

Shortly after [Geo16] was published, Matano et al. showed a similar single crystal ^{77}Se NMR spectrum of $Cu_{0.3}Bi_2Se_3$ in the supplementary information of their publication [Mat16]. In the main article, the authors report on a peculiar two-fold rotational symmetry (upon rotation within the *ab*-plane having a three-fold rotational symmetry) of the Knight shift for the stronger ^{77}Se signal in the superconducting $Cu_{0.3}Bi_2Se_3$ below $T_c = 3.4$ K and interpret it as spin-triplet superconductivity.

Unexpectedly large field-independent ^{77}Se linewidths have been measured for both Bi_2Se_3 and $Cu_{0.15}Bi_2Se_3$ in [Geo16] and explained by a strong Bloembergen-Rowland-like indirect internuclear coupling mediated by bulk electrons. This finding complies with the fact that magic angle spinning did not result in any significant narrowing or breaking into side bands of the resonances [Geo16; Tay12]. Field-independence of the linewidth in Hz means a linearly increasing linewidth in ppm with decreasing magnetic field which explains the discrepancy in the powder spectra of Taylor et al. and Georgieva et al., cf. Fig. 4.1(a) and (b). The question arises, whether an indirect nuclear coupling is present in Bi_2Te_3 as well. If so, larger applied magnetic field strengths would increase the resolution of the ^{125}Te spectra.

Significant differences in the spin-echo decays and longitudinal relaxation times of Se_{in} and Se_{out} have been reported in [Geo16] and need to be kept in mind when interpreting ^{77}Se and ^{125}Te NMR spectra of Bi_2Se_3 and Bi_2Te_3. For example, in the supplementary information of [Mat16] the Se_{in} signal was found to disappear from the spectrum for longer pulse separations.

In the ^{125}Te NMR study at 9.4 T by Levin et al. [Lev16] differences in the shifts and T_1s of electron- and hole-doped Bi_2Te_3 single crystals suggest that NMR is sensitive to the doping type. The ^{125}Te spectra, depicted in Fig. 4.1(j), consist of a main peak and a small shoulder, assigned to normal and defect-rich bulk regions, respectively, leaving the question of distinguishing the Te_{in} and Te_{out} NMR signals open until the following two publications by Antonenko et al. [Ant17a; Ant17b], which will be considered next.
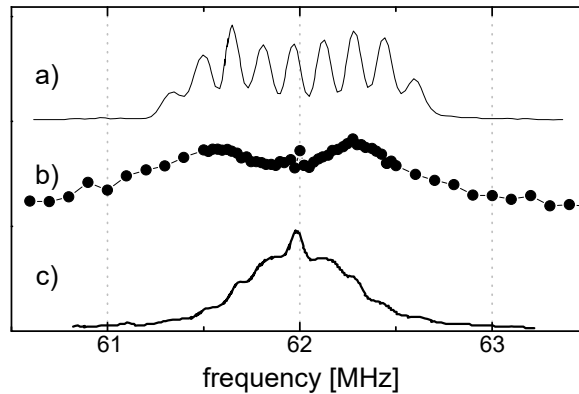
Figure 4.2: ^{209}Bi spectra of Bi_2Se_3 at $9\,T$ and $10\,K$ adapted from [Nis14]: measured spectra for (a) a single crystal oriented as $c\,\|\,B_0$ and (b) a mortar-and-pestle powder, and a simulation of the powder spectrum (c) based on a weighted sum of the angular-dependent single crystal data.

In [Ant17b] ^{125}Te NMR of Bi_2Te_3 powder and a single crystal plate have been performed for $B_0 \simeq 9.4\,T$ at room temperature and $16.5\,K$, and in [Ant17a] several intermediate temperatures have been added. For the first time, a two-component bulk ^{125}Te powder spectrum has been shown, cf. Fig. 4.1(k), and found to agree with the single crystal spectra, cf. Fig. 4.1(l), at room temperature. The weaker and stronger signals have been attributed to the Te_{in} and Te_{out} lattice sites, respectively, in contrast to the earlier assignment by Podorozhkin et al. [Pod15]. While "the temperature dependences of the spectra for the powder and plates with the orientation $c \perp B_0$ agree with each other", "the spectra for the plates with orientation $c\,\|\,B_0$ demonstrate peculiar behavior below $91\,K$". For $c \perp B_0$ both, the Te_{in} and Te_{out} lines move to lower frequencies with decreasing temperature (explained by a reduction of Knight shift)[1]. A more complicated behavior is observed for $c\,\|\,B_0$: while the spectrum is nearly unchanged between $293\,K$ and $132\,K$, at $91\,K$ the weaker signal seems to have moved to the negative shift range, and with further decreasing temperatures $<91\,K$ both lines become broader and their intensity ratio gets closer to 1 until at $16\,K$ only a single asymmetrical line can be distinguished. This peculiar behavior might be "connected with Landau quantization of the surface", as the authors claimed, however, in order to achieve clarity, temperature-dependent measurements of the full angular dependence of the shifts and a careful determination of the relative intensity (taking into account potential spin-echo-decay differences) are needed.

Recently, two ^{77}Se NMR studies at $\sim 9.4\,T$ have been published by Antonenko et al. [Ant18] and Choi and Lee [Cho18]. In [Ant18] the spectrum of a Bi_2Se_3 single crystal has been measured for $c\,\|\,B_0$ at 3 different temperatures (293, 88 and $15.8\,K$) with relatively poor resolution and signal-to-noise ratio. Interestingly, no significant temperature dependence of the ^{77}Se shift and linewidth has been found, in contrast to the ^{125}Te NMR of Bi_2Te_3 in [Ant17a; Ant17b; Pod15].

---

[1] A thermal activation behavior of the Te_{in} and Te_{out} Knight shifts has been found and the same thermal activation energy of the charge carriers ($\sim 25\,meV$) has been extracted from both signals.

In the publication by Choi and Lee [Cho18] MAS ^{77}Se spectra of Bi_2Se_3 nanoparticles (of roughly $100\,nm$ size) physically mixed with insulating Al_2O_3 nanoparticles ($\sim50\,nm$) in various proportions are presented. The spectrum of the non-diluted Bi_2Se_3 nanoparticles consists of a main peak and a shoulder, cf. Fig. 4.1(e). By increasing the molar ratio Al_2O_3/Bi_2Se_3 to 75%, the intensity of the shoulder grows to $\sim65\%$ of the total intensity, cf. Fig. 4.1(f), and Choi and Lee attribute these spectral changes to an increase in the surface-to-volume ratio. The last findings reinforce the hope that characterization of the topological surface states by means of NMR is feasible. However, keeping in mind the complexity of the bulk NMR properties, revealed in the previous studies, a more thorough investigation is called for, including absolute intensity determination, relaxation measurements, and better spectral resolution in a higher magnetic field.

4.2 ^{209}Bi

All of the publications on ^{209}Bi NMR known to the author so far, consider Bi_2Se_3 samples and report on quadrupolar split single crystal spectra consisting of 9 lines (one central transition and eight satellite peaks) with a quadrupole splitting of 0.15-0.18 MHz [Muk15; Nis13; Nis14; You12]. The spectra span a large total width of up to $2\,MHz$ which is why the frequency-shifted-and-summed Fourier transform method (using spin-echo pulse sequences) was applied in all studies. A proper excitation of each individual signal is therefore questionable. Indeed, atypical intensity profiles have been reported for most samples, having a much smaller (or nearly equal) intensity of the peaks in the center of the spectrum compared to the outer satellites[1], cf. Fig. 4.2(a). Young et al. [You12] explained this fact with shorter spin-echo decay times in the central region than in the edges of the spectrum.

The studies of Young et al. [You12] and Nisson et al. [Nis13] (including various single crystal samples) have shown that the ^{209}Bi spectra and T_1 are sensitive to disorder[2] and the charge carrier density n of the sample. From the measured dependence of ^{209}Bi Knight shifts on n in [Nis13], the hyperfine coupling energy of ^{209}Bi could be estimated to $27\,\mu eV$. The measured linewidths of the central peaks largely exceed (by two orders of magnitude) the theoretical linewidth contribution from dipole-dipole coupling, similar to the ^{77}Se and ^{125}Te linewidths.

Although the angular dependence of the single crystal spectrum was found to agree with the local symmetry of the Bi lattice site[3] [Muk15; Nis14; You12], the powder spectra measured in [Nis14], cf. Fig. 4.2(b), disagree severely with the single-crystal-data-based simulation, cf. Fig. 4.2(c). On the other hand, the spectra of nanowires and mortar-and-pestle ground powder agree well with each other. Although Nisson et al. [Nis14] discuss several possible interpretation scenarios, understanding the "anomalous" shapes of the

---

[1] Normally the intensity drops off from the central transition to the outermost satellites.

[2] The 9 lines could be seen only in phase-pure Bi_2Se_3 single crystals and not in $Cu_xBi_2Se_3$ or Bi_2Te_2Se.

[3] The angular dependence of the shift of the central line was found to agree with an axially symmetric shift tensor (expected from the local coordination symmetry of the bismuth site in the crystals) and moreover, all nine lines were found to merge in the vicinity of the magic angle, as expected.

[209]Bi powder spectra of Bi$_2$Se$_3$ remains a task for the future.

In a combined high magnetic field NMR and transport study, Mukhopadhyay et al. [Muk15] have determined precisely the electron g-factor and have extracted the contact hyperfine coupling constant from the isotropic [209]Bi NMR shift. The study moreover shows that "NMR can probe the electron spin polarization in the bulk of Bi$_2$Se$_3$ directly".

4.3 Theory of NMR in Bi$_2$Se$_3$ and Bi$_2$Te$_3$

The experimental studies discussed so far revealed that NMR in both, bulky Bi$_2$Se$_3$ and Bi$_2$Te$_3$ samples, and such having an increased surface-to-volume ratio have nontrivial features. Lacking theoretical calculations concerning NMR shift and T_1 in doped TIs like Bi$_2$Se$_3$ and Bi$_2$Te$_3$, the results were mostly interpreted based on theories developed for simpler systems like an ideal Fermi-gas or a semiconductor, disregarding potential effects due to the presence of strong SOC and bulk band inversion in the TI materials.

In 2016 the indirect internuclear coupling constants and the consequent [77]Se linewidth in bulk Bi$_2$Se$_3$ have been calculated and compared with the experimental findings by Ion Garate [Geo16]. The presented simplified model calculation supported the interpretation of the enhanced field-independent linewidths and revealed a dominance of the interband part of the electronic spin susceptibility in Bi$_2$Se$_3$ over the intraband part. However, being based on a minimal $\mathbf{k} \cdot \mathbf{p}$ model describing the electronic structure only in the vicinity of the Γ point, the calculation required fitting to experimental data, in order to estimate the contact hyperfine couplings.

Not long after that, Boutin, Ramírez-Ruiz, and Garate [Bou16] presented a much more advanced, tight-binding model calculation of the *carrier-density-dependent* NMR shifts in Bi$_2$Se$_3$ and Bi$_2$Te$_3$, obtaining the first theoretical estimates of the hyperfine couplings and *g*-factors in these materials. While no significant influence of the band inversion has been found, the strong SOC in these materials and their layered crystal structure lead to peculiar properties, which have not been discussed so far: a strong uniaxial anisotropy of the contact Knight shift and a significant isotropic part of the dipolar Knight shift. Moreover, the Van Vleck term was found to make a "large density-independent contribution to the itinerant spin density" due to the strong SOC. It was established that the contact interaction indeed dominates the isotropic [209]Bi Knight shift, verifying interpretations from before [Muk15; You12]. On the contrary, [77]Se and [125]Te isotropic shifts are predicted to be dominated by dipolar and orbital shift contributions, rather than the contact one.

Recently, a quantitative theory of electric-field-induced splitting of NMR peaks for [77]Se, [125]Te, and [209]Bi in Bi$_2$Se$_3$ and Bi$_2$Te$_3$ was published [Ram17] and suggested as a detection scheme for hidden spin and orbital polarizations in these materials.

Concerning the theory of NMR as a probe for TSS, two other theoretical studies should be mentioned: the one by Zocher and Rosenow [Zoc13] on the local spin susceptibility of doped 3D TIs with a superconducting pairing, and the one by Schlottmann [Sch14] regarding the NMR relaxation in a topological Kondo insulator. The former suggests the NMR Knight shift in Cu-doped Bi$_2$Se$_3$ as a probe for pairing symmetry in the superconducting state. The latter makes predictions on a superposition of relaxation rates (due to an exponential decrease of the TSS with distance) and consequent stretched-exponential relaxation in the vicinity of the surface.

4.4 Open questions

Although a significant experimental effort has been made over the past 6 years, the understanding of the ^{77}Se, ^{125}Te and ^{209}Bi NMR of Bi_2Se_3 and Bi_2Te_3 is still far from complete and remains challenging. Specifically, the following open questions can be named: explaining the "anomalous" ^{209}Bi spectral shapes of Bi_2Se_3 powders and single crystals, understanding the peculiar ^{125}Te spectral changes with temperature for the Bi_2Te_3 single crystal, and broadening the temperature and charge carrier density range for ^{77}Se NMR of Bi_2Se_3.

The study of Choi and Lee [Cho18] demonstrated a potentially successful NMR approach to the topological surface states in the model 3D TI Bi_2Se_3 and calls for deeper investigations.

Chapter 5

^{77}Se NMR in Cu$_x$Bi$_2$Se$_3$ single crystals

5.1 Samples and experimental setup

5.1.1 Sample preparation and characterization

In this chapter Cu$_x$Bi$_2$Se$_3$ single crystal samples with x = 0, 0.10, 0.125, 0.15, and 0.17 are considered. All crystals have been grown as described in Ref. [Das11] in the groups of Kazuo Kadowaki (Bi$_2$Se$_3$, Cu$_{0.10}$Bi$_2$Se$_3$, and Cu$_{0.15}$Bi$_2$Se$_3$) and Grant V. M. Williams (Cu$_{0.125}$Bi$_2$Se$_3$ and Cu$_{0.17}$Bi$_2$Se$_3$, by Shen Chong). The silver color platelet crystals had edge lengths of 0.5 to 5 mm, the Bi$_2$Se$_3$ crystal is shown in the upper inset of Fig. 5.2. For all samples the crystal structure and phase purity have been verified with X-ray diffraction (XRD) and, for the Cu-doped samples, magnetization measurements have been performed by our collaborators. Shortly after their production the samples with the biggest Cu content, Cu$_{0.17}$Bi$_2$Se$_3$ and Cu$_{0.15}$Bi$_2$Se$_3$, had a superconducting transition temperature of $\sim$3 K, while Cu$_{0.125}$Bi$_2$Se$_3$ showed no significant signature of superconductivity above 2 K, cf. the upper panel in Fig. 5.1 and Appendix A. Cu$_{0.10}$Bi$_2$Se$_3$ showed no signature of a superconducting transition 6 years after its production, cf. Fig. A.1 in Appendix A.

Aging of Cu$_{0.15}$Bi$_2$Se$_3$

An aging effect of the Cu$_{0.15}$Bi$_2$Se$_3$ sample has been noticed approximately 1.5 years after its production. By that time, the surface of the crystal had lost its luster and acquired a rusty coloring, accompanied by a significant change of NMR parameters, which will be described in the next section. The crystal has been mostly kept in a desiccator filled with air. During the week-long NMR measurements, however, the crystal was wrapped in Teflon tape within the NMR coil surrounded by air. Note that while the Bi$_2$Se$_3$ single crystal has a comparable history of storing and measuring, it has not shown the effects described for Cu$_{0.15}$Bi$_2$Se$_3$. Note also that the other Cu doped samples Cu$_{0.10}$Bi$_2$Se$_3$, Cu$_{0.125}$Bi$_2$Se$_3$, and Cu$_{0.17}$Bi$_2$Se$_3$ had an unaltered shiny surface during all NMR measurements.

The temperature dependence of the magnetization of the electrons M_e has been found to be significantly changed in the aged Cu$_{0.15}$Bi$_2$Se$_3$ crystal in comparison to the non-aged one. Fig. 5.1 shows DC-SQUID M_e measurements on Cu$_{0.15}$Bi$_2$Se$_3$ performed shortly after its production (upper plot) and $\sim$2 years later (lower plot). While the non-aged sample exhibits a clear superconducting transition at $\sim$3 K, the aged Cu$_{0.15}$Bi$_2$Se$_3$ sample shows no signature of superconductivity.

5.1.2 NMR setup

The NMR measurements presented in this chapter have been performed using commercial spectrometers by Bruker (Avance), and Tecmag (Apollo) combined with superconducting magnets providing various field strengths. Table 5.1 gives an overview of the used equipment. Commercial and home-built cryogenic probes have been used for all measurements together with bottom-loaded cryostats providing electrical grounding and radiation shielding of the probe on one hand, and the possibility for cooling with liquid nitrogen or helium on the other hand. The single crystals were placed in home-built sample holders (made of non-magnetic thermoplastics), as shown in Fig. 5.2, allowing for a fixed orientation of the crystal in the static magnetic field. The coil was wound by hand as tightly as possible around the sample fixture so that a possibly maximal filling factor was achieved, cf. Fig. 5.2. With this setup, the crystal orientation in the magnetic field could be adjusted with degree accuracy by rotating the crystal together with the coil around the coil's symmetry axis. All investigated single crystals had flat shapes (similar to the Bi$_2$Se$_3$ single crystal shown in the upper inset of Fig. 5.2) and their flat sides were expected to be parallel to the crystal's *ab*-plane, i.e., the *c*-axis was expected to be perpendicular to the flat surface of each crystal. Therefore, by rotating the sample in the sample holder, the orientation of the *c*-axis was expected to change from perpendicular to parallel (and back to perpendicular) to the static magnetic field. Exact determination and adjustment of the orientation of the *c*-axis have been done by measuring the anisotropy of the NMR shift (see Section 5.3). Rotation of the crystal around the *c*-axis could be achieved within few degrees by turning the fixture in a position $c \perp B_0$ and tilting the whole sample holder by a few degrees, as the lower inset of Fig. 5.2 demonstrates.

Table 5.1: NMR spectrometer consoles and static magnetic fields B_0 used in this work.

B_0 [T]	console
17.6	Avance 750
11.7	Avance III HD / Apollo (two-channel)
9.4	Avance III HD
7.0	Apollo (one-channel)

Pulse length determination

For the determination of the length of a π-pulse at a certain power we have performed nutation experiments on the ^{63}Cu signal in metallic copper powder in epoxy using the same setup as for the single crystals.[1] From the measured ^{63}Cu π-pulse length $^{63}\tau_\pi$ we have calculated an expected ^{77}Se π-pulse length $^{77}\tau_\pi$ using the formula

$$\tau_\pi = \frac{\pi}{\gamma B_1} = \sqrt{\frac{2\pi^2 \omega_0 V}{\gamma^2 \mu_0 Q P}} \tag{5.1}$$

---

[1] Each copper sample has been cut to a size similar to the respective single crystal, in order to achieve a similar filling factor of the coil.

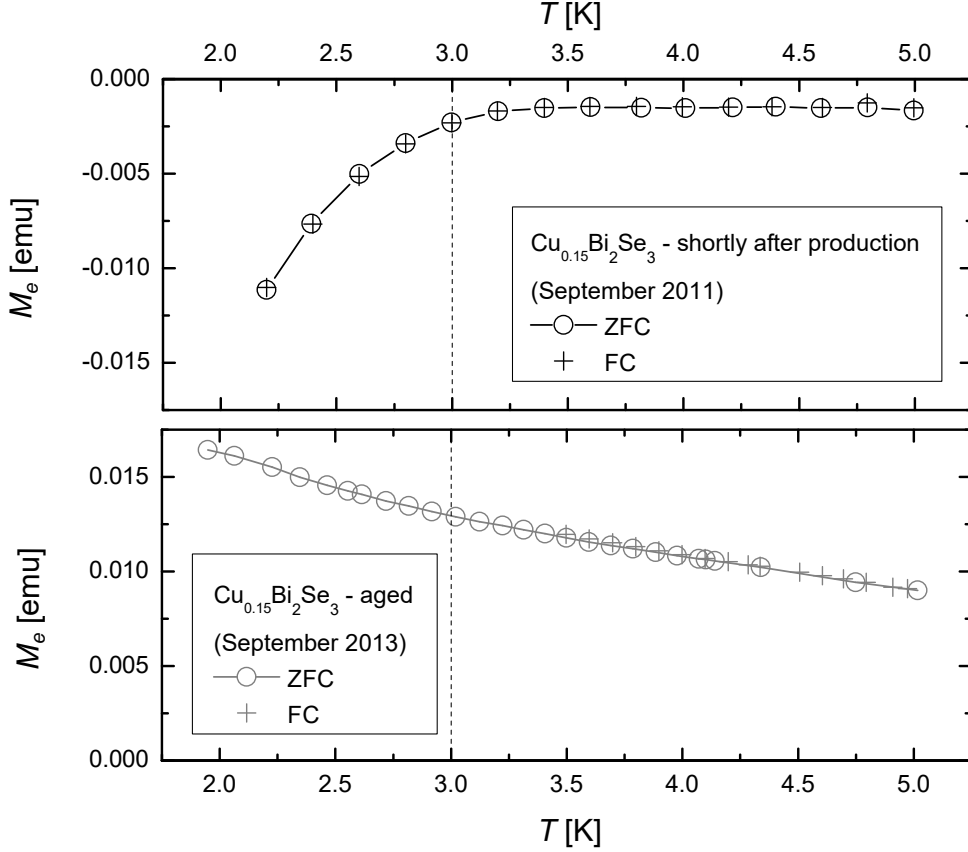**Figure 5.1:** DC-SQUID magnetization measurements in zero-field-cooling (ZFC) and field-cooling (FC, at $H = 100$ Oe) modes of the $Cu_{0.15}Bi_2Se_3$ single crystal shortly after its production (upper plot) and after two years of air exposure (lower plot). The first measurements have been performed in the group of Kazuo Kadowaki and the later ones - by Sebastian Sambale using a SQUID of the group of Pablo Esquinazi at Leipzig University. The vertical dashed line marks the superconducting transition in the non-aged crystal at $T_c \approx 3$ K.

and correcting for γ, ω_0 and Q differences.[1] The so extracted $^{77}\tau_\pi$ value has been then verified in a series of spin-echo experiments on the single crystal with varying power levels, in which the optimal power yielding a maximal signal was determined.

Shift determination

As a reference sample for determining the shift we have used the same copper sample as for the pulse length determination. The center of mass of the ~ 10 kHz broad ^{63}Cu NMR line was extracted from a Gaussian fit. Based on this value we have calculated the ^{77}Se frequency shift with respect to the standard reference $(CH_3)_2$Se using the universal shift scale by Harris et al. [Har08] as described in Appendix B.

---

1   This can be done in spite of ^{63}Cu being a quadrupolar spin-3/2 nucleus, since the cubic lattice symmetry of metallic copper leads to zero electric field gradient and hence no quadrupolar splitting, i.e., a single ^{63}Cu NMR line.
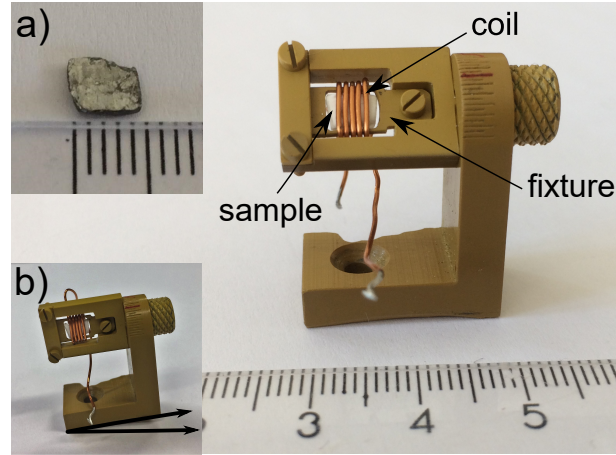
Figure 5.2: A tailored sample holder made of nonmagnetic thermoplastic. The single crystal sample is wrapped in teflon tape and mounted in the fixture around which the coil is tightly wound. The upper inset (a) shows a Bi$_2$Se$_3$ single crystal. The lower inset (b) demonstrates how the sample holder has been tilted in order to achieve rotation around a second axis (within a few degrees).

Q-factors

Typical quality factors (Q-factors) for the measurements described in this chapter were 50-70 for the Cu-doped Bi$_2$Se$_3$ samples and 30-40 for the Bi$_2$Se$_3$ crystal.

The quality factor $Q = \omega L/r$ of the NMR probe was drastically reduced when one of the single crystals was inserted into the coil – by factor 5 to 7 in the case of the Bi$_2$Se$_3$ crystal and by factor 2 to 3 in the case of the Cu$_x$Bi$_2$Se$_3$ samples. We found that this effect is due to a sample-induced change of the apparent serial resistance of the coil r, rather than of its inductance L: in the case of Bi$_2$Se$_3$, we find the resistance increased 4.7 times with respect to the resistance of the empty coil while the inductance was nearly unchanged, cf. Appendix C. In comparison, a metallic copper piece with a comparable volume leads to a reduction of the inductance by 20% and a 1.2 times increased resistance, and a Q decreased by only a factor of 1.4.

5.2 Spectra

5.2.1 Results

Fig. 5.3 shows typical ^{77}Se NMR spectra of Bi$_2$Se$_3$ and Cu$_x$Bi$_2$Se$_3$ single crystals with x = 0.1, 0.125, 0.15 and 0.17. The spectra are as measured (see experimental details at the end of this section), however, their maxima have been normalized to 1 for better comparison among the samples. All spectra contain two Gaussian shaped lines, a narrower and a wider one. The intensity ratio of the lines and their widths do not change significantly throughout all samples and orientations in the magnetic field, however, their shifts vary. For a fixed crystal orientation in the magnetic field ($c \parallel B_0$ or $c \perp B_0$) all spectra of Cu-doped samples show similar line shifts, significantly different from the shifts in Bi$_2$Se$_3$. Note that for all samples both lines undergo a significant shift change upon varying crystal orientation in the magnetic field (c.f. spectra shown left and right in Fig 5.3).
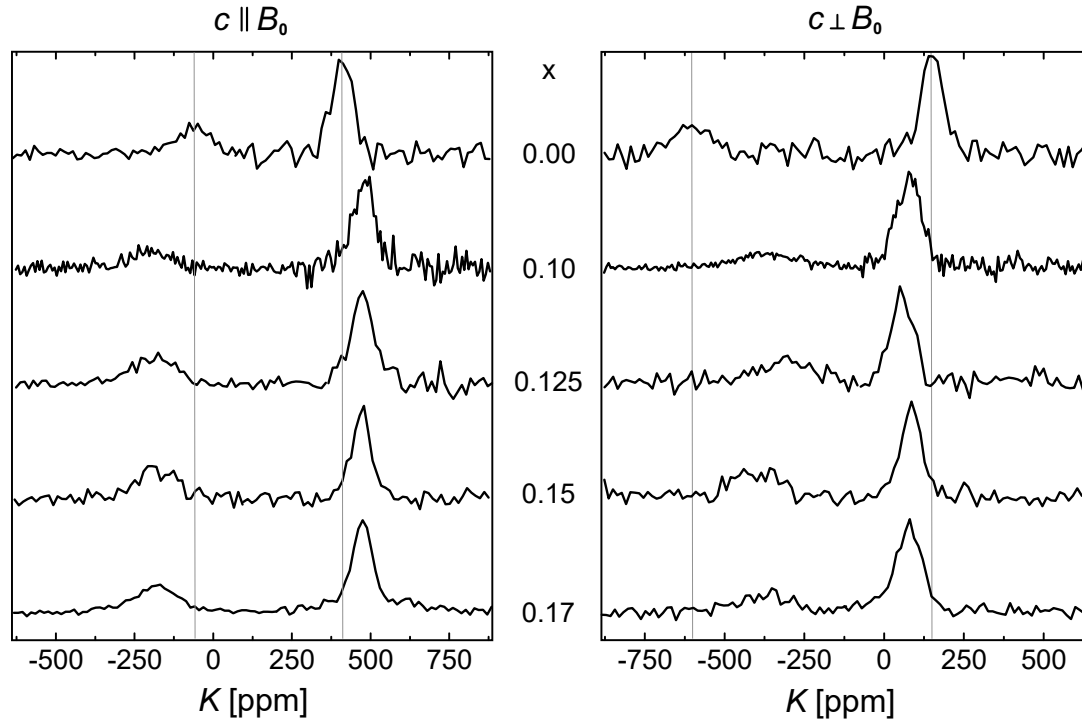
Figure 5.3: ^{77}Se NMR spectra of $Cu_xBi_2Se_3$ single crystals with different Cu content x (0, 0.1, 0.125, 0.15 and 0.17, from top to bottom) measured at two orientations of the crystal c-axis in the magnetic field B_0 (parallel and perpendicular, shown left and right, respectively). The gray vertical lines mark the center positions of the Bi_2Se_3 lines. All spectra were acquired at ambient conditions and $B_0 = 17.6\,T$. Shifts (K) are given with respect to $(CH_3)_2Se$.

Relative intensity

The intensity of the two signals has been compared after correcting for spin echo decay effects. We find for all crystals at both $c\,\|\,B_0$ and $c\perp B_0$ orientations that the narrow line is approximately 2 times more intense than the wider one.

Aging of $Cu_{0.15}Bi_2Se_3$

Upon aging, the ^{77}Se spectrum of $Cu_{0.15}Bi_2Se_3$ is altered, as Fig. 5.4 shows. The central positions of both signals have shifted significantly closer to the positions of the Bi_2Se_3 signals. In the same time, the linewidths and relative intensity of the lines have remained nearly unchanged.

Absolute intensity

The absolute ^{77}Se NMR intensity, which is proportional to the total number of spins contributing to the signal, has been estimated for the $Cu_{0.15}Bi_2Se_3$ single crystal sample (non-aged). The outcome was that $\gtrsim 25\%$ of the ^{77}Se nuclei available in the sample contribute to the spectrum. This indicates that only the outer skin of the single crystal, with a thickness of $\gtrsim 80\,\mu m$, is excited by the radio frequency field. A comparable penetration depth of $100\,\mu m$ can be estimated from resistivity data on a $Cu_{0.12}Bi_2Se_3$ sample with charge carrier density $n = 2\times 10^{20}\,cm^{-3}$ in [Hor10].

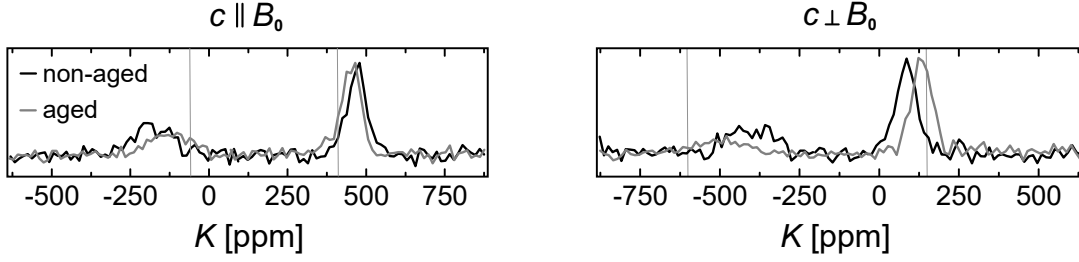**Figure 5.4:** ^{77}Se NMR spectra of the Cu$_{0.15}$Bi$_2$Se$_3$ single crystal (non-aged in black and aged in gray) measured at two orientations of the crystal c-axis in the magnetic field B_0 (parallel and perpendicular, shown left and right, respectively at ambient conditions and $B_0 = 17.6\,$T. Shifts (K) are given with respect to (CH$_3$)$_2$Se. The gray vertical lines mark the center positions of the Bi$_2$Se$_3$ lines.

5.2.2 Discussion

It is apparent that the observed ^{77}Se signals are due to bulk nuclei and the narrow (broad) one can be assigned to the outer (inner) selenium site Se$_{out}$ (Se$_{in}$), for the following reasons: (1) all measured spectra contain one narrower and one broader line with an intensity ratio of roughly 2:1, while (2) the stoichiometric ratio of Se$_{out}$ and Se$_{in}$ nuclei is 2:1, and (3) a penetration depth of $\gtrsim 80\,\mu$m can be expected for all samples[1]. An angular dependence of the line shifts is expected from the non-cubic coordination symmetry of the Se$_{in}$ and Se$_{out}$ sites. The qualitative differences and similarities in the spectra will be quantified and interpreted in the following sections.

In the supplement of Ref. [Muk15], a single ^{77}Se NMR line with a field-*independent* linewidth of $\sim$12 kHz is reported for a Bi$_2$Se$_3$ single crystal. We suggest that the authors observed only Se$_{out}$, while Se$_{in}$ was missing, probably due to noise. The ^{77}Se powder spectrum reported in Ref. [Tay12] could not distinguish the two ^{77}Se signals due to their large field-independent linewidths (cf. Sec. 5.4 and [Muk15]) and the low applied magnetic field of 7.05 T.

5.2.3 Experimental details

The two ^{77}Se lines have been excited individually and the corresponding spectra have been put together subsequently.[2] In all cases, spin echo pulse sequences have been used with $\pi/2$ pulse lengths of 5 to 7 µs and pulse separation $\tau = 15$ µs. The individual signals have been acquired via Fourier transforms of the second halves of the echoes.

For determining the relative intensity ratio of the signals we have multiplied the measured signal intensities $M_{SE}(2\tau)$ for a certain pulse separation time τ with $e^{(2\emptyset)^2/(2T_{2G}^2)}$. The echo decay curves and the Gaussian decay constants T_{2G}s extracted from them are shown in section 5.5.

For the absolute intensity estimation, we have measured the ^{77}Se spectrum of an H$_2$SeO$_3$

---

1 Our Cu-doped crystals have comparable charge carrier densities n and the undoped Bi$_2$Se$_3$ crystal is expected to have $\sim$10 times smaller n (and hence a bigger penetration depth).

2 The acquired individual signal strengths have been corrected for the number of scans first.

powder sample[1] with the same coil and probe as the $Cu_{0.15}Bi_2Se_3$ single crystal. In order to make the signal strengths of the two samples comparable, the same spin echo pulse sequence has been used and the signal strengths have been corrected for differences in the quality factor Q, receiver gain, spin echo decay time and longitudinal relaxation effects. In a final step the corrected intensities have been normalized by the total number of selenium atoms in the samples and compared to each other.[2]

5.3 Shifts and longitudinal relaxation

5.3.1 Results

Table 5.2 compares shifts K_0 and longitudinal relaxation times T_1 of Se_{out} and Se_{in} signals measured in the various single crystal samples oriented as $c \parallel B_0$ and $c \perp B_0$. While all Cu-doped samples (except for the aged $Cu_{0.15}Bi_2Se_3$) show similar shifts and relaxation times, the undoped Bi_2Se_3 crystal exhibits significantly different shift and $\sim$10 times slower relaxation (for both signals and orientations). For the $Cu_{0.15}Bi_2Se_3$ sample, all T_1 and K_0 values have shifted closer to the Bi_2Se_3 values upon aging. We note that the values depend on the crystal orientation in the magnetic field and will take a closer look at this next.

Angular dependence
The dependence of the Se_{out} shift (K_0^{out}) on the polar angle θ (between the crystal c-axis and the applied field B_0) has been measured and an excellent agreement of the data with $K_0(\theta) = K_{iso} + K_{aniso}(3\cos^2\theta - 1)/2$ has been found. Representative example curves for the undoped and one Cu-doped Bi_2Se_3 crystal are depicted in Fig. 5.5. This angular dependence corresponds to an axially symmetric shift tensor, i.e., $\eta = 0$, which has been confirmed also by changing the azimuthal angle ϕ at a fixed $\theta = 90°$ for $Cu_{0.1}Bi_2Se_3$ (cf. inset of Fig. 5.5).

The values of the isotropic shift K_{iso} and the shift anisotropy K_{aniso} of the two ^{77}Se signals are summarized in the two panels in Fig. 5.6, respectively. Here, the values for Se_{in} are plotted against the ones for Se_{out} with the Cu-doping x being an intrinsic parameter. We note that for all samples the isotropic shift of Se_{in} (Se_{out}) is negative (positive) and that the absolute value $|K_{iso}^{in}|$ is always bigger than $|K_{iso}^{out}|$. The shift anisotropies of both Se_{in} and Se_{out} are positive. For both, K_{iso} and K_{aniso} a linear dependence between Se_{in} and Se_{out} values, i.e., $K^{in} = a + bK^{out}$, is found, with similar slope values $b_{iso} = -3.6 \pm 0.7$ and $b_{aniso} = -2.8 \pm 0.2$. The intersection points with the vertical axis are $a_{iso} = 440 \pm 150$ ppm and $a_{aniso} = 860 \pm 60$ ppm. Upon doping with Cu the isotropic shift of Se_{out} K_{iso}^{out} decreases and its shift anisotropy K_{aniso}^{out} increases, and the opposite is true for Se_{in}: K_{iso}^{in} increases (i.e., becomes less negative) and K_{aniso}^{in} decreases. The values determined for the aged

---

1   H_2SeO_3 is a nonconducting acid, hence it is expected that all ^{77}Se spins in the sample contribute to the measured NMR signal.
2   The total number of Se atoms has been obtained from the measured sample masses and assuming a formula unit mass of 1103.232×10^{-27} kg for $Cu_{0.15}Bi_2Se_3$ and 214.172×10^{-27} kg for H_2SeO_3. Since the H_2SeO_3 powder is hygroscopic, we considered an extreme scenario in which 10% of the sample mass is due to water, therefore we give a lower border of $\sim$25% above. In the case of a completely dry sample, we obtain that $\sim$28% of all ^{77}Se nuclei in $Cu_{0.15}Bi_2Se_3$ are excited.

$Cu_{0.15}Bi_2Se_3$ sample are again between the non-aged $Cu_{0.15}Bi_2Se_3$ and the Bi_2Se_3 values. For the K_{aniso}^{in} vs. K_{aniso}^{out} plot it is obvious that upon aging the values have shifted along the linear fit.

Comparing the T_1 values measured for $c \| B_0$ and $c \perp B_0$ in Tab. 5.2 we find for all samples smaller (bigger) T_1s for Se_{in} (Se_{out}) at $c \| B_0$ than at $c \perp B_0$. These relations can be seen better in Fig. 5.7 where the rates $1/T_1$ at perpendicular and parallel orientations are plotted against each other with Cu doping x being an intrinsic parameter. For both, Se_{in} and Se_{out}, we see that all samples lie more or less on one line passing through the coordinate origin, i.e., they all have similar rate anisotropies. The proportionality constant $T_1^{\|}/T_1^{\perp}$ (i.e., the slope of the linear fit) is 0.7±0.1 for Se_{in} and 1.6±0.1 for Se_{out}.

In Fig. 5.8 we have the relaxation rates of the inner and outer ^{77}Se signals in all $Cu_xBi_2Se_3$ crystals plotted against each other for $c \| B_0$ and $c \perp B_0$ (left and right, respectively). We find a direct proportionality between the inner and outer ^{77}Se rates with proportionality ratio T_1^{out}/T_1^{in} of 2.9±0.1 (1.45±0.20) for $c \| B_0$ ($c \perp B_0$).

Table 5.2: Shifts $K_0^{in(out)}$ and longitudinal relaxation times $T_1^{in(out)}$ of the Se_{in} (Se_{out}) NMR signals of $Cu_xBi_2Se_3$ single crystals with different Cu content x (0, 0.1, 0.125, 0.15 and 0.17) measured at two orientations of the crystal c-axis in the magnetic field B_0 at ambient conditions and 17.6 T.

	$c \| B_0$		$c \perp B_0$	
x	K_0^{in} [ppm]	K_0^{out} [ppm]	K_0^{in} [ppm]	K_0^{out} [ppm]
0.00	-63±7	410±7	-605±12	144±7
0.10	-201±5	477±3	-379±8	71±3
0.125	-182±5	476±5	-315±10	60±5
0.15 (aged)	-175±10 (-150±5)	475±5 (452±5)	-400±10 (-486±5)	86±5 (123±5)
0.17	-178±7	480±7	-388±27	80±5
x	T_1^{in} [s]	T_1^{out} [s]	T_1^{in} [s]	T_1^{out} [s]
0.00	1.4±0.3	4.8±0.3	2.0±0.3	3.0±0.3
0.10	0.13±0.02	0.43±0.02	0.17±0.02	0.23±0.02
0.125	0.10±0.02	0.29±0.02	0.10±0.05	0.20±0.02
0.15 (aged)	0.13±0.01 (0.36±0.02)	0.40±0.03 (1.10±0.12)	0.24±0.03 (0.44±0.11)	0.21±0.02 (0.67±0.05)
0.17	0.14±0.01	0.35±0.01	0.17±0.02	0.27±0.01
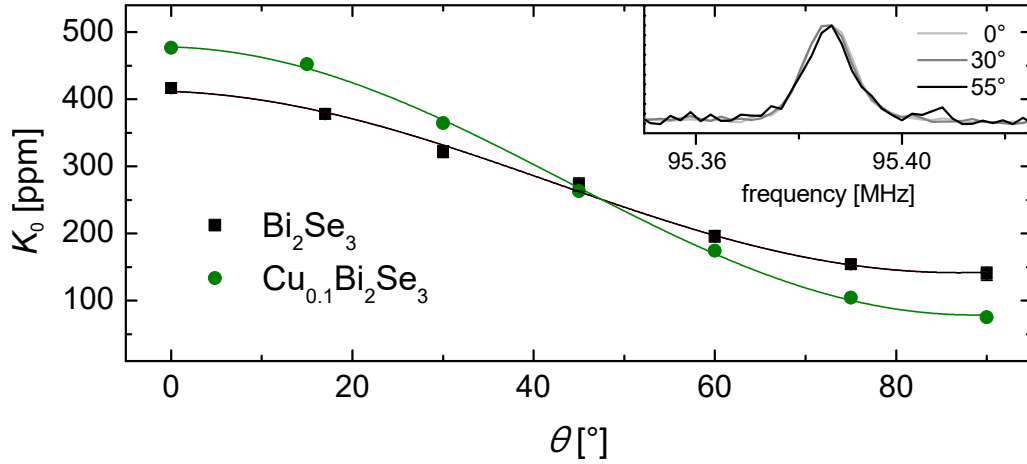
Figure 5.5: Shift K_0 of the $\mathrm{Se_{out}}$ line center measured in the $\mathrm{Bi_2Se_3}$ and $\mathrm{Cu_{0.1}Bi_2Se_3}$ single crystals at 17.6 T as a function of polar angle θ. Solid lines are fits to $K_0(\theta) = K_{\mathrm{iso}} + K_{\mathrm{aniso}}(3\cos^2\theta - 1)/2$. Inset shows the $\mathrm{Se_{out}}$ NMR line measured in the $\mathrm{Cu_{0.1}Bi_2Se_3}$ single crystal at fixed polar angle $\theta = 90°$ (i.e., $c \perp B_0$) and three different azimuthal angles ϕ (0°, 30° and 55°) at ambient conditions and 11.7 T.

Temperature dependence

The ^{77}Se NMR parameters for the $\mathrm{Bi_2Se_3}$ and $\mathrm{Cu_{0.15}Bi_2Se_3}$ (non-aged) samples have been measured at two additional temperatures (200 K and 250 K, for $c \| B_0$) and compared to the room temperature data. While no change in the line shifts has been found within the error (see spectra in Appendix D), for both samples and signals we find T_1 increasing with decreasing T, cf. Fig. 5.9. The Korringa products T_1T are plotted against temperature in the insets of Fig. 5.9. For $\mathrm{Bi_2Se_3}$ T_1T is nearly constant within the considered temperature range, however, for $\mathrm{Cu_{0.15}Bi_2Se_3}$, it is $\sim$2 times bigger at 200 K than at room temperature (for both signals in each case).

In Fig. 5.10 we plot the relaxation rates of the inner and outer ^{77}Se lines from Fig. 5.9 against each other, with the temperature as an intrinsic parameter. For $\mathrm{Cu_{0.15}Bi_2Se_3}$ we find a proportionality, similarly to Fig. 5.8, however, with a bigger proportionality ratio $T_1^{\mathrm{out}}/T_1^{\mathrm{in}}$ of 3.9±0.3. For $\mathrm{Bi_2Se_3}$ a proportionality as $T_1^{\mathrm{out}}/T_1^{\mathrm{in}} = 3.7\pm0.7$ can be fitted, however, the variance of the values, as well as their uncertainties, are much bigger[1].

---

1   The longitudinal relaxation measurements for $\mathrm{Bi_2Se_3}$ were more time consuming due to the 10 times longer T_1s. In order to save measurement time, the relaxation curves have been acquired with a poorer signal-to-noise ratio.
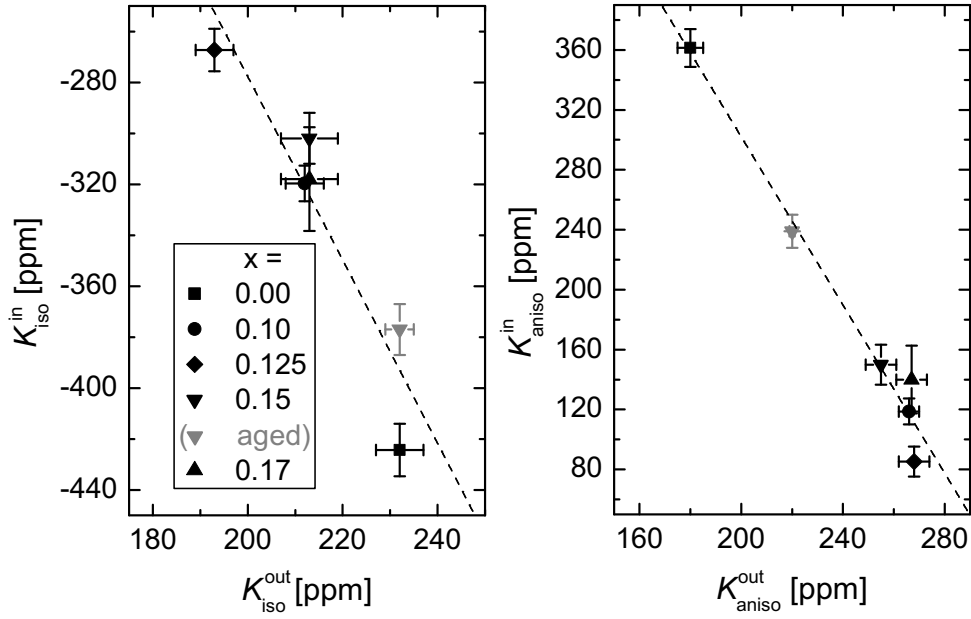
Figure 5.6: ^{77}Se isotropic shifts K_{iso} (shown left) and shift anisotropies K_{aniso} (shown right) of Se$_{\mathrm{in}}$ (K^{in}) plotted against the corresponding values of Se$_{\mathrm{out}}$ (K^{out}) for Cu$_x$Bi$_2$Se$_3$ single crystals with various Cu content x (see legend). Values for the aged Cu$_{0.15}$Bi$_2$Se$_3$ sample are shown in gray. Dashed lines are linear fits.

5.3.2 Discussion

The measured K and T_1 values of the ^{77}Se signals reflect the charge carrier density levels of the studied samples. This interpretation is supported by several facts.

- We find similar K and T_1 values for all Cu-doped samples (except for the aged Cu$_{0.15}$Bi$_2$Se$_3$), all of which are expected to have similar carrier densities.

- In comparison to the Cu-doped samples, the undoped Bi$_2$Se$_3$ sample, having at least one order of magnitude smaller charge carrier density, exhibits 10 times slower relaxation and significantly different shifts of both ^{77}Se signals.

- The measured ^{77}Se T_1s in the Bi$_2$Se$_3$ sample are of few seconds, i.e., too short for an insulator, and hence point to the presence of a coupling of the nuclear spins to itinerant electrons. A significant electron doping level in our Bi$_2$Se$_3$ sample has been confirmed by ^{209}Bi NMR measurements by Robin Guehne yielding $^{209}T_1 \sim 10\,\mathrm{ms}$ [Gue], in agreement with ^{209}Bi NMR data on naturally doped Bi$_2$Se$_3$ samples with known charge carrier density n of at least $10^{19}\,\mathrm{cm}^{-3}$ from Ref. [Nis13] (reporting $^{209}T_1$ of 30 ms for $n = 1.35 \times 10^{19}\,\mathrm{cm}^{-3}$ and up to 100 ms for smaller n at 295 K). This estimate has been moreover confirmed by a comparison of Hall constants and ^{209}Bi NMR quadrupole splittings in various Bi$_2$Se$_3$ samples, performed by Robin Guehne [Gue], yielding that our Bi$_2$Se$_3$ single crystal must have a charge carrier density of 2×10^{19} to $5 \times 10^{19}\,\mathrm{cm}^{-3}$.
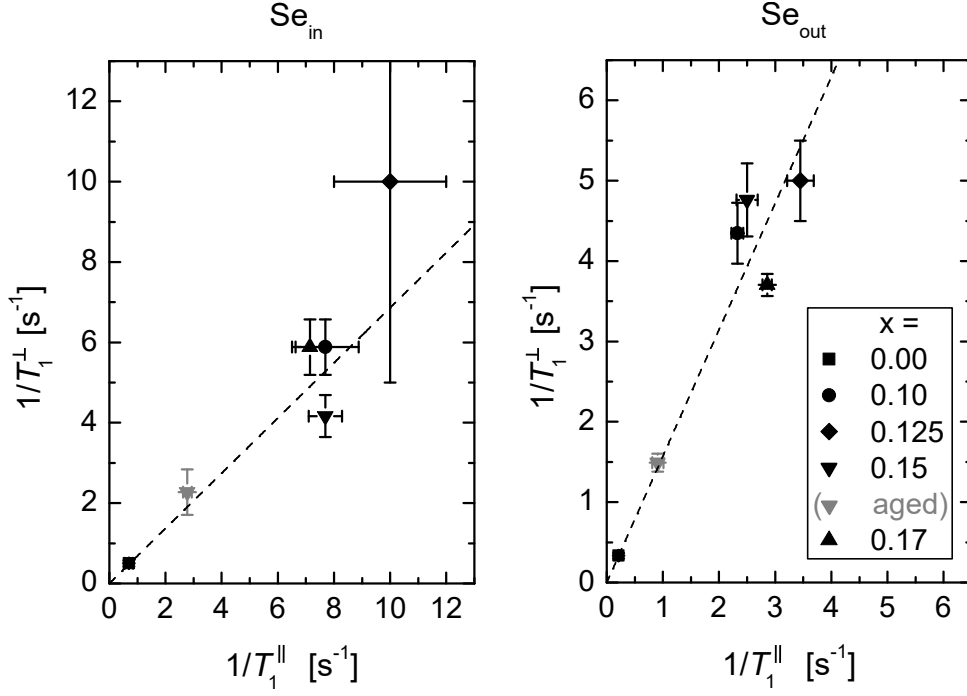
Figure 5.7: ^{77}Se longitudinal relaxation rates $1/T_1^\perp$ and $1/T_1^\parallel$ measured at $c \perp B_0$ and $c \parallel B_0$, respectively and plotted against each other for Se$_{in}$ and Se$_{out}$ (left and right plot, respectively) in Cu$_x$Bi$_2$Se$_3$ single crystals with various Cu content x (see legend). Values for the aged Cu$_{0.15}$Bi$_2$Se$_3$ sample are shown in gray. Dashed lines are linear fits.

- Upon aging Cu$_{0.15}$Bi$_2$Se$_3$ has lost its superconductivity while both its K and T_1 values have changed towards the Bi$_2$Se$_3$ values. Both phenomena can be interpreted as a decrease of n. Remember that Hor et al. [Hor10] report on a superconducting Cu$_{0.12}$Bi$_2$Se$_3$ sample with $n \simeq 2 \times 10^{20}$ cm^{-3} while Nisson et al. [Nis13] report on a Cu$_{0.12}$Bi$_2$Se$_3$ sample lacking superconductivity with significantly smaller $n = 2.5 \times 10^{19}$ cm^{-3}. Note that we have checked and found no changes of K and T_1 in the Bi$_2$Se$_3$ sample, which was stored and measured under the same conditions as the Cu$_{0.15}$Bi$_2$Se$_3$ one.

The measured shift values are *total* shifts containing chemical shift (independent on n) and Knight shift (dependent on n) contributions which cannot be separated in this study. In order to separate the n-dependent from the n-independent component, one would need a set of samples with a wide range of well-defined carrier concentrations, e.g., like in [Lel73]. We expect the chemical shift contribution to be nearly the same in all Cu$_x$Bi$_2$Se$_3$ samples since their lattice parameters are very similar, and hence the Knight shift contribution to be the one responsible for the shift differences among the samples.

The nature of Knight shifts in the systems under study can be a quite complex interplay of contact and non-contact contributions like orbital hyperfine interactions and core-polarization, and spin-orbit-coupling effects [Yes12]. The model calculation of the *contact* Knight shift in Bi$_2$Se$_3$ (due to contact hyperfine interaction only) in Ref. [Geo16] showed that it has an unconventional n-independent "interband" part (due to electronic transitions between the valence and conduction bands) next to the expected n-dependent "intraband"
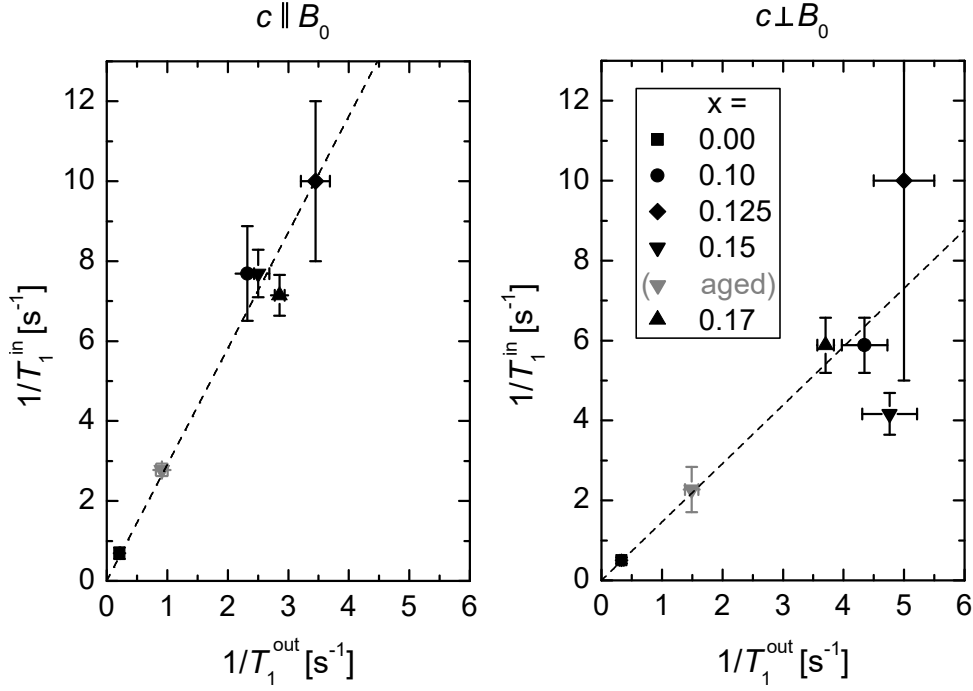
Figure 5.8: ^{77}Se longitudinal relaxation rates $1/T_1^{\mathrm{in}}$ (of Se$_{\mathrm{in}}$) vs. $1/T_1^{\mathrm{out}}$ (of Se$_{\mathrm{out}}$) measured in Cu$_x$Bi$_2$Se$_3$ single crystals with various Cu content x (see legend) at $c \parallel B_0$ and $c \perp B_0$ (left and right plot, respectively). Values for the aged Cu$_{0.15}$Bi$_2$Se$_3$ sample are shown in gray. Dashed lines are linear fits.

part (proportional to the density of states at the Fermi energy). This prediction cannot be verified without knowing the chemical shift contribution to our experimental shifts[1], however, its consequences for the ^{77}Se linewidths, which are in agreement with our data, will be discussed in the next section.

The more exact tight-binding theory of the Knight shifts in Bi$_2$Se$_3$ and Bi$_2$Te$_3$ from 2016 [Bou16] (focused on the *n*-dependent parts of the contact, dipolar, core-polarization, and orbital shifts) yields a rather complex picture where Se$_{\mathrm{in}}$ shifts are dominated by dipolar interactions and Se$_{\mathrm{out}}$ shifts - by orbital currents, and the strong spin-orbit coupling leads to unconventional shift contributions. We will compare our experimental findings with some of its predictions below.

The measured total shift tensor is axially symmetric. An axially symmetric chemical shift tensor is in agreement with the local coordination symmetry of the Se$_{\mathrm{in}}$ and Se$_{\mathrm{out}}$ sites in the crystal lattice. Upon doping, both the isotropic shift K_{iso} and the shift anisotropy K_{aniso} change, cf. Fig. 5.6, pointing to an axially symmetric Knight shift tensor (as predicted in [Bou16]). Interestingly, the left plot in Fig. 5.6 reveals that the *isotropic n-dependent Knight shift* for Se$_{\mathrm{in}}$ increases while the one for Se$_{\mathrm{out}}$ decreases with increasing *n*. The opposite must be true for the *n-dependent Knight shift anisotropies* for Se$_{\mathrm{in}}$ and Se$_{\mathrm{out}}$ (decreasing and increasing, respectively), as one can see in the right plot of Fig. 5.6. These findings agree with the theoretical predictions for the *n*-dependent Knight shifts (for

---

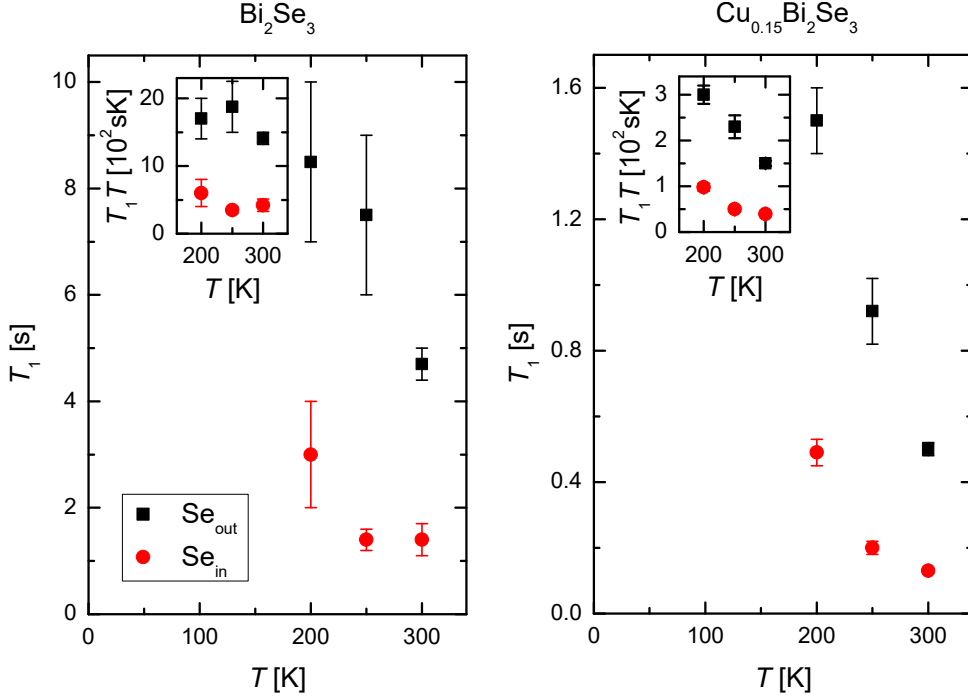1   First-principles calculations of chemical shifts in Bi$_2$Se$_3$ have not been attempted to this day.

Figure 5.9: Longitudinal relaxation times T_1 as a function of temperature T for the ^{77}Se signals due to Se_{out} and Se_{in} in Bi_2Se_3 (left) and $Cu_{0.15}Bi_2Se_3$ (non-aged, right) oriented as $c \parallel B_0$ at 17.6 T. Insets show corresponding Korringa products T_1T.

$2 \times 10^{19}\,\text{cm}^{-3} < n < 2 \times 10^{20}\,\text{cm}^{-3}$) from [Bou16], except for the Se_{in} isotropic shift (predicted to decrease with increasing n).

The slope of the linear dependence between Se_{in} and Se_{out} shifts $K^{in} = a + bK^{out}$ (cf. Fig. 5.6) infers a constant Knight shift ratio of the two sites. A proportionality of the n-dependent Knight shifts of Se_{in} and Se_{out} could mean that both selenium sites couple with the same electronic susceptibility but with different (in magnitude and sign) hyperfine coupling constants. This thesis is supported also by the proportionality of the relaxation rates of Se_{in} and Se_{out} ($T_1^{in}/T_1^{out} = $ const., cf. Fig. 5.8). It is obvious that the magnitude of the hyperfine coupling strength of Se_{in} is bigger than the one of Se_{out} (for Se_{in} exhibiting always bigger shift changes and bigger relaxation rates than Se_{out}). Within the experimental range of carrier densities ($\sim 2 \times 10^{19}$ to $2 \times 10^{20}\,\text{cm}^{-3}$) the theoretical isotropic and anisotropic shifts for Se_{in} and Se_{out} in [Bou16] change linearly, however, the Se_{in}/Se_{out} proportionality ratios do not agree with the experiment.

There is a much more pronounced temperature dependence of T_1 in the $Cu_{0.15}Bi_2Se_3$ crystal than in the undoped Bi_2Se_3, cf. Fig. 5.10, pointing to a different electronic behavior, which is not surprising, since the samples have significantly different charge carrier densities. Nevertheless, the rate anisotropies and the ratios T_1^{in}/T_1^{out} are the same in both samples, confirming the thesis that the relaxation mechanisms in both samples are the same (dominated by hyperfine coupling of the nuclei to itinerant electrons). In order to understand the temperature dependence better, one would need data from a much bigger temperature range, however, these are very time-consuming measurements that go beyond the scope of this work.
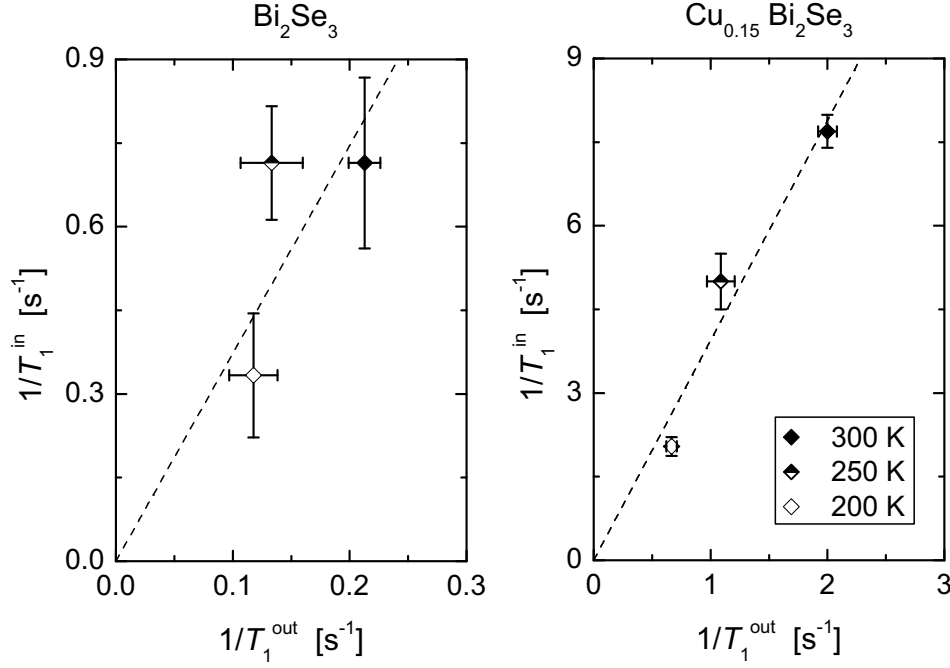
Figure 5.10: ^{77}Se longitudinal relaxation rates $1/T_1^{\mathrm{in}}$ (of Se$_{\mathrm{in}}$) vs. $1/T_1^{\mathrm{out}}$ (of Se$_{\mathrm{out}}$) taken from Fig. 5.9 with T as an intrinsic parameter (see legend) for Bi$_2$Se$_3$ and Cu$_{0.15}$Bi$_2$Se$_3$ single crystals oriented as $c \parallel B_0$ (left and right plot, respectively). Dashed lines are linear fits.

5.3.3 Experimental details

The center positions of the Se$_{\mathrm{in}}$ and Se$_{\mathrm{out}}$ NMR lines K_0 have been extracted from Gaussian fits. The values of the isotropic shift K_{iso} and the shift anisotropy K_{aniso} of the two ^{77}Se signals have been extracted partly from fits to measured angular dependences[1] and partly from $K_{\parallel/\perp}$ values in Tab. 5.2 using the relationships $K_{\mathrm{iso}} = (K_\parallel + 2K_\perp)/3$ and $K_{\mathrm{aniso}} = 2(K_\parallel - K_\perp)/3$.

For the determination of T_1 values saturation or inversion recovery pulse sequences have been used and a single exponential dependence of the form $M(t) = M_0 \left(1 - q\mathrm{e}^{-\mathrm{t}/\mathrm{T}_1}\right)$ has been fitted to the data, cf. Eq. 3.15.

For the low-temperature measurements we have used the same set up (i.e., cryogenic probe, cryostat, 17.6 T superconducting magnet, and spectrometer) as for the room temperature measurements performed beforehand. Before cooling we acquired spectra at room temperature and found that the line positions in both Bi$_2$Se$_3$ and Cu$_{0.15}$Bi$_2$Se$_3$ were unchanged in comparison to the earlier room temperature measurements.

---

1   Angular dependences have been measured for Se$_{\mathrm{out}}$ in all single crystals except for Cu$_{0.17}$Bi$_2$Se$_3$ and for Se$_{\mathrm{in}}$ in Cu$_{0.1}$Bi$_2$Se$_3$ and the aged Cu$_{0.15}$Bi$_2$Se$_3$ sample.

5.4 Linewidths

5.4.1 Results

The measured linewidths Λ of the Se_{out} and Se_{in} NMR signals in $Cu_xBi_2Se_3$ (x = 0, 0.1, 0.125, 0.15, 0.17) single crystals oriented as $c \parallel B_0$ and $c \perp B_0$ are summarized in Tab. 5.3.[1] We find Se_{in} linewidths between 20 and 31 kHz and Se_{out} linewidths between 10 and 15 kHz. Note that there is no change in the linewidths of $Cu_{0.15}Bi_2Se_3$ upon aging.

Angular dependence

The values for $c \perp B_0$ ($\theta = 90°$) are only slightly bigger than the ones for $c \parallel B_0$ ($\theta = 0°$), cf. Tab. 5.3. The angular dependence of the Se_{out} linewidth is shown in Fig. 5.11. While for Bi_2Se_3 there is a clear maximum (14 ± 1 kHz) near $\theta = 45°$, for the remaining samples there is no pronounced maximum within the measurement accuracy.

Temperature dependence

No change of the linewidths of both signals upon varying temperature has been found in the range from 200 K to room temperature (for Bi_2Se_3 and $Cu_{0.15}Bi_2Se_3$ at $c \parallel B_0$, cf. subsection 5.3.3 for experimental details).

Dipolar linewidths

The dipolar linewidths (i.e., full widths at half maximum) Λ_{dip} of the Se_{in} and Se_{out} NMR signals in Bi_2Se_3 have been calculated[2] for $c \parallel B_0$ and $c \perp B_0$ orientations and are presented in Tab. 5.4. The calculated values are more than 10 times smaller than the linewidths measured at 17.6 T. This discrepancy might be due to a large magnetic linewidth

Table 5.3: Linewidths $\Lambda^{in(out)}$ of the Se_{in} (Se_{out}) NMR signals of $Cu_xBi_2Se_3$ single crystals with different Cu content x (0, 0.1, 0.125, 0.15 and 0.17) measured at two orientations of the crystal c-axis in the magnetic field B_0 at ambient conditions and 17.6 T.

	$c \parallel B_0$		$c \perp B_0$	
x	Λ^{in} [kHz]	Λ^{out} [kHz]	Λ^{in} [kHz]	Λ^{out} [kHz]
0.00	24.0 ± 0.7	10.1 ± 0.4	24.3 ± 0.7	10.9 ± 0.1
0.10	21.0 ± 2.0	12.0 ± 1.0	31.0 ± 5.0	13.0 ± 1.2
0.125	23.7 ± 1.4	12.2 ± 1.2	26.0 ± 1.5	13.1 ± 0.8
0.15 (aged)	20.6 ± 1.2 (21.9 ± 1.7)	10.8 ± 0.4 (10.8 ± 0.9)	24.7 ± 3.5 (25.2 ± 1.6)	12.4 ± 1.2 (11.4 ± 0.9)
0.17	25.9 ± 0.7	12.6 ± 0.4	28.8 ± 3.5	14.7 ± 1.6

---

1   The value Λ corresponds to the full width at half maximum of a Gaussian function fitted to the measured NMR signal.

2   For details see Appendix G. Note that $\sim 99\%$ of the linewidth is due to ^{77}Se-^{209}Bi dipole-dipole interactions and only $\sim 1\%$ is due to ^{77}Se-^{77}Se coupling, since ^{77}Se has a much smaller spin and very low abundance in comparison to the 100%-abundant spin-9/2 ^{209}Bi nuclei.
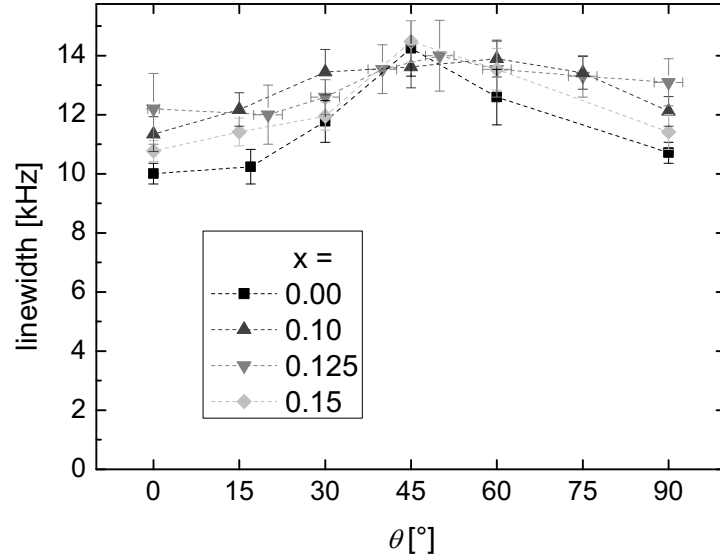
Figure 5.11: Se$_{out}$ linewidths of Cu$_x$Bi$_2$Se$_3$ single crystals with different Cu content x (see legend) measured as a function of the polar angle θ at ambient conditions and 17.6 T.

component. In order to verify this, we have measured the magnetic field dependence of the linewidths.

Magnetic field dependence

Fig. 5.12 shows the magnetic field dependence of the Se$_{in}$ and Se$_{out}$ linewidths in Bi$_2$Se$_3$ and Cu$_{0.1}$Bi$_2$Se$_3$. We find similar dependences for both samples (cf. green and black symbols) and only minor differences upon changing the crystal orientation in the magnetic fields (cf. left and right plots). Both, the Se$_{in}$ and Se$_{out}$ linewidths are surprisingly weakly dependent on the magnetic field, with the Se$_{in}$ linewidth being nearly field-independent. We would like to separate the field-independent component of the linewidth an compare it with the dipolar one. Since the measured signals are Gaussian shaped, their second moment is proportional to the square of the linewidth Λ^2. We assume that there are two contributions to the total second moment: a field independent one (proportional to the

Table 5.4: Calculated Se$_{in}$ (Se$_{out}$) linewidths $\Lambda_{dip}^{in(out)}$ due to dipole-dipole coupling between ^{77}Se spins sitting on the inner (outer) selenium site in the Bi$_2$Se$_3$ lattice and the surrounding ^{209}Bi and ^{77}Se spins for $c \parallel B_0$ and $c \perp B_0$.

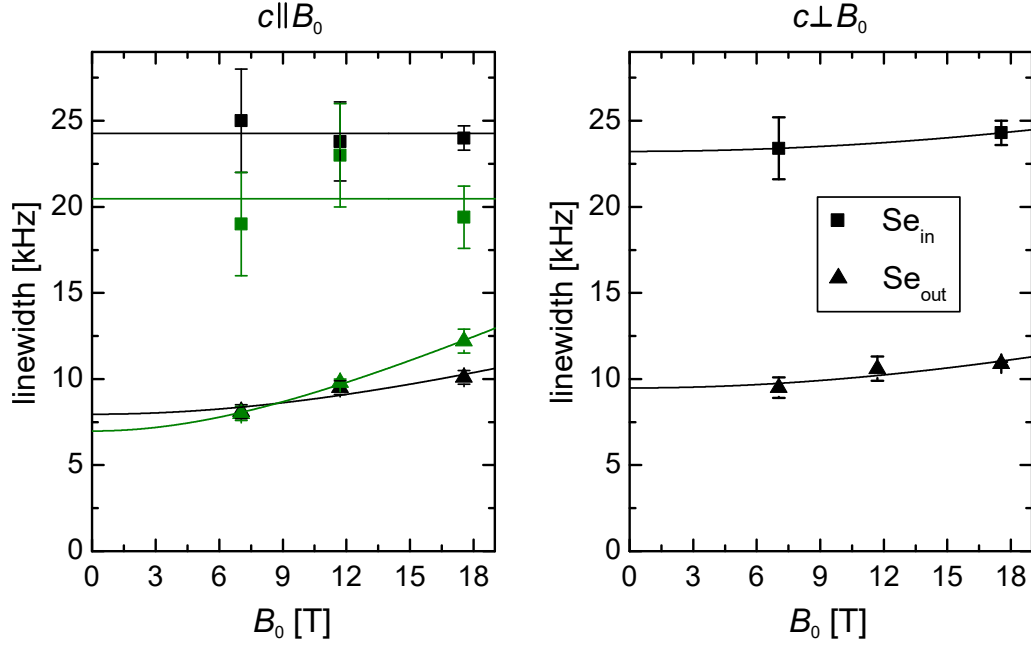| $c \parallel B_0$		$c \perp B_0$	
Λ_{dip}^{in} [kHz]	Λ_{dip}^{out} [kHz]	Λ_{dip}^{in} [kHz]	Λ_{dip}^{out} [kHz]
0.6	0.7	1.6	1.3

Figure 5.12: Magnetic field dependence of Se_{in} (squares) and Se_{out} (triangles) linewidths Λ measured for Bi_2Se_3 (black symbols) and $Cu_{0.1}Bi_2Se_3$ (green symbols) single crystals oriented as $c \parallel B_0$ (left) or $c \perp B_0$ (right). Solid lines are fits to $\Lambda^2 = \Lambda_0^2 + [\lambda B_0]^2$ (see text).

square of a field-independent linewidth Λ_0^2) and a field-dependent one (proportional to B_0^2). Making use of the additive property of second moments and assuming a Gaussian-like field independent contribution, we fit the function $\Lambda^2 = \Lambda_0^2 + [\lambda B_0]^2$ to the data and find a good agreement (cf. solid lines in Fig. 5.12). The extracted field-independent linewidths are summarized in Tab. 5.5. Note that they are one order of magnitude bigger and have a much smaller anisotropy than the dipolar linewidths. The proportionality constant in the field-dependent contribution to the Se_{out} linewidth λ is $\lesssim 0.4\,kHz/T$ for Bi_2Se_3 and 0.57 ± 0.02 kHz/T for $Cu_{0.1}Bi_2Se_3$.

Table 5.5: Field-independent contributions $\Lambda_0^{in(out)}$ to the Se_{in} (Se_{out}) linewidths in Bi_2Se_3 $\{Cu_{0.1}Bi_2Se_3\}$ oriented as $c \parallel B_0$ or $c \perp B_0$.

$c \parallel B_0$		$c \perp B_0$	
Λ_0^{in} [kHz]	Λ_0^{out} [kHz]	Λ_0^{in} [kHz]	Λ_0^{out} [kHz]
24 ± 1 $\{20.5\pm1.3\}$	8.0 ± 0.6 $\{7.0\pm0.6\}$	23 ± 1	9.5 ± 0.6

5.4.2 Discussion

Field-*independent* linewidths in excess of what might be expected from internuclear dipole-dipole coupling for the non-quadrupolar (spin-1/2) ^{77}Se nuclei point immediately to indirect internuclear coupling mediated by electrons [Abr61].

We expect the field-independent linewidths to be determined by indirect coupling to ^{209}Bi spins, neglecting the coupling to ^{77}Se spins due to their much lower abundance and smaller spin. The fact that the measured field-independent linewidths for Se$_{in}$ are almost three-time larger than for Se$_{out}$ (in contrast to the calculated dipolar linewidths) can be explained with the stronger hyperfine coupling of Se$_{in}$ and the fact that Se$_{in}$ has twice as many nearest neighboring ^{209}Bi nuclei.

The indirect coupling tensor $\mathcal{J}_{AB}$ in the bilinear relation $\boldsymbol{I}_A\cdot\mathcal{J}_{AB}\cdot\boldsymbol{I}_B$ of two spins $\boldsymbol{I}_A$ and $\boldsymbol{I}_B$ can be separated into a traceless part $\mathcal{J}-\mathcal{I}J$ and a diagonal part $\mathcal{I}J$, where $J = 1/3\,\mathrm{tr}\,(\mathcal{J})$ and $\mathcal{I}$ is the identity matrix [Abr61]. According to [Blo55] the two parts will contribute independently to the second moment of the NMR line.

In some special cases, e.g., as shown in [Blo55] in the so-called spheric approximation, the traceless part of the tensor is pseudodipolar, i.e., having the same angular dependence as the dipolar coupling of nuclear spins [Abr61]. Since magic angle spinning ^{77}Se NMR experiments on Bi$_2$Se$_3$ powders do not result in significant narrowing or appearance of spinning side bands (cf. Fig. F.1 and [Tay12]), one can exclude a significant pseudodipolar contribution to the indirect coupling in Bi$_2$Se$_3$. A traceless part of the coupling tensor, however, cannot be excluded in general.

The diagonal part of the coupling tensor leads to a scalar exchange coupling of the form $J\boldsymbol{I}_A\cdot\boldsymbol{I}_B$. The theoretical second moment due to scalar exchange coupling alone contributing to the width of a particular ^{77}Se resonance line (i) is given by [Abr61]

$$\left\langle \Delta\omega^2\right\rangle_i = \sum_j \frac{I_j(I_j+1)}{3\hbar^2}J_{ij}^2 \tag{5.2}$$

(here $I_j = 9/2$ is the nuclear spin quantum number for ^{209}Bi) and is not dependent on the crystal orientation in the external magnetic field. In reality, the picture is probably more complicated due to the fact that each ^{209}Bi nucleus has a different resonance frequency (the ^{209}Bi spectrum consists of 9 distinct broad lines). For example, it is conceivable that the strong angular dependence of the ^{209}Bi spectrum is responsible for the angular dependence of the ^{77}Se linewidth in Bi$_2$Se$_3$ reaching a maximum in the vicinity of the magic angle, cf. Fig. 5.11, where all 9 ^{209}Bi lines overlap.

Unlike the shifts and T_1s, the field-independent linewidths are only weakly dependent on the charge carrier density[1] (even slightly smaller for the sample with ten-time bigger n), cf. Tab. 5.5. Such weak n-dependence of the indirect internuclear coupling has been predicted (for low-to-moderate doping) by a model calculation in [Geo16] and explained with the dominance of the Bloembergen-Rowland coupling over the Ruderman-Kittel-Kasuya-Yosida coupling in Bi$_2$Se$_3$. The model calculation is far from complete: it uses a simplified band model and includes contact hyperfine interaction only (excluding possibly significant [Bou16]

---

[1]   The fact that the measured linewidths do not change upon aging, in contrast to shifts and T_1s, supports this thesis.

contributions to the electron susceptibility from dipolar, core-polarization, and orbital interactions), estimating the contact hyperfine constants from comparison of calculated and measured isotropic Knight shifts. Nevertheless, it gives estimates for the Se_{in} linewidth in the right order of magnitude, thereby supporting the attribution of the measured field-independent linewidths to a strong indirect internuclear coupling. Interestingly, the calculated coupling tensor $\mathcal{J}$ is not diagonal, although an isotropic hyperfine (contact) interaction is assumed[1], but the off-diagonal elements are much smaller than the diagonal ones and $\mathcal{J}_{xx} = \mathcal{J}_{yy} \approx \mathcal{J}_{zz}$ so that the formula for the second moment (Eq. 5.2), valid for scalar exchange coupling, could be used.

The field-*dependent* part of the linewidths, which is significant ($\sim 0.5\,\text{kHz/T}$) for Se_{out}, signifies a distribution of shifts which could be due to impurities or disorder in the crystal lattice (e.g. selenium vacancies)[2]. As for the temperature-independence of the measured total linewidths - it complies with the theory of strong Bloembergen-Rowland coupling and also a field-dependent shift distribution is expected to be temperature-independent.

The postulated Bloembergen-Rowland-dominated indirect internuclear coupling may have implications for the carrier-mediated magnetism of topological materials, e.g., by anticipating bulk magnetic order even when the Fermi level lies inside the bulk gap. It will thus be interesting to determine its universality by conducting further experimental and theoretical studies in other topological materials.

A strong indirect coupling should also affect the ^{209}Bi NMR. Here, the coupling is dominated by ^{209}Bi-^{209}Bi interactions, but does not lead to exchange narrowing [Abr61] since the local symmetry at the Bi site causes a sizable (~ 140 to $170\,\text{kHz}$) quadrupole shift [Nis13; You12] of the ^{209}Bi nuclear levels, such that nuclear neighbors may not be able to participate in exchange if they are in different spin states. Furthermore, the quadrupole shift can vary from one nucleus to the next, due to strain caused by imperfections. As a result, the line broadening and spin echo behavior of ^{209}Bi NMR can be quite complicated and may depend on the impurity levels.

The ^{209}Bi NMR spectrum for our Bi_2Se_3 single crystal contains 9 lines from quadrupole splitting with very similar yet large linewidths [Gue], thereby showing that quadrupolar broadening does not dominate the individual linewidths. Field-dependent measurements on Bi_2Se_3 powder [Höf] yield a field-*independent* linewidth of about $46\pm7\,\text{kHz}$ for the ^{209}Bi central transition, in agreement with $46\pm2\,\text{kHz}$ measured in our single crystal at the magic angle and $9.4\,\text{T}$ by Robin Guehne [Gue]. This width strongly exceeds the estimated dipolar linewidth of $\sim 1.5\,\text{kHz}$, and hence must be caused by indirect coupling.

Unusually large ^{209}Bi linewidths have been noticed in previous works [Muk15; Nis13; Nis14; You12], but indirect coupling was not invoked as a possible origin. Besides, rather fast ^{209}Bi NMR spin echo decays were observed, in particular in the central region of the spectra, but could not be explained. Interestingly, the linewidth from Ref. [Nis13] increases with decreasing carrier concentration (larger linewidths for more homogeneous samples grown with excess Se). Most of these results appear compatible with a large indirect coupling among the ^{209}Bi nuclei in the presence of quadrupole interaction.

---

1   This fact is due to the strongly anisotropic *g*-factors in Bi_2Se_3.
2   The absence of paramagnetic Cu^{2+} impurities has been verified with EPR for the non-aged $Cu_{0.15}Bi_2Se_3$ sample (see Appendix E).

5.4.3 Experimental details

The linewidths Λ are full widths at half maximum, extracted from Gaussian fits to the measured signals: $G(f) = G_0 \exp\left[-\ln(16)(f - f_0)^2/\Lambda^2\right]$, derived from Eq. 3.20 with $\Lambda \equiv \sqrt{\ln 4}/(\pi T_{2G}^{*2})$ and the center of mass shifted to f_0.

For details related to the calculation of the full widths at half maximum due to dipolar coupling Λ_0 see Appendix G.

5.5 Spin echo decays

5.5.1 Results

Fig. 5.13 depicts spin echo decays of the Se$_{in}$ and Se$_{out}$ NMR signals measured in Bi$_2$Se$_3$ and Cu$_{0.15}$Bi$_2$Se$_3$ (non-aged). The decays in Cu$_{0.15}$Bi$_2$Se$_3$ are representative for all Cu-doped samples. The echo decays are always well described by Gaussian functions proportional to $\exp\left(-(2\tau)^2/2T_{2G}^2\right)$ (τ is the distance between the pulses, cf. dotted lines in Fig. 5.13). The extracted decay constants T_{2G} are summarized in Tab. 5.6. The Se$_{in}$ signal decays always ~ 2.1 times faster than Se$_{out}$. While all Cu-doped samples show similar T_{2G}s, the values for Bi$_2$Se$_3$ are roughly 2.5 times bigger. Note that we find no change in the echo decays of Cu$_{0.15}$Bi$_2$Se$_3$ upon aging. The decay constants measured for $c \parallel B_0$ are always ~ 1.2 times bigger than the values for $c \perp B_0$.
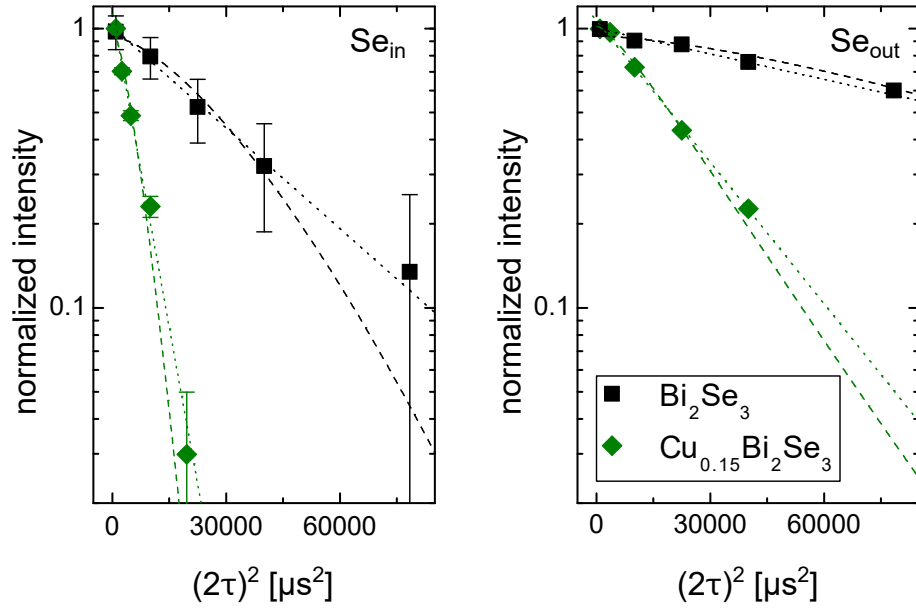

Figure 5.13: Spin echo decays of Se$_{in}$ (left) and Se$_{out}$ (right) signals of Bi$_2$Se$_3$ (black squares) and Cu$_{0.15}$Bi$_2$Se$_3$ (non-aged, green diamonds) single crystals oriented as $c \parallel B_0$ measured at ambient conditions and 17.6 T. Dotted lines are Gaussian fits proportional to $\exp\left(-(2\tau)^2/2T_{2G}^2\right)$. Dashed lines are fits to Eq. (5.4) with second moments taken from the field-independent linewidths Λ_0^{in} and Λ_0^{out}, respectively, of Bi$_2$Se$_3$ in Tab. 5.5 (see text).

Table 5.6: Spin echo decay times $T_{2G}^{in(out)}$ of the Se_{in} (Se_{out}) NMR signals of $Cu_xBi_2Se_3$ single crystals with different Cu content x (0, 0.1, 0.125, 0.15 and 0.17) measured at two orientations of the crystal c-axis in the magnetic field B_0 at ambient conditions and 17.6 T.

| x | $c \parallel B_0$ | | $c \perp B_0$ | |
	T_{2G}^{in} [μs]	T_{2G}^{out} [μs]	T_{2G}^{in} [μs]	T_{2G}^{out} [μs]
0.00	134±2	260±20	94±10	215±10
0.10	48±2	108±3	45±2	85±2
0.125	50±5	110±4	44±4	85±2
0.15 (aged)	54±2 (55±2)	113±4 (105±2)	35±5 (37±5)	99±5 (92±2)
0.17	45±1	109±1	42±2	85±1

Temperature dependence

Fig. 5.14 shows Gaussian decay constants as a function of temperature for Se_{in} and Se_{out} in Bi_2Se_3 and $Cu_{0.15}Bi_2Se_3$. While for Bi_2Se_3 we measure temperature-independent spin echo decays with T_{2G}s of 135 (255) μs for Se_{in} (Se_{out}), for $Cu_{0.15}Bi_2Se_3$ there is a significant increase in T_{2G} upon decreasing temperature for both signals. For $Cu_{0.15}Bi_2Se_3$ linear functions, i.e., $T_{2G} = a + bT$, fit the data well yielding $a = 115 \pm 20$ (260 ± 15) μs and $b = -0.21 \pm 0.08$ (-0.50 ± 0.06) μs/K for Se_{in} (Se_{out}).
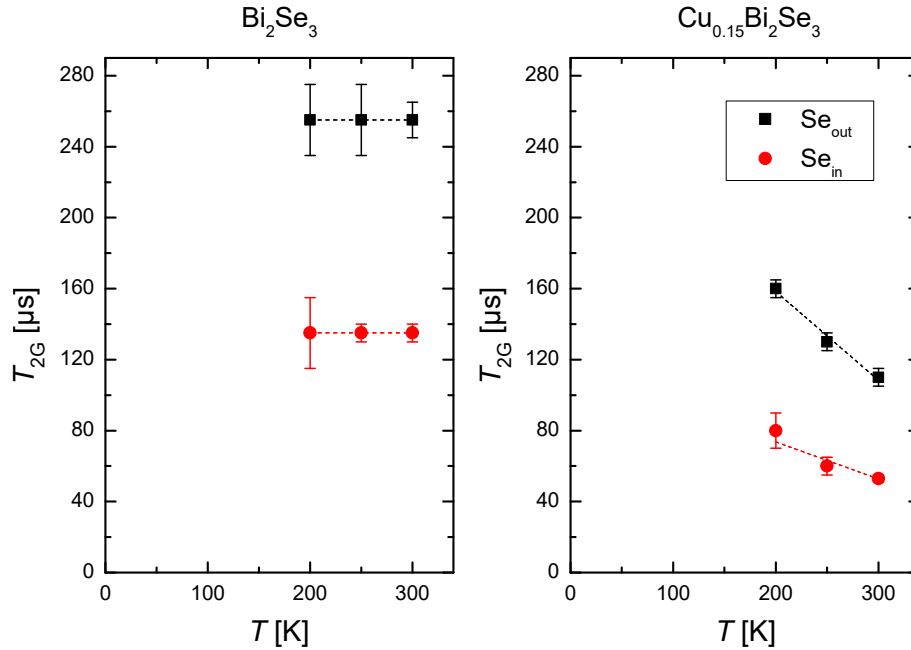

Figure 5.14: Spin echo decay constants T_{2G} (extracted from Gaussian fits) for the ^{77}Se signals due to Se_{out} and Se_{in} in Bi_2Se_3 (left) and $Cu_{0.15}Bi_2Se_3$ (non-aged, right) oriented as $c \parallel B_0$ at 17.6 T. Dashed lines are linear fits.

Table 5.7: Calculated Se$_{in}$ (Se$_{out}$) Gaussian decay constants $T_{2G,dip}^{in(out)}$ due to dipole-dipole coupling solely among Se$_{in}$ (Se$_{out}$) nuclear spins in Bi$_2$Se$_3$ for $c \parallel B_0$ and $c \perp B_0$.

$c \parallel B_0$		$c \perp B_0$	
$T_{2G,dip}^{in}$ [μs]	$T_{2G,dip}^{out}$ [μs]	$T_{2G,dip}^{in}$ [μs]	$T_{2G,dip}^{out}$ [μs]
4800	3000	4200	2300

Contributions due to homonuclear dipolar coupling

It is natural to compare the measured T_{2G}s of Se$_{in}$ (Se$_{out}$) to the values expected from homonuclear dipole-dipole coupling among Se$_{in}$ (Se$_{out}$) spins only. The homonuclear dipolar decay constants $T_{2G,dip}$ have been calculated for Bi$_2$Se$_3$, for $c \parallel B_0$ and $c \perp B_0$ orientations, and the resulting values are shown in Tab. 5.7. The calculated values are one order of magnitude bigger than the experimentally determined T_{2G}s. Moreover, in contrast to the experiments the calculations yield a slower decay for Se$_{in}$ than for Se$_{out}$, for both orientations. Solely the anisotropies of the calculated and measured T_{2G}s are similar.

Double resonance experiment

The coupling between Se$_{out}$ and Se$_{in}$ nuclei in Bi$_2$Se$_3$ has been checked with the following experiment. While observing a spin echo on Se$_{out}$, Se$_{in}$ has also been inverted with a π-pulse applied immediately after the π-pulse on Se$_{out}$. The echo maximum in this case was found to be $\sim 10\%$ smaller than in the case when Se$_{in}$ was not inverted. This additional spin echo decay effect must be due to Se$_{out}$-Se$_{in}$ coupling. Its decay constant T_{2G}^{out-in} can be roughly estimated assuming Gaussian decays and exploiting their property of additive second moments, i.e.,

$$\exp\left[-\frac{t^2}{2}\left(\frac{1}{(T_{2G}^{out})^2} + \frac{1}{(T_{2G}^{out-in})^2}\right)\right] \approx 0.9 \times \exp\left[-\frac{t^2}{2}\left(\frac{1}{(T_{2G}^{out})^2}\right)\right]. \tag{5.3}$$

The resulting value for T_{2G}^{out-in} is in the range 600-1000 μs, i.e., one order of magnitude smaller than expected from direct dipolar coupling between Se$_{out}$ and Se$_{in}$ ($T_{2G,dip}^{out-in} = 15$ ms for $c \perp B_0$).[1]

5.5.2 Discussion

We find Gaussian-like spin echo decays with decay constants T_{2G} significantly bigger than the inverse linewidths $T_{2G}^* = \sqrt{\ln 4}/(\pi \Lambda)$ for both ^{77}Se signals in all samples. This confirms an inhomogeneous broadening of the ^{77}Se lines, as suggested in the previous section. Since direct homonuclear dipolar coupling is far too weak to account for the echo decays, the question arises as to whether an indirect ^{77}Se-^{77}Se coupling mechanism can.

The double resonance experiment shows that there is indeed an enhanced, hence indirect, coupling between *unlike* ^{77}Se spins. A scalar exchange coupling J between *like* ^{77}Se nuclei would cause exchange *narrowing* [Abr61] (i.e., a slower echo decay) and hence can *not*

---

1   The crystal was oriented as $c \perp B_0$, hence $T_{2G}^{out} = 215$ μs was assumed.

explain the measured fast decays, however, a traceless coupling tensor $\mathcal{J}$ could.

Comparing T_{2G} with the inverse linewidths T_{2G}^* we find several puzzling differences:

(i) in contrast to the field-independent linewidths, the measured T_{2G}s show anisotropies very similar to the calculated dipolar ones,

(ii) while T_{2G}^* of a certain signal at a certain orientation is nearly the same in all samples, the corresponding T_{2G} is the same in all *Cu-doped* samples, but ~ 2.5 times bigger in Bi_2Se_3, and furthermore

(iii) we found no temperature dependence of T_{2G}^* in Bi_2Se_3 and $Cu_{0.15}Bi_2Se_3$, and of T_{2G} in Bi_2Se_3, whereas T_{2G} of both signals in $Cu_{0.15}Bi_2Se_3$ increases with decreasing temperature.

Summarizing, if the T_{2G}s are due to a tensorial indirect coupling between like ^{77}Se spins[1], then this coupling must be Ruderman-Kittel-Kasuya-Yosida-dominated (for being *n-* and *T*-dependent) and might be pseudodipolar (for having a dipolar-like anisotropy) - in contrast to the Bloembergen-Rowland-dominated and non-pseudodipolar ^{77}Se-^{209}Bi indirect coupling causing the field-independent linewidths. A full first-principles calculation of the indirect internuclear coupling in Bi_2Se_3 is needed to verify this hypothesis.

Another feasible spin-echo decay mechanism will be discussed next. It seems possible that ^{209}Bi spin flips, e.g., due to spin-lattice relaxation, will induce fluctuations of the local field at the ^{77}Se site via the ^{77}Se-^{209}Bi indirect coupling, thereby shortening the spin echo decay. In order to test this hypothesis we apply the Gaussian-approximation formalism model[2] described by Recchia et al. [Rec96]. In this formalism an effective longitudinal local magnetic field $h_z(t)$ is assumed to be characterized by an exponential time correlation function $g(t) = \langle (h_0)^2 \rangle \exp\left(-|t|/\tau_c\right)$ with correlation time τ_c and mean-square field $\langle (h_0)^2 \rangle$. We assume a single source of fluctuations and the mean-square field at ^{77}Se given by the ^{77}Se-^{209}Bi indirect coupling, and hence by the field-independent ^{77}Se linewidths Λ_0, i.e., $\gamma^2 \langle (h_0)^2 \rangle = (\pi \Lambda_0)^2 / \ln 4$. With this assumption we fit the data to the formula derived by Recchia et al. for the spin-echo decay

$$M(2\tau) = M_0 \times \exp\left[-\gamma^2 \langle (h_0)^2 \rangle \tau_c^2 \times \left\{ (2\tau)/\tau_c + 4e^{-(2\tau)/2\tau_c} - e^{-(2\tau)/\tau_c} - 3 \right\} \right], \quad (5.4)$$

cf. dashed lines in Fig. 5.13. The best fitting τ_c values are summarized in Tab. 5.8.

We notice that correlation times extracted from fits to the decays of the Se_{in} and Se_{out} signals (τ_c^{in} and τ_c^{out}) are the same within the error (although different $\gamma^2 \langle (h_0)^2 \rangle$ values have been put into the fits), supporting the idea of one source of fluctuations coupling differently with the two ^{77}Se sites. Note that all Cu-doped samples yield the same correlation time of $\sim 50\,\mu s$ ($\sim 40\,\mu s$) for $c \parallel B_0$ ($c \perp B_0$) and that it is one order of magnitude smaller than the correlation time for Bi_2Se_3 of $\sim 2\,ms$ ($\sim 1\,ms$). The correlation times for Bi_2Se_3 comply with the *non-selectively* excited $^{209}T_1$ value of $10\,ms$ measured in the same sample by Robin Guehne [Gue], since the single level lifetime for $I = 9/2$ is expected to be a factor of 10

---

1   The faster echo decay of the Se_{in} signal can be attributed again to larger hyperfine coupling.

2   At the time of the echo, the distribution of accumulated phase angles for the ensemble of nuclear spins is approximated as a Gaussian.

Table 5.8: Correlation times $\tau_c^{in(out)}$ extracted from fitting Eq. (5.4) to the spin echo decays of the Se$_{in}$ (Se$_{out}$) NMR signals of Cu$_x$Bi$_2$Se$_3$ single crystals with different Cu content x (0, 0.1, 0.125, 0.15 and 0.17) measured at two orientations of the crystal c-axis in the magnetic field B_0 at ambient conditions and 17.6 T. The amplitudes $\gamma^2\langle(h_0)^2\rangle$ in the fits were fixed to the second moments $(\pi\Lambda_0)^2/\ln 4$ corresponding to the field-independent linewidths $\Lambda_0^{in(out)}$ of Bi$_2$Se$_3$ {Cu$_{0.1}$Bi$_2$Se$_3$} from Tab. 5.5.

	$c \parallel B_0$		$c \perp B_0$	
x	τ_c^{in} [μs]	τ_c^{out} [μs]	τ_c^{in} [μs]	τ_c^{out} [μs]
0.00	2400±400	1900±500	850±350	1200±400
0.10	{50±15}	{50±40}	40±10	35±15
0.125	{45±10}	{50±25}	40±10	35±15
0.15	{95±25}	{45±30}	20±20	40±30
0.17	{50±10}	{50±30}	45±10	55±10

smaller [Sli10]. Tenfold shorter correlation times for the Cu-doped samples agree with an expected tenfold decrease in $^{209}T_1$ due to the factor 10 decrease of $^{77}T_1$ upon Cu doping.

The temperature dependences of the extracted τ_cs, depicted in Fig. 5.15, are qualitatively comparable to the ones measured for the $^{77}T_1$s in Fig. 5.9, supporting the hypothesis from above.

We conclude that the spin echo decays are most likely due to the ^{209}Bi level lifetime together with the ^{77}Se-^{209}Bi indirect coupling, however a Ruderman-Kittel-Kasuya-Yosida-dominated homonuclear ^{77}Se-^{77}Se indirect coupling can also explain the data.

5.5.3 Experimental details

The double resonance experiment was performed on the Bi$_2$Se$_3$ single crystal at ambient conditions and a magnetic field of 9.4 T applied perpendicular to the crystal c-axis. The used pulse sequence was $\left\{\frac{\pi}{2}\right\}_{Se_{out}} - \tau - \{\pi\}_{Se_{out}} - \{\pi\}_{Se_{in}}$ with $\tau = 150$ μs and the pulse lengths (36 μs and 72 μs for the $\pi/2$ and π pulse, respectively) were chosen so that a pulse on Se$_{out}$ did not influence Se$_{in}$ and vice versa. For comparison, a second experiment, in which the Se$_{in}$ spins were not inverted, was performed using a slightly modified pulse sequence $\left\{\frac{\pi}{2}\right\}_{Se_{out}} - \tau - \{\pi\}_{Se_{out}} - \{\pi\}_{off}$, where the second π-pulse was off-resonant.
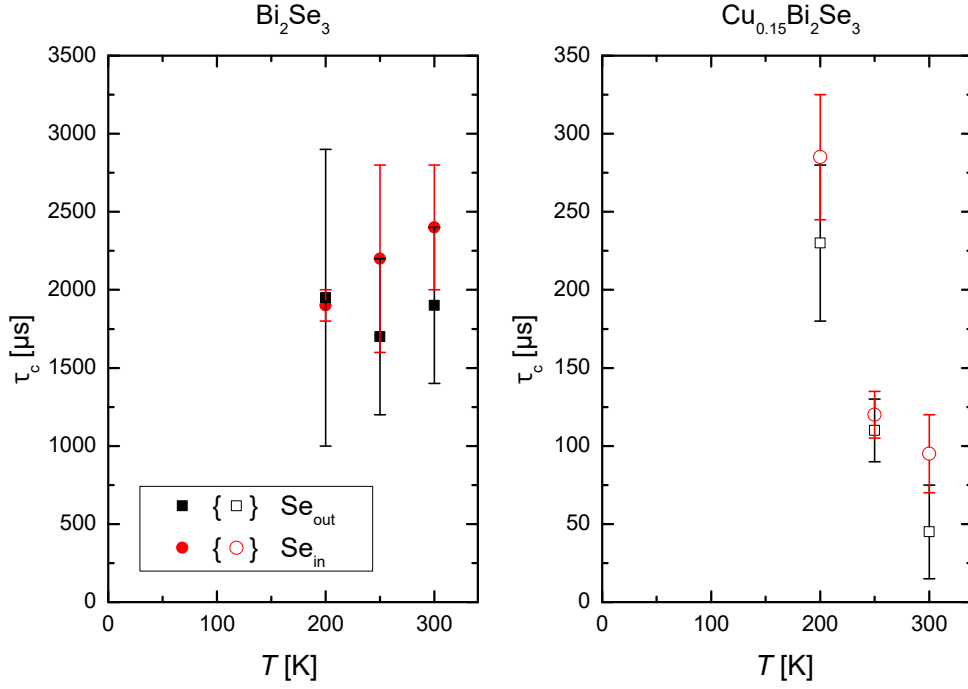
Figure 5.15: Correlation times τ_c extracted from fitting Eq. (5.4) to the spin echo decays of the ^{77}Se signals due to Se_{out} and Se_{in} in Bi_2Se_3 (left) and $Cu_{0.15}Bi_2Se_3$ (non-aged, right) oriented as $c \parallel B_0$ at 17.6 T. The amplitudes $\gamma^2\langle(h_0)^2\rangle$ in the fits were fixed to the second moments $(\pi\Lambda_0)^2/\ln 4$ corresponding to the field independent linewidths $\Lambda_0^{in(out)}$ for Bi_2Se_3 (filled symbols) or $Cu_{0.1}Bi_2Se_3$ (open symbols) from Tab. 5.5.

5.6 Summary

In this chapter we considered ^{77}Se NMR of Bi_2Se_3 and $Cu_xBi_2Se_3$ single crystals with different Cu content x (0.1, 0.125, 0.15 and 0.17). Rather similar results were found for all Cu-doped samples, which are expected to have similar charge carrier densities n ($\sim 2 \times 10^{20}$ cm^{-3}), while mostly significantly distinct results were found for the undoped Bi_2Se_3 sample having one order of magnitude smaller n (2×10^{19} to 5×10^{19} cm^{-3}). An aging effect in the $Cu_{0.15}Bi_2Se_3$ sample has shown itself in a change of color, loss of superconductivity and approach of the NMR parameters to the values measured for undoped Bi_2Se_3. While the chemistry of the aging process is unclear, the latter two phenomena can be explained by a reduction of the charge carrier density of the sample.

Two ^{77}Se signals with an intensity ratio of ~ 2 were found in all samples and the stronger (weaker) one has been assigned to nuclei occupying the Se_{out} (Se_{in}) lattice site in the crystal structure. We have verified that the signals originate from the bulk (the alternating field penetrates $\gtrsim 80$ µm deep into the crystals).

The ^{77}Se NMR parameters (shift, T_1, linewidth, T_{2G}) of the two ^{77}Se lines have been determined for various orientations of the crystals in the applied magnetic field. Furthermore, the temperature dependence of the NMR parameters was studied for Bi_2Se_3 and $Cu_{0.15}Bi_2Se_3$ (non-aged) between 200 K and room temperature.

Measured angular dependences of the shifts reveal an axially symmetric shift tensor in

all samples. The individual chemical and Knight shift contributions cannot be separated in this study, however we expect the chemical shift to be the same in all samples and hence, the shift differences to be due to (n-dependent) Knight shift differences. An *axially symmetric chemical* shift tensor is expected from the coordination symmetry of the Se$_{in}$ and Se$_{out}$ sites. Since both, the isotropic and the anisotropic parts of the total shift change with n, we infer an *axially symmetric Knight* shift tensor, in agreement with theoretical predictions [Bou16]. With increasing n, the n-dependent isotropic Knight shift for Se$_{in}$ (Se$_{out}$) increases (decreases) and the Knight shift anisotropy decreases (increases). This finding is in agreement with [Bou16] (within the experimental range for carrier densities), except for the Se$_{in}$ isotropic shift. Furthermore, we find a proportionality between the n-dependent shift changes of Se$_{in}$ and Se$_{out}$, suggesting that both selenium sites couple with the same electronic susceptibility with different (in magnitude and sign) hyperfine coupling constants.

Longitudinal relaxation times T_1 between 1 s and 5 s in Bi$_2$Se$_3$ and 10 (4) times smaller in the Cu-doped samples (aged Cu$_{0.15}$Bi$_2$Se$_3$) were measured. In all samples (i.e., independent on n) there is a constant proportionality ratio between the Se$_{in}$ and Se$_{out}$ values $T_1^{out}/T_1^{in} \approx$ 2.9 (1.5) for $c \parallel B_0$ ($c \perp B_0$), as well as anisotropy $T_1^{\parallel}/T_1^{\perp} \approx 0.7$ (1.6) for Se$_{in}$ (Se$_{out}$), supporting the hypothesis that Se$_{in}$ and Se$_{out}$ couple to the (same) itinerant electrons with different hyperfine coupling strengths (bigger for Se$_{in}$).

Upon decreasing temperature in Bi$_2$Se$_3$ and Cu$_{0.15}$Bi$_2$Se$_3$, the shifts remain unchanged, while there is an increase of T_1 (stronger in the Cu-doped sample). Although the two samples exhibit different temperature dependences of T_1, their temperature-independent proportionality ratios T_1^{out}/T_1^{in} are the same, suggesting the same relaxation mechanism in both, undoped and Cu-doped Bi$_2$Se$_3$.

Nearly isotropic linewidths Λ of 10-15 kHz for Se$_{out}$ and twice as large for Se$_{in}$ were found in all samples (only for Bi$_2$Se$_3$ a clear maximum of the Se$_{out}$ linewidth was observed near the polar angle of 45°). The linewidth contribution from dipolar internuclear coupling was computed and found to be much smaller (of the order of 1 kHz) and with a significant anisotropy. To clarify the origin of these discrepancies, field-dependent measurements (in the range 7.0-17.6 T) were performed for Bi$_2$Se$_3$ and Cu$_{0.1}$Bi$_2$Se$_3$. The outcome was only a weak dependence on the magnetic field strength of the form $\Lambda(B_0) = \sqrt{\Lambda_0^2 + [\lambda B_0]^2}$ with $\lambda \lesssim 0.4$ kHz/T (0.6 kHz/T) for Bi$_2$Se$_3$ (Cu$_{0.1}$Bi$_2$Se$_3$) and large field-independent linewidths Λ_0 (of the order of 10 kHz and 20 kHz for Se$_{out}$ and Se$_{in}$, respectively).

Field-independent linewidths in excess of what might be expected from dipole-dipole coupling for the spin-1/2 (nonquadrupolar) ^{77}Se nuclei can only be explained by an electron-mediated *indirect internuclear coupling*. Moreover, the linewidths must be due to ^{77}Se-^{209}Bi indirect coupling since ^{209}Bi has a nine-fold bigger spin (9/2) and thirteen-fold bigger abundance than ^{77}Se. The significantly larger field-independent Se$_{in}$ linewidths can be explained with Se$_{in}$ having double as many nearest ^{209}Bi neighbors and bigger hyperfine coupling strength than Se$_{out}$(as the shift and T_1 data suggest). Since the determined field-independent linewidths are nearly isotropic and due to the fact that magic angle spinning does not result in significant narrowing or appearing of side bands, we infer that the indirect internuclear coupling is not pseudopolar.

In contrast to the shifts and T_1s, the field-independent linewidths in Bi$_2$Se$_3$ and Cu$_{0.1}$Bi$_2$Se$_3$ are very similar (even slightly smaller in the sample with bigger n). Such weak n-dependence of the indirect coupling has been predicted with a model calculation

by Ion Garate in our joint publication [Geo16], showing that the indirect coupling is of Bloembergen-Rowland (rather than Ruderman-Kittel-Kasuya-Yosida) type.

The field-dependent part of the linewidth signifies a distribution of shifts, probably due to the presence of impurities (e.g., selenium vacancies). The lack of change in the linewidths upon changing temperature is expected for such a shift distribution and is also in agreement with a Bloembergen-Rowland-dominated field-independent linewidth component.

All measured spin-echo decays are well described by Gaussian fits from which the decay constants T_{2G} have been extracted. For all Cu-doped samples we find T_{2G}s of $\sim 110\,\mu s$ for Se_{out} (for $c\,\|\,B_0$, the values for $c\perp B_0$ are always 1.2 times smaller) and always roughly half as big values for Se_{in}. In comparison, the spin echoes in Bi_2Se_3 decay 2.5 times slower (at room temperature). Calculated T_{2G}s due to homonuclear dipole-dipole coupling ($\geq 2.3\,ms$) are one order of magnitude bigger than the experimental values and, in contrast to the experiments, bigger for Se_{in} than for Se_{out}.

Since homonuclear dipole-dipole interaction cannot explain the spin-echo decays, the question arises as to whether indirect internuclear ^{77}Se-^{77}Se coupling can. An evidence for the existence of enhanced Se_{out}-Se_{in} coupling was found with a double-resonance experiment (yielding T_{2G}^{out-in} one order of magnitude smaller than expected from dipolar Se_{out}-Se_{in} coupling). However, a Bloembergen-Rowland-dominated indirect coupling among ^{77}Se spins (similar to the one between ^{77}Se and ^{209}Bi spins causing the field-independent linewidths) *can not* explain the facts that (i) the T_{2G}s for the Cu-doped and the undoped Bi_2Se_3 differ, and (ii) the T_{2G}s for $Cu_{0.15}Bi_2Se_3$ increase with decreasing temperature, while the T_{2G}s for Bi_2Se_3 as well as the linewidths in both samples remain constant. Therefore, one should either contemplate the possibility of a distinct (e.g., Ruderman-Kittel-Kasuya-Yosida-dominated) indirect coupling tensor between ^{77}Se spins, or look for an additional decay mechanism. Fluctuating internal fields may lead to a decay of the spin-echo. Therefore, we have assumed and verified that ^{209}Bi spin flips (due to longitudinal relaxation) influence the ^{77}Se spin-echo decays via the strong ^{77}Se-^{209}Bi indirect coupling.

Chapter 6

^{77}Se NMR in Bi$_2$Se$_3$ powders

6.1 Samples and experimental setup

6.1.1 Sample preparation and characterization

Granular Bi$_2$Se$_3$ from Sigma Aldrich has been ground with mortar and pestle or in a planetary ball mill (for 460 minutes under an inert atmosphere). Powder X-ray diffraction (PXRD) confirmed the expected rhombohedral crystal structure in both samples, cf. Fig. 6.1, with the peaks of the ball-milled (BM) sample being significantly broadened in comparison to the ones of the mortar-ground (MG) powder. From this broadening, we could estimate the mean particle size of the BM powder to be 45 ± 10 nm. Transmission electron microscopy (TEM) images show that the BM powder consists of micrometer-sized agglomerates of individual nanoparticles, cf. Fig. 6.2. Only particles smaller than ~25 nm could be distinguished by TEM.

6.1.2 NMR setup and experimental details

The NMR measurements have been performed at 17.6 Tesla and ambient conditions using a commercial Avance 750 console and a probe by Bruker. ^{77}Se NMR signals have been acquired using spin echo pulse sequences ($\rho - \pi/2 - \tau - \pi - \text{repeat}$) with repetition time ρ and $\pi/2$-pulse length of 7 µs and pulse separation time $\tau = 15$ µs. The spectra have been sampled with frequency-stepped spin echoes, i.e., each point in the spectrum corresponds to an integrated half of an echo, measured at the respective frequency. Saturation recovery experiments ($\rho - \pi/2 - t_{\text{vd}} - \pi/2 - \tau - \pi - \text{repeat}$, with t_{vd} being a variable delay time) have been used for the determination of longitudinal relaxation times. Quality factors were 70 and 120 for the MG and BM sample, respectively.
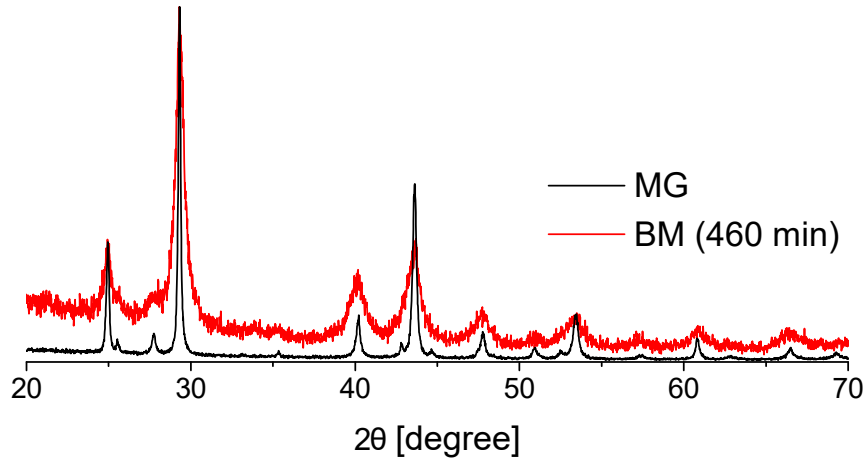
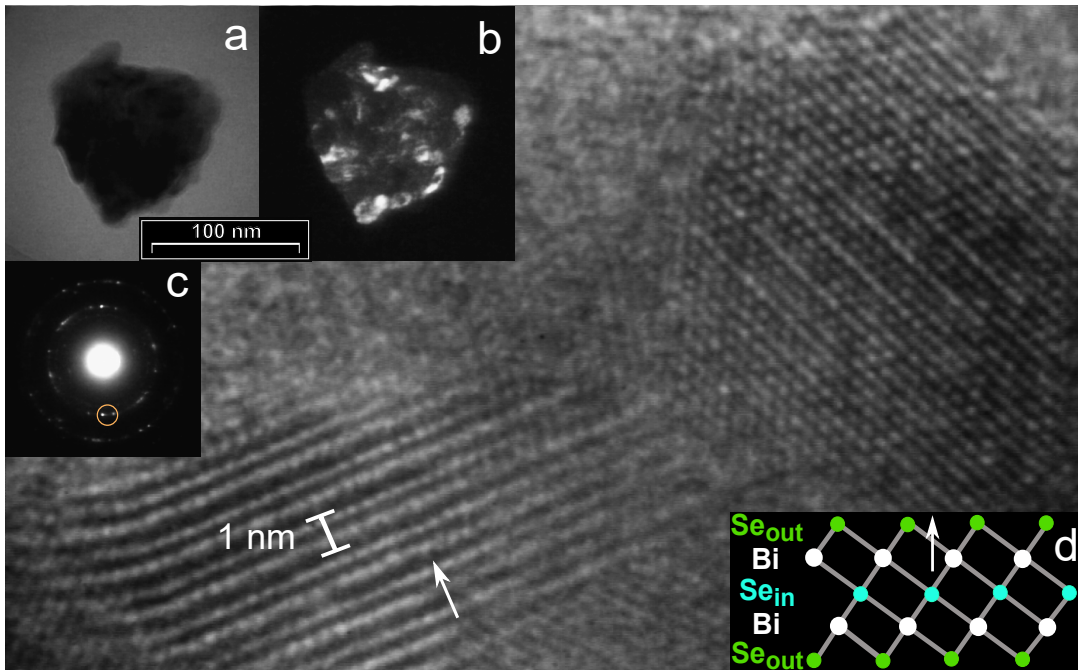**Figure 6.1:** Powder X-ray diffractograms of mortar-ground (MG) and ball-milled (BM) Bi$_2$Se$_3$.

Figure 6.2: Transmission electron microscopy of ball-milled Bi$_2$Se$_3$. Insets show bright- (a) and dark-field (b) images, and a selected area diffraction electron pattern (c) of a Bi$_2$Se$_3$ agglomerate. The encircled diffraction spots in c) have been used for the dark-field image where the corresponding individual nanocrystallites are visible. The main image shows typical Bi$_2$Se$_3$ nanocrystallites recorded digitally with high resolution. Inset d) depicts a quintuple layer and the white arrows indicate the orientation of the *c*-axis.

6.2 Results

6.2.1 Spectra

Fig. 6.3 shows the ^{77}Se NMR spectrum of MG Bi_2Se_3 powder (black squares) and a fit based on the single crystal data from last chapter (blue line). We have simulated the powder averages of the undoped and one Cu-doped Bi_2Se_3 single crystals (see the inset of Fig. 6.3) by summing up weighted single crystal spectra at different orientations of the c-axis in the magnetic field B_0 (for $0° \leq \theta \leq 90°$, in steps of 5°) assuming a homogeneous distribution of orientations and taking relaxation effects (T_1s and T_{2G}s) into account. For the fit, we have adjusted the intensity and offset of the Bi_2Se_3-based simulation so that the square root of the sum of squared differences between the fit and the data is minimized. We find a good agreement between the data and the fit.

In Fig. 6.4 the ^{77}Se NMR spectrum of BM Bi_2Se_3 powder is compared to the MG Bi_2Se_3 spectrum. Similarly to the MG sample, the BM powder exhibits a ^{77}Se NMR spectrum consisting of two signals (a stronger one at positive shifts and a weaker one at negative shifts), however, with several differences: (i) the stronger signal is broadened, (ii) the weaker signal is shifted closer to the stronger one, and (iii) the spectral weight in the region between the two peaks is increased.

6.2.2 Intensity

We have measured two BM samples from the same batch - the first (second) one with a repetition time of 25 s (12.5 s). The as-measured intensities of the second BM sample and the MG sample have been corrected for number of scans, Q-factor, and sample mass. We find that the total area underneath the corrected spectra is the same within the error.
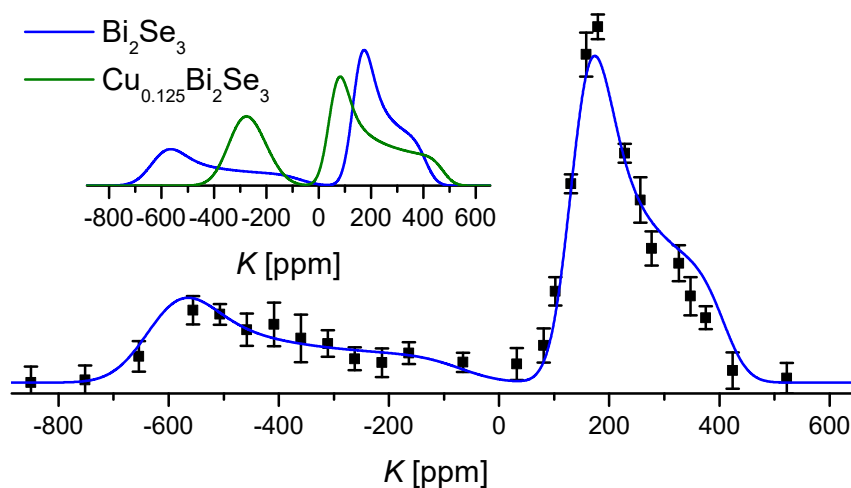

Figure 6.3: ^{77}Se NMR spectrum of MG Bi_2Se_3 powder measured at 17.6 T (black squares) and a powder spectrum simulation based on single crystal ^{77}Se NMR data from Chap. 5 (blue line), fitted to the experiment. The inset shows simulated powder spectra based on single crystal data for Bi_2Se_3 and $Cu_{0.125}Bi_2Se_3$ (see legend). Shifts (K) are given with respect to $(CH_3)_2Se$.
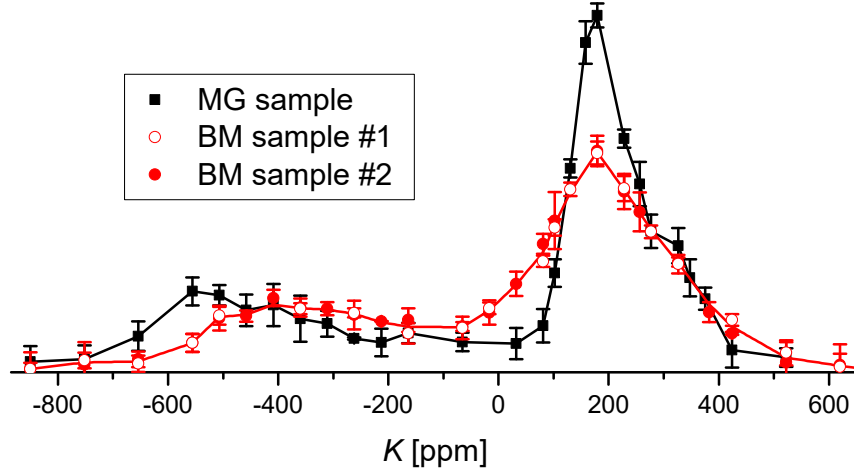
Figure 6.4: ^{77}Se NMR spectra of Bi$_2$Se$_3$ MG powder (black squares, measured with 25 s repetition time) and BM powder (open and closed red circles, for two samples from one batch measured with 25 s and 12.5 s repetition time, respectively) acquired at 17.6 T, and corrected for sample mass and quality factor (for the MG and the second BM sample; the intensity of the first BM sample has been scaled to match the second one). Solid lines are interpolations to the data. Shifts (K) are given with respect to (CH$_3$)$_2$Se.

6.2.3 Longitudinal relaxation

In a next experiment we have measured the longitudinal relaxation of the MG and the second BM sample as a function of frequency[1]. Fig. 6.5(a) shows representative saturation recovery curves (acquired at $K = +179$ ppm).

The saturation recovery data has been fitted by a stretched exponential function of the form

$$M(t) = M_0 \left[1 - q \exp\left(-(t/T_{1,\beta})^\beta \right) \right], \tag{6.1}$$

where β is a stretching exponent ($0 < \beta \leq 1$), M_0 is the maximal magnetization, and $q \approx 1$ accounts for imperfect saturation. For the MG powder $\beta = 1$ (i.e., normal exponential) gives the best fits, cf. Fig. 6.5(a), with an average T_1 of $\sim$4.5 s ($\sim$2 s) for the positive (negative) shift range, cf. Fig. 6.5(b), in agreement with the single crystal values in Chap. 5. For the BM powder $\beta \approx 0.7$ gives the best fits with average $T_{1,\beta}$ of $\sim$1.7 s ($\sim$0.9 s) for the positive (negative) shift range, cf. Fig. 6.5(b).

It is conceivable that some portion of the BM powder spectrum is due to "pristine bulk", i.e., larger particles having the same spectrum and T_1 distribution as the MG powder (which are moreover in agreement with single crystal data). Such particles would be invisible for PXRD and TEM, but visible for NMR, since the NMR signal is proportional to the number of spins. To check this hypothesis we have fitted the saturation recovery

---

1 For several different shift positions in the spectrum we have obtained the corresponding saturation recovery curves by integrating the second half of the echo in time domain (thereby obtaining solely the intensity at the excitation frequency).
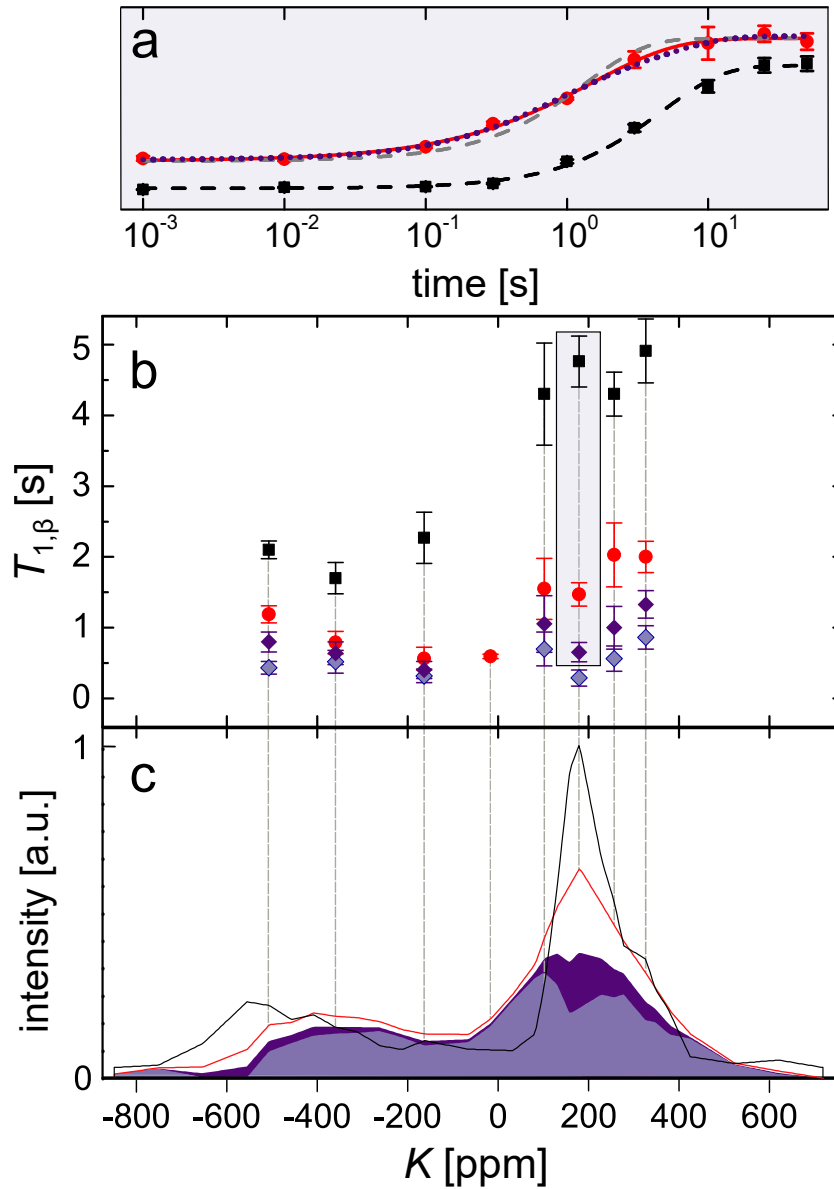
Figure 6.5: (a) Normalized ^{77}Se saturation recovery curves acquired at $K = +179$ ppm for MG (black squares) and BM (red circles) Bi_2Se_3 powder (presented with different vertical offsets). Lines are stretched exponential fits with $\beta = 1$ (dashed) and $\beta = 0.72 \pm 0.08$ (solid); and biexponential fit (dotted) with 22% pristine bulk and $\beta = 0.8 \pm 0.2$ (see text). (b) ^{77}Se $T_{1,\beta}$ relaxation times from stretched exponential fits (see text) in MG ($\beta = 1$, black squares) and BM ($\beta \approx 0.7$, red bullets) Bi_2Se_3 powder; and biexponential fits (see text) in the BM powder with two different fixed fractions of the pristine bulk: $\sim$20% (dark purple diamonds) and $\sim$40% (light purple diamonds). (c) Dark (light) purple area corresponds to fast relaxing spins remaining after subtraction of 20% (40%) pristine bulk fraction from the BM powder spectrum (see text). The red and black solid lines depict the spectra of BM and MG Bi_2Se_3 from Fig. 6.4, respectively.

of the BM sample with a sum of a normal exponential function with a known T_1 (due to pristine bulk) and a second, stretched, exponential function with a freely fitted $T_{1,\beta}$, i.e.,

$$M(t) = \alpha M_{\mathrm{MG}}(t) + M_0 \left[1 - q e^{-(t/T_{1,\beta})^\beta} \right] \tag{6.2}$$

with $M_{\mathrm{MG}}(t) = M_{0,\mathrm{MG}} \left[1 - q \exp\left(-t/T_{1,\mathrm{MG}}\right) \right]$. The fitting parameters $M_{0,\mathrm{MG}}$ and $T_{1,\mathrm{MG}}$ have been fixed to the values measured in the MG sample and α scales the fraction of the pristine bulk in the total intensity of the BM powder spectrum.

Fitting the biexponential expression from Eq. 6.2 to the BM powder data with various αs, we found that a $\sim$20% to $\sim$40% pristine bulk fraction gives the best results[1]. Note that these biexponential fits are as good as the stretched exponential ones using Eq. 6.1, cf. Fig. 6.5(a).

For the biexponential fits, both fixed $\beta = 1$ and variable β (average outcome $\sim$0.7), yield similar $T_{1,\beta}$ values within the error, and all extracted $T_{1,\beta}$s are 2 to 8 times smaller than the $T_{1,\mathrm{MG}}$s measured at the same frequency shift. For $\beta = 0.7$ there is a distribution of T_1s around $T_{1,\beta}$, which, however, spans only values smaller than $T_{1,\mathrm{MG}}$ [Joh06].

One can obtain the spectrum corresponding to these faster relaxing spins by subtracting the MG powder spectrum, multiplied by $\alpha = 0.2$ (0.4), from the BM powder spectrum, cf. dark (light) purple area in Fig. 6.5(c).

6.2.4 Spectra acquired with different repetition times

In order to separate signals with significantly distinct T_1s, we have recorded the spectrum of the second BM sample with various repetition times ρ. At sufficiently long ρ all nuclear spins would contribute to the spectrum, while at shorter ρ only faster relaxing spins would be visible. Fig. 6.6 shows spectra acquired with repetition times of 30 ms to 12.5 s. Note that the spectral shape at $\rho = 12.5$ s does not differ from the one measured with $\rho = 25$ s for the first BM sample, cf. Fig. 6.4. With decreasing $\rho < 12.5$ s, the relative intensity of the weaker signal increases and its center of mass shifts closer to the stronger signal, and below 100 ms, the spectral shape remains unchanged within the error.

For the spectra with short $\rho \leq 100$ ms, a hypothetical signal contribution from pristine bulk nuclei must be suppressed to noise level (due to their long T_1). Comparing these spectra with the spectrum obtained by subtracting a 20% pristine bulk fraction from the spectrum with long ρ (cf. dark purple area in Fig. 6.5(c)), we find an agreement, except for the strongly increased relative weight of the smaller peak at short ρ (cf. Fig. 6.6). This discrepancy disappears when the intensity of the spectrum of 80% faster relaxing spins from Fig. 6.5(c) is corrected for ρ^2, cf. striped area in Fig. 6.6.

We have looked for additional fast relaxing signals in the BM powder spectrum but did not find any within a twelve-times bigger frequency range, cf. inset of Fig. 6.6.

---

1   For $\alpha > 40$% the intensity of the pristine bulk fraction would outweigh the measured one (for the most negative shifts).

2   We have simulated the spectral shape of 80% faster relaxing spins from Fig. 6.5(c) for $\rho = 30$ ms by multiplying the intensity with $[1 - \exp\left(-30\,\mathrm{ms}/T_{1,\beta}\right)]$ using the corresponding $T_{1,\beta}$ values from Fig. 6.5(b).
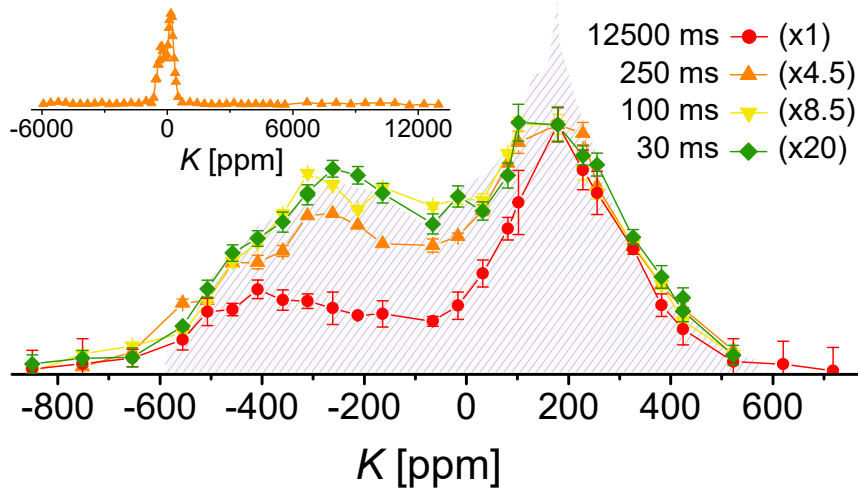
Figure 6.6: Scaled ^{77}Se NMR spectra of the second BM Bi_2Se_3 sample measured at different repetition times ρ (see legend). The inset shows a broad ranged spectrum acquired with $\rho = 250$ ms. Shifts (K) are given with respect to $(CH_3)_2$Se. The striped area represents a simulated spectrum of 80% faster relaxing spins at $\rho = 30$ ms (see text and Footnote 2).

6.3 Discussion

The measured NMR spectral shape, shifts and T_1s for the MG powder are in good agreement with the single crystal Bi_2Se_3 data. Therefore, we claim that

- the two signals in the ^{77}Se spectrum of the MG Bi_2Se_3 powder must be due to *bulk* Se_{in} and Se_{out} nuclei.

The ^{77}Se powder spectrum of MG Bi_2Se_3 reported in Ref. [Tay12] could not distinguish the Se_{in} and Se_{out} signals due to the large field-independent linewidths and low applied magnetic field (7.05 T).

Since the total intensities of the BM powder spectrum and the MG powder spectrum are comparable, we infer that

- there are no further significant signal contributions to the BM powder spectrum

(in agreement with the spectrum in the inset of Fig. 6.6). The question arises as to whether the weaker and stronger ^{77}Se signals in the BM powder spectrum can be assigned to Se_{in} and Se_{out} nuclei, respectively.

Since the two peaks in the BM powder spectrum overlap, it is not possible to determine their intensity ratio (although a $\sim 2:1$ ratio is plausible, cf. Fig. 6.4). Furthermore, one cannot quantify the differences in their first and second moments, compared to the Se_{in} and Se_{out} bulk powder spectra. The qualitative differences, however, are similar to the ones between the simulated $Cu_{0.125}Bi_2Se_3$ and Bi_2Se_3 powder spectra: the BM ($Cu_{0.125}Bi_2Se_3$) powder spectrum exhibits an increased width of the stronger signal and a decreased width and positive center-of-mass shift of the weaker signal, in comparison to the MG (Bi_2Se_3) powder spectrum, cf. Fig. 6.4 (inset of Fig. 6.3). The two signals in the BM powder

spectrum do not have the typical uniaxial powder shapes like the pristine bulk ones. However, this is not surprising since the corresponding saturation recovery curves (at a certain shift) cannot be described by a single exponential, pointing to the presence of overlapping signals with different T_1s. Therefore,

- the weaker (stronger) ^{77}Se signal in the BM powder spectrum can be due to Se$_{in}$ (Se$_{out}$) nuclei, and its altered shape in comparison to the Se$_{in}$ (Se$_{out}$) bulk powder spectrum can be explained by an increased charge carrier density n.

We can get a better insight into the composition of the BM powder spectrum by taking a closer look at the two models fitting the saturation recovery curves.

Let us consider the stretched exponential fits first. A stretching exponent β smaller than one suggests a broad distribution of T_1 values, ranging from less than 0.7 to $\sim$5 times $T_{1,\beta}$ for $\beta = 0.7$ [Joh06]. This complies with the following

- scenario (I): the BM powder spectrum consists of signals with different T_1s, some being shorter and some – longer than in the pristine bulk.

Shorter (longer) T_1s can signify increased (decreased) charge carrier density, similar to the single crystal findings in Chap. 5. Regions with decreased carrier concentrations can occur upon ball-milling, due to so-called "self-cleaning" of the bulk whereby defects are pushed towards the surface [Kou14]. Moreover, the band structure of some nanoparticles can be different from the pristine bulk band structure due to the constrained particle size and/or altered crystal structure[1], leading to altered (longer or shorter) T_1s. It is not known how the T_1 of surface nuclei (i.e., coupling to the electronic surface states) would compare to the T_1 of nuclei in the pristine bulk (remember that our pristine bulk has a significant charge carrier density of the order of 10^{19} cm^{-3}). A stretched exponential relaxation has been predicted for nuclei sitting near the surface of the topological Kondo insulator SmB$_6$ [Sch14] (since the wave functions of the surface states fall off exponentially with distance).

Let us now consider the biexponential fits, suggesting

- scenario (II): the BM powder spectrum consists of 20% to 40% pristine bulk nuclei and 60% to 80% (faster relaxing) nuclei with shorter T_1s.

The spectrum of 80% faster relaxing spins extracted within this scenario agrees with the measurements with short repetition times where the pristine bulk contributions must be suppressed. This spectrum consists of two overlapping (weaker and stronger) signals with an intensity ratio close to 2 (cf. dark purple area in Fig. 6.5(c)). Their shapes can be explained as a superposition of distinct (Se$_{in}$ and Se$_{out}$) powder spectra, in compliance with the corresponding stretched exponential relaxation curves. Moreover, both, the changes in the spectral shape and the T_1-decrease with respect to the bulk ^{77}Se NMR can come from increased charge carrier densities. Therefore, we conclude that

- the BM powder spectrum is most likely due to $\sim$20% pristine bulk and $\sim$80% faster relaxing Se$_{in}$ and Se$_{out}$ nuclei (having 2 to 8 times shorter T_1s than the pristine bulk nuclei).

---

1 Note that in the TEM image in Fig. 6.2 one of the particles has a bent edge.

It is not clear whether the faster relaxing spins are coupled to the topological surface states or not. The number of surface nuclei in the sample cannot be estimated, since we do not know the exact particle size distribution (PXRD gives only an average size of $\sim 45\,\mathrm{nm}$ and TEM shows a big portion of $\sim 5\,\mathrm{nm}$ big particles, however, cannot distinguish particles bigger than $\sim 25\,\mathrm{nm}$) and moreover, the particle shape is unknown. Further measurements (going beyond the time constraint of this work) are needed, e.g., of the temperature dependence of T_1, or following the recently reported approach [Cho18] of physically mixing the Bi_2Se_3 nanoparticles with Al_2O_3 to increase further the surface-to-volume ratio. Moreover, measuring the powder spectra with magic angle spinning could help in separating signal contributions having significantly distinct isotropic shifts.

6.4 Summary

In this chapter we considered the ^{77}Se NMR of bulk, mortar-ground (MG), Bi_2Se_3 powder in comparison to nanocrystalline, ball-milled (BM), Bi_2Se_3 powder with increased surface-to-volume ratio.

The ^{77}Se powder spectrum and longitudinal relaxation of the MG sample were shown to agree with the single crystal Bi_2Se_3 data. Hence, the weaker and stronger signals in the MG powder spectrum must be due to bulk nuclei occupying the Se_{in} and Se_{out} crystallographic sites, respectively.

Similarly to the MG powder spectrum, the ^{77}Se spectrum of the BM powder contains two peaks of different intensity (we have verified that there are no further signals). However, the BM powder spectral shape is altered so that (i) the stronger signal is broadened, (ii) the weaker signal is shifted closer to the stronger one and, as a result, (iii) the two overlap. Furthermore, the BM powder exhibits altered longitudinal relaxation behavior with respect to the one of the bulk – with faster, non-single exponential relaxation curves. Both, the spectral and relaxation changes can be due to a distribution of *increased* charge carrier densities in the BM sample (compared to the carrier density in the bulk Bi_2Se_3 samples).

Two different models fit the relaxation data for the BM powder equally well and hence, two scenarios have been considered for the interpretation of the data. On one hand, stretched exponential functions, i.e., $1 - \exp\left(-(t/T_{1,\beta})^\beta\right)$ with $\beta \approx 0.7$, fit the data and lead to the scenario (I), where the BM powder spectrum consists of overlapping signals with various T_1s spanning from $\sim 20\%$ to $\sim 200\%$ of the bulk T_1s. On the other hand, assuming a certain "pristine bulk" fraction in the BM powder (i.e., ^{77}Se nuclei exhibiting the same NMR parameters as the ones in the MG powder), we could separate its contribution from both, the BM powder spectrum and relaxation data. Hence, we obtained the scenario (II), where 20% to 40% of the BM powder spectrum are due to pristine bulk nuclei and the remaining 60% to 80% are due to (two- to eight-times) faster relaxing nuclei.

Both scenarios are conceivable: T_1s shorter (longer) than the pristine-bulk ones can be attributed to regions with increased (decreased) bulk carrier density, e.g., due to a redistribution of ^{77}Se vacancies or an altered bulk band structure upon ball-milling, or to surface nuclei which couple to the topological surface states.

However, while the BM powder spectrum does not reveal signatures of the slower relaxing spins that were suggested by scenario (I), the spectrum of the fast-relaxing nuclei separated within scenario (II) complies with the BM powder spectrum measured with short repetition time (where pristine-bulk signals must be suppressed). Therefore, we consider scenario (II)

being more likely.

Although the origin of the shortened relaxation cannot be clarified on the basis of our data, they still complement the picture and call for revision of earlier NMR studies, cf. Chap. 4. We saw here that the underlying pristine bulk signal can be separated both from the spectrum and from the relaxation curves if one measures a bulky sample under the same conditions as the nanoparticles under investigation.

Chapter 7

Conclusion

In this thesis, a thorough ^{77}Se NMR study of the model topological insulator compound Bi_2Se_3 was presented. We believe that this work contributes significantly to forming a basis for understanding the bulk and surface NMR of Bi_2Se_3, Bi_2Te_3, and other topologically nontrivial systems with strong spin-orbit coupling.

The ^{77}Se NMR properties of the bulk were investigated in $Cu_xBi_2Se_3$ single crystals with various Cu doping (x=0, 0.10, 0.125, 0.15, and 0.17) for different crystal orientations in the applied field (at 17.6 T and ambient conditions). The undoped and one Cu-doped Bi_2Se_3 sample with x=0.15 (x=0.1) were moreover studied as a function of temperature (magnetic field strength) in the range 200-295 K (7.0-17.6 T). In order to examine the surface with NMR, nanometer-sized Bi_2Se_3 particles with increased surface-to-bulk ratio were produced and compared to bulk Bi_2Se_3 powder. For these powder samples, the ^{77}Se NMR intensity and longitudinal relaxation were measured as a function of frequency (at 17.6 T and ambient conditions). The data have been interpreted by means of established solid-state NMR theory, as well as by comparison to newly developed theoretical models for Bi_2Se_3 and Bi_2Te_3.

For the first time, signals from the crystallographically distinct selenium sites Se_{in} and Se_{out} have been distinguished and thoroughly characterized. As a consequence, the powder spectrum of the bulk could be understood. The NMR shifts and T_1s were found to be sensitive to the charge carrier density of the sample. Correlations – in various NMR parameters – between Se_{in} and Se_{out} have been revealed, pointing to different (in magnitude and sign) site-specific hyperfine couplings to itinerant electrons. Field-independent linewidths in ten- to twenty-fold excess of conventional theoretical expectations were found and explained by an electron-mediated indirect internuclear coupling. The unexpectedly fast spin-echo decays are most likely due to the ^{209}Bi Zeeman-level lifetime causing fluctuating magnetic fields at the Se sites with amplitudes determined by ^{77}Se-^{209}Bi indirect coupling. Most of these findings were published in 2016 [Geo16] in collaboration with Ion Garate, whose model calculation based on bulk electronic bands affirms the suggested indirect coupling and moreover shows that it is Bloembergen-Rowland dominated.

With the hitherto created understanding of the bulk, we looked for surface ^{77}Se NMR signals in Bi_2Se_3 nanoparticles. Contributions from pristine bulk nuclei could be separated from both, the spectrum and the longitudinal relaxation data and thereby, signals due to (two- to eight-times) faster relaxing spins (making 80% of the total intensity) were revealed. Whether these fast relaxing nuclei couple to the topological surface states remains unclear.

In future experiments, an improved approach to the surface NMR might be realized with

samples having defined size and shape, e.g., synthesized nanoparticles or thin films stacked in alternating order together with intermediate (normal) insulating layers. In order to be able to separate and understand signals from surface nuclei, the complex bulk NMR needs to be studied further in the future. For this purpose, variously doped single crystal samples with (a wide range of) well-known charge carrier densities are needed and the temperature-, field- and orientation-dependence of shifts, T_1s, spin-echo decays and linewidths have to be studied thoroughly. On the theoretical front, *ab initio* calculations of the NMR shifts, T_1s and field-independent linewidths would be very desirable. A resulting quantitative understanding of bulk NMR data might hold important clues about material properties, including the characterization of the surface electronic states.

In summary, this thesis offers a deeper insight into the nontrivial NMR of the spin-orbit coupled systems Bi_2Se_3 and Bi_2Te_3 by reviewing the current state of the art and comprehensively discussing the own and literature data in the context of well-established and newly made theoretical models.

Bibliography

[Abr61]   ABRAGAM, A.: *The Principles of Nuclear Magnetism.* Oxford University Press, 1961 (cit. on pp. 7, 13, 42, 43, 46).

[Ana10]   ANALYTIS, J.G., J.-H. CHU, Y. CHEN, F. CORREDOR, R.D. MCDONALD, Z.X. SHEN, and I.R. FISHER: 'Bulk Fermi surface coexistence with Dirac surface state in Bi_2Se_3: A comparison of photoemission and Shubnikov de Haas measurements'. *Phys. Rev. B* (2010), vol. 81(20): p. 205407 (cit. on p. 5).

[And13]   ANDO, Y.: 'Topological Insulator Materials'. *Journal of the Physical Society of Japan* (2013), vol. 82(10): p. 102001 (cit. on pp. 1, 6).

[Ant17a]   ANTONENKO, A.O., E.V. CHARNAYA, D.YU. NEFEDOV, D.YU. PODOROZHKIN, A.V. USKOV, A.S. BUGAEV, M.K. LEE, L.J. CHANG, S.V. NAUMOV, YU.A. PEREVOZCHIKOVA, V.V. CHISTYAKOV, J.C.A. HUANG, and V.V. MARCHENKOV: 'NMR study of topological insulator Bi_2Te_3 in a wide temperature range'. *Physics of the Solid State* (2017), vol. 59(12): 2331 to 2339 (cit. on pp. 2, 17, 19–21).

[Ant17b]   ANTONENKO, A.O., E.V. CHARNAYA, D.YU. NEFEDOV, D.YU. PODOROZHKIN, A.V. USKOV, A.S. BUGAEV, M.K. LEE, L.J. CHANG, S.V. NAUMOV, YU.A. PEREVOZCHIKOVA, V.V. CHISTYAKOV, E.B. MARCHENKOVA, H.W. WEBER, J.C.A. HUANG, and V.V. MARCHENKOV: 'NMR studies of single crystals of the topological insulator Bi_2Te_3 at low temperatures'. *Physics of the Solid State* (2017), vol. 59(5): 855 to 859 (cit. on pp. 17, 20, 21).

[Ant18]   ANTONENKO, A.O., D.YU. NEFEDOV, E.V. CHARNAYA, S.V. NAUMOV, and V.V. MARCHENKOV: '^{77}Se Low-Temperature NMR in the Bi_2Se_3 Single Crystalline Topological Insulator'. *Applied Magnetic Resonance* (2018), vol. 49(6): 599 to 605 (cit. on pp. 17, 19, 21).

[Blo55]   BLOEMBERGEN, N. and T.J. ROWLAND: 'Nuclear Spin Exchange in Solids: Tl^{203} and Tl^{205} Magnetic Resonance in Thallium and Thallic Oxide'. *Phys. Rev.* (1955), vol. 97(6): pp. 1679–1698 (cit. on p. 42).

[Bou16]   BOUTIN, S., J. RAMIREZ-RUIZ, and I. GARATE: 'Tight-binding theory of NMR shifts in topological insulators Bi_2Se_3 and Bi_2Te_3'. *Phys. Rev. B* (2016), vol. 94(11): p. 115204 (cit. on pp. 2, 23, 36, 37, 42, 50).

[Che09]   CHEN, Y.L., J.G. ANALYTIS, J.-H. CHU, Z.K. LIU, S.-K. MO, X.L. QI, H.J. ZHANG, D.H. LU, X. DAI, Z. FANG, S.C. ZHANG, I.R. FISHER, Z. HUSSAIN, and Z.-X. SHEN: 'Experimental Realization of a Three-Dimensional Topological Insulator, Bi2Te3'. *Science* (2009), vol. 325(5937): pp. 178–181 (cit. on p. 4).

[Cho18]   CHOI, D.M. and C.E. LEE: '^{77}Se Nuclear Magnetic Resonance Study of the Surface Effect in Topological Insulator Bi_2Se_3 Nanoparticles'. *Journal of the Korean Physical Society* (2018), vol. 72(7): 835 to 837 (cit. on pp. 17, 19, 21, 22, 24, 61).

[Das11]   DAS, P., Y. SUZUKI, M. TACHIKI, and K. KADOWAKI: 'Spin-triplet vortex state in the topological superconductor $Cu_xBi_2Se_3$'. *Phys. Rev. B* (2011), vol. 83(22): p. 220513 (cit. on p. 25).

[Fen12]   FENG, W.X. and Y.G. YAO: 'Three-dimensional topological insulators: A review on host materials'. *Science China Physics, Mechanics and Astronomy* (Nov. 2012), vol. 55(12): pp. 2199–2212 (cit. on p. 1).

[Fra13]   FRANZ, M. and L. MOLENKAMP, eds.: *Topological Insulators*. Elsevier, 2013 (cit. on pp. 1, 3–6).

[Fu10]   FU, L. and E. BERG: 'Odd-Parity Topological Superconductors: Theory and Application to $Cu_xBi_2Se_3$'. *Phys. Rev. Lett.* (2010), vol. 105(9): p. 097001 (cit. on p. 5).

[Fu07a]   FU, L. and C.L. KANE: 'Topological insulators with inversion symmetry'. *Phys. Rev. B* (2007), vol. 76(4): p. 045302 (cit. on p. 4).

[Fu07b]   FU, L., C.L. KANE, and E.J. MELE: 'Topological Insulators in Three Dimensions'. *Phys. Rev. Lett.* (2007), vol. 98(10): p. 106803 (cit. on pp. 1, 3).

[Geo16]   GEORGIEVA, N.M., D. RYBICKI, R. GUEHNE, G.V.M. WILLIAMS, S.V. CHONG, K. KADOWAKI, I. GARATE, and J. HAASE: '^{77}Se nuclear magnetic resonance of topological insulator Bi_2Se_3'. *Phys. Rev. B* (2016), vol. 93(19): p. 195120 (cit. on pp. 2, 17, 19, 20, 23, 35, 42, 51, 63).

[Gue]   GUEHNE, R.: 'Private communication'. unpublished (cit. on pp. 34, 43, 47).

[Har08]   HARRIS, R.K., E.D. BECKER, S.M. CABRAL de MENEZES, P. GRANGER, R.E. HOFFMAN, and K.W. ZILM: 'Further conventions for NMR shielding and chemical shifts (IUPAC Recommendations 2008)'. *Pure and Applied Chemistry* (2008), vol. 80(1): pp. 59–84 (cit. on pp. 27, 75, 76).

[Has10]   HASAN, M.Z. and C.L. KANE: 'Colloquium: Topological insulators'. *Reviews of Modern Physics* (2010), vol. 82(4): 3045 to 3067 (cit. on pp. 1, 3).

[Has11]   HASAN, M.Z. and J.E. MOORE: 'Three-Dimensional Topological Insulators'. *Annual Review of Condensed Matter Physics* (2011), vol. 2(1): pp. 55–78 (cit. on p. 1).

[Hat17]   HATTORI, Y., Y. TOKUMOTO, and K. EDAGAWA: 'Optimizing composition of $Pb(Bi_{1-x}Sb_x)_2Te_4$ topological insulator to achieve a bulk-insulating state'. *Phys. Rev. Materials* (2017), vol. 1(7): p. 074201 (cit. on p. 6).

[Höf]   HÖFER, F.: 'Private communication'. unpublished (cit. on p. 43).

[Hor09]   HOR, Y.S., A. RICHARDELLA, P. ROUSHAN, Y. XIA, J.G. CHECKELSKY, A. YAZDANI, M.Z. HASAN, N.P. ONG, and R.J. CAVA: 'p-type Bi_2Se_3 for topological insulator and low-temperature thermoelectric applications'. *Phys. Rev. B* (2009), vol. 79(19): p. 195208 (cit. on p. 5).

[Hor10]   HOR, Y.S., A.J. WILLIAMS, J.G. CHECKELSKY, P. ROUSHAN, J. SEO, Q. XU, H.W. ZANDBERGEN, A. YAZDANI, N.P. ONG, and R.J. CAVA: 'Superconductivity in $Cu_xBi_2Se_3$ and its Implications for Pairing in the Undoped Topological Insulator'. *Phys. Rev. Lett.* (2010), vol. 104(5): p. 057001 (cit. on pp. 29, 35).

[Hsi08]   HSIEH, D., D. QIAN, L. WRAY, Y. XIA, Y.S. HOR, R.J. CAVA, and M.Z. HASAN: 'A topological Dirac insulator in a quantum spin Hall phase'. *Nature* (2008), vol. 452(7190): pp. 970–974 (cit. on p. 4).

[Joh06]   JOHNSTON, D.C.: 'Stretched exponential relaxation arising from a continuous sum of exponential decays'. *Physical Review B* (2006), vol. 74(18) (cit. on pp. 58, 60).

[Kou13]   KOUMOULIS, D., T.C. CHASAPIS, R.E. TAYLOR, M.P. LAKE, D. KING, N.N. JARENWATTANANON, G.A. FIETE, M.G. KANATZIDIS, and L.-S. BOUCHARD: 'NMR Probe of Metallic States in Nanoscale Topological Insulators'. *Phys. Rev. Lett.* (2013), vol. 110(2): p. 026602 (cit. on pp. 2, 17–20).

[Kou14]   KOUMOULIS, D., B. LEUNG, T.C. CHASAPIS, R. TAYLOR, D. KING, M.G. KANATZIDIS, and L.-S. BOUCHARD: 'Understanding Bulk Defects in Topological Insulators from Nuclear-Spin Interactions'. *Advanced Functional Materials* (2014), vol. 24(11): pp. 1519–1528 (cit. on pp. 2, 17, 18, 60).

[Kus16]   KUSHWAHA, S.K. et al.: 'Sn-doped $Bi_{1.1}Sb_{0.9}Te_2S$ bulk crystal topological insulator with excellent properties'. *Nature Communications* (2016), vol. 7: p. 11456 (cit. on p. 6).

[Lee16]   LEE, C.-K., C.-M. CHENG, S.-C. WENG, W.-C. CHEN, K.-D. TSUEI, S.-H. YU, M. M.-C. CHOU, C.-W. CHANG, L.-W. TU, H.-D. YANG, C.-W. LUO, and M.M. GOSPODINOV: 'Robustness of a Topologically Protected Surface State in a Sb_2Te_2Se Single Crystal'. *Scientific Reports* (2016), vol. 6(1) (cit. on p. 6).

[Lee17]   LEE, P.-H., J. ZHOU, S.-T. PI, and Y.-K. WANG: 'Topological insulators double perovskites: A_2TePoO_6 (A = Ca, Sr, Ba)'. *Journal of Applied Physics* (2017), vol. 122(22): 224902 to (cit. on p. 6).

[Lel73]   LELOUP, J.Y., B. SAPOVAL, and G. MARTINEZ: 'Knight shift in multivalley semiconductors. II. Determination of the hyperfine coupling constants in *N*- and *P*-type PbSe and PbTe'. *Phys. Rev. B* (1973), vol. 7(12): pp. 5276–5284 (cit. on p. 35).

[Lev16]   LEVIN, E.M., T.M. RIEDEMANN, A. HOWARD, N.H. JO, S.L. BUDKO, P.C. CANFIELD, and T.A. LOGRASSO: '^{125}Te NMR and Seebeck effect in Bi_2Te_3 synthesized from stoichiometric and Te-rich melts'. *The Journal of Physical Chemistry C* (2016), vol. 120(44): 25196 to 25202 (cit. on pp. 17, 19, 20).

[Lut78a]   LUTZ, O., H. OEHLER, and P. KRONECK: '^{63}Cu and ^{65}Cu Fourier transform nuclear magnetic resonance studies'. *Zeitschrift für Physik A Atoms and Nuclei* (1978), vol. 288(1): pp. 17–21 (cit. on p. 75).

[Lut78b]   LUTZ, O., H. OEHLER, and P. KRONECK: 'Chemical shifts and coupling constants in copper(I)-compounds by ^{63}Cu and ^{65}Cu FT-NMR studies'. *Zeitschrift für Naturforschung* (June 1978), vol. 33a: pp. 1021–1024 (cit. on p. 75).

[Mat16]   MATANO, K., M. KRIENER, K. SEGAWA, Y. ANDO, and G.-Q. ZHENG: 'Spin-rotation symmetry breaking in the superconducting state of $Cu_xBi_2Se_3$'. *Nature Physics* (May 2016), vol. 12(9): 852 to 854 (cit. on pp. 2, 17, 20).

[Muk15]   MUKHOPADHYAY, S., S. KRÄMER, H. MAYAFFRE, H.F. LEGG, M. ORLITA, C. BERTHIER, M. HORVATI Ć, G. MARTINEZ, M. POTEMSKI, B.A. PIOT, A. MATERNA, G. STRZELECKA, and A. HRUBAN: 'Hyperfine coupling and spin polarization in the bulk of the topological insulator Bi_2Se_3'. *Phys. Rev. B* (2015), vol. 91(8): p. 081105 (cit. on pp. 2, 17, 22, 23, 30, 43).

[Nak07]   NAKANISHI, W., S. HAYASHI, and M. HADA: 'How ^{77}Se NMR chemical shifts originate from pre-$^{\alpha}$, $^{\beta}$, and $^{\gamma}$ effects: Interpretation based on molecular orbital theory'. *Chemistry - A European Journal* (2007), vol. 13(18): pp. 5282–5293 (cit. on p. 76).

[Nis13]   NISSON, D.M., A.P. DIOGUARDI, P. KLAVINS, C.H. LIN, K. SHIRER, A.C. SHOCKLEY, J. CROCKER, and N.J. CURRO: 'Nuclear magnetic resonance as a probe of electronic states of Bi_2Se_3'. *Phys. Rev. B* (2013), vol. 87(19): p. 195202 (cit. on pp. 2, 5, 17, 22, 34, 35, 43).

[Nis14]   NISSON, D.M., A.P. DIOGUARDI, X. PENG, D. YU, and N.J. CURRO: 'Anomalous nuclear magnetic resonance spectra in Bi_2Se_3 nanowires'. *Phys. Rev. B* (2014), vol. 90(12): p. 125121 (cit. on pp. 2, 17, 21, 22, 43).

[Pi17]   Pi, S.-T., H. Wang, J. Kim, R. Wu, Y.-K. Wang, and C.-K. Lu: 'New class of 3D topological insulator in double perovskite'. *The Journal of Physical Chemistry Letters* (2017), vol. 8(2): 332 to 339 (cit. on p. 6).

[Pod15]   Podorozhkin, D.Yu., E.V. Charnaya, A. Antonenko, R. Mukham-ad'yarov, V.V. Marchenkov, S.V. Naumov, J.C.A. Huang, H.W. Weber, and A.S. Bugaev: 'Nuclear magnetic resonance study of a Bi_2Te_3 topological insulator'. English. *Physics of the Solid State* (2015), vol. 57(9): pp. 1741–1745 (cit. on pp. 2, 17, 19, 21).

[Qi11]   Qi, X.-L. and S.-C. Zhang: 'Topological insulators and superconductors'. *Rev. Mod. Phys.* (2011), vol. 83(4): pp. 1057–1110 (cit. on p. 1).

[Ram17]   Ramirez-Ruiz, J., S. Boutin, and I. Garate: 'NMR in an electric field: A bulk probe of the hidden spin and orbital polarizations'. *Physical Review B* (2017), vol. 96(23) (cit. on p. 23).

[Rec96]   Recchia, C.H., K. Gorny, and C.H. Pennington: 'Gaussian-approximation formalism for evaluating decay of NMR spin echoes'. *Phys. Rev. B* (1996), vol. 54(6): pp. 4207–4217 (cit. on p. 47).

[Ren10]   Ren, Z., A.A. Taskin, S. Sasaki, K. Segawa, and Y. Ando: 'Large bulk resistivity and surface quantum oscillations in the topological insulator Bi_2Te_2Se'. *Phys. Rev. B* (2010), vol. 82(24): p. 241306 (cit. on p. 6).

[Sán16]   Sánchez-Barriga, J., E. Golias, A. Varykhalov, J. Braun, L.V. Yashina, R. Schumann, J. Minár, H. Ebert, O. Kornilov, and O. Rader: 'Ultrafast spin-polarization control of Dirac fermions in topological insulators'. *Phys. Rev. B* (2016), vol. 93(15): p. 155426 (cit. on p. 1).

[Sch14]   Schlottmann, P.: 'NMR relaxation in the topological Kondo insulator SmB_6'. *Physical Review B* (2014), vol. 90(16) (cit. on pp. 23, 60).

[She17]   Shen, S., W. Zhu, Y. Deng, H. Zhao, Y. Peng, and C. Wang: 'Enhancing thermoelectric properties of Sb_2Te_3 flexible thin film through microstructure control and crystal preferential orientation engineering'. *Applied Surface Science* (2017), vol. 414: pp. 197–204 (cit. on p. 4).

[She18]   Shen, S.-Q.: *Topological Insulators*. 2018 (cit. on p. 4).

[Sli10]   Slichter, C.P.: *Principles of Magnetic Resonance*. Springer, 2010 (cit. on pp. 7, 14, 48).

[Son17]   Song, H.-D., D. Sheng, A.-Q. Wang, J.-G. Li, D.-P. Yu, and Z.-M. Liao: 'Topological transport in Dirac electronic systems: A concise review'. *Chinese Physics B* (2017), vol. 26(3): p. 037301 (cit. on p. 1).

[Sun15]   Sun, G., X. Qin, D. Li, J. Zhang, B. Ren, T. Zou, H. Xin, S. Buehler Paschen, and X. Yan: 'Enhanced thermoelectric performance of n-type Bi$_2$Se$_3$ doped with Cu'. *Journal of Alloys and Compounds* (2015), vol. 639: pp. 9–14 (cit. on p. 4).

[Tay12]   Taylor, R.E., B. Leung, M.P. Lake, and L.-S. Bouchard: 'Spin-lattice relaxation in bismuth chalcogenides'. *J. Phys. Chem. C* (2012), vol. 116(32): pp. 17300–17305 (cit. on pp. 2, 17–20, 30, 42, 59).

[Urk17]   Urkude, R.R., R. Rawat, and U.A. Palikundwar: 'Temperature and impurity effect on parallel field magnetoconductance of bulk insulating topological insulator (Bi$_{1-x}$Sb$_x$)$_2$Te$_3$'. *Journal of Physics: Condensed Matter* (2017), vol. 29(49): p. 495602 (cit. on p. 6).

[Van48]   Van Vleck, J.H.: 'The dipolar broadening of magnetic resonance lines in crystals'. *Phys. Rev.* (1948), vol. 74(9): pp. 1168–1183 (cit. on p. 12).

[Wan18]   Wang, Y., T.P. Ginley, and S. Law: 'Growth of high-quality Bi$_2$Se$_3$ topological insulators using (Bi$_{1-x}$In$_x$)$_2$Se$_3$ buffer layers'. *Journal of Vacuum Science & Technology B, Nanotechnology and Microelectronics: Materials, Processing, Measurement, and Phenomena* (2018), vol. 36(2): p. 02D101 (cit. on p. 6).

[Wan10]   Wang, Z., T. Lin, P. Wei, X. Liu, R. Dumas, K. Liu, and J. Shi: 'Tuning carrier type and density in Bi$_2$Se$_3$ by Ca-doping'. *Applied Physics Letters* (2010), vol. 97(4), 042112: pp. 1–3 (cit. on p. 5).

[Xia09]   Xia, Y., D. Qian, D. Hsieh, L. Wray, A. Pal, H. Lin, A. Bansil, D. Grauer, Y.S. Hor, R.J. Cava, and M.Z. Hasan: 'Observation of a large-gap topological-insulator class with a single Dirac cone on the surface'. *Nat. Phys.* (2009), vol. 5(6): p. 398 (cit. on p. 4).

[Yes12]   Yesinowski, J.P.: 'Solid-state NMR of inorganic semiconductors'. *Topics in Current Chemistry* (2012), vol. 306: pp. 229–312 (cit. on p. 35).

[Yos15]   Yoshimi, R., A. Tsukazaki, Y. Kozuka, J. Falson, K.S. Takahashi, J.G. Checkelsky, N. Nagaosa, M. Kawasaki, and Y. Tokura: 'Quantum Hall effect on top and bottom surface states of topological insulator (Bi$_{1-x}$Sb$_x$)$_2$Te$_3$ films'. *Nature Communications* (2015), vol. 6(1): p. 6627 (cit. on p. 6).

[You12]   Young, B.-L., Z.-Y. Lai, Z. Xu, A. Yang, G.D. Gu, Z.-H. Pan, T. Valla, G.J. Shu, R. Sankar, and F.C. Chou: 'Probing the bulk electronic states of Bi$_2$Se$_3$ using nuclear magnetic resonance'. *Phys. Rev. B* (2012), vol. 86(7): p. 075137 (cit. on pp. 2, 17, 22, 23, 43).

[Zha09]   Zhang, H., C.-X. Liu, X.-L. Qi, X. Dai, Z. Fang, and S.-C. Zhang: 'Topological insulators in Bi$_2$Se$_3$, Bi$_2$Te$_3$ and Sb$_2$Te$_3$ with a single Dirac cone on the surface'. *Nat. Phys.* (2009), vol. 5(6): pp. 438–442 (cit. on p. 4).

[Zha15]   ZHANG, X. and L.-D. ZHAO: 'Thermoelectric materials: Energy conversion between heat and electricity'. *Journal of Materiomics* (2015), vol. 1(2): pp. 92–105 (cit. on p. 4).

[Zoc13]   ZOCHER, B. and B. ROSENOW: 'Surface states and local spin susceptibility in doped three-dimensional topological insulators with odd-parity superconducting pairing symmetry'. *Phys. Rev. B* (2013), vol. 87(15): p. 155138 (cit. on p. 23).

Acknowledgments

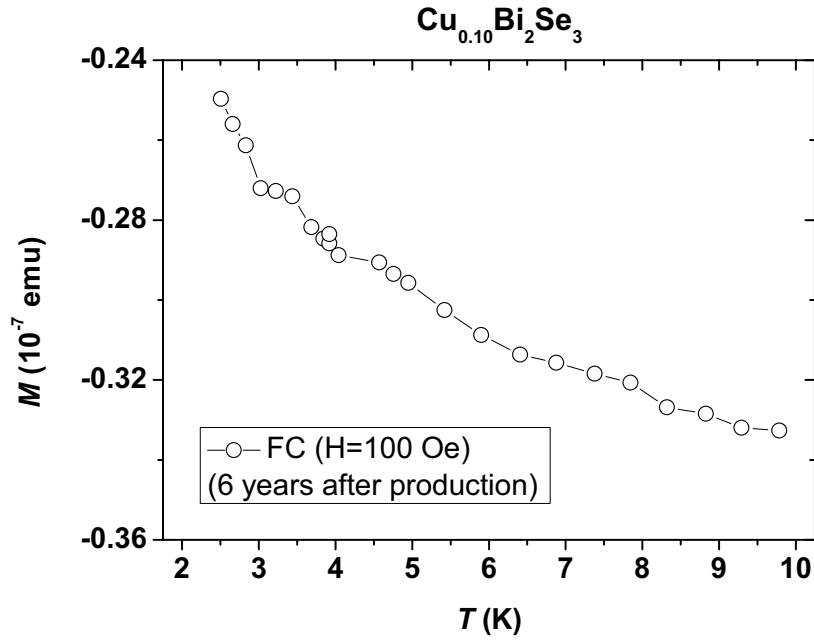# Appendix A

Magnetization measurements on $Cu_xBi_2Se_3$ single crystals

Figure A.1: DC-SQUID magnetization measurement in field-cooling (FC) mode at $H = 100$ Oe of the $Cu_{0.10}Bi_2Se_3$ single crystal performed 6 years after its production by Shen Chong at the Victoria University of Wellington. During the whole 6 years the single crystal has been kept in an inert atmosphere.
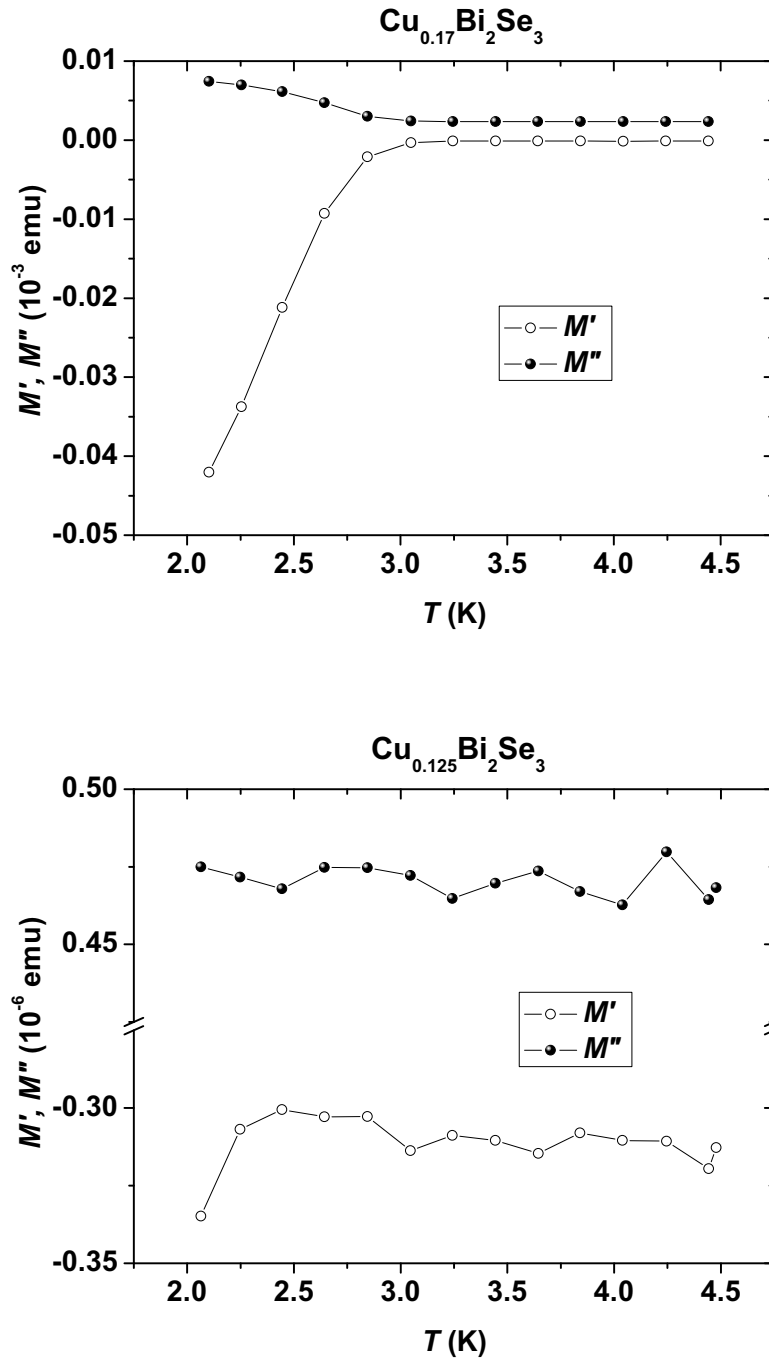
Figure A.2: Alternating current (AC) magnetization measurements performed by Shen Chong at the Victoria University of Wellington using the AC measurement system option of a Physical Property Measurement System (PPMS). The upper (lower) plot shows data on $Cu_{0.17}Bi_2Se_3$ ($Cu_{0.125}Bi_2Se_3$) acquired with an excitation field of 2 Oe (5 Oe) at a frequency of 666 Hz (1000 Hz) shortly after the production of the samples.

Appendix B

Shift determination using metallic copper powder

We want to use metallic copper for determining the chemical shift of a sample. The chemical shift δ for an isotope X is defined as

$$\delta_{\text{sample}}(X) = \frac{\nu_{\text{sample}}(X) - \nu_{\text{reference}}(X)}{\nu_{\text{reference}}(X)} \cdot 10^6. \tag{B.1}$$

Here $\nu_{\text{reference}}$ is the frequency of a standard reference compound for X, measured at the same magnetic field as the sample.

We want to compute $\nu_{\text{reference}}(Y)$ (Y is the isotope we are interested in) from the measured resonance frequency $\nu_{\text{metal}}(^{63}\text{Cu})$ for the ^{63}Cu isotope in metallic copper. Therefore we use the frequency ratio Ξ introduced by Harris et al. [Har08],

$$\Xi(X) = \frac{\nu_{\text{sec. ref.}}(X)}{\nu_{\text{TMS}}(^1\text{H})} \cdot 10^2, \tag{B.2}$$

where $\nu_{\text{sec. ref.}}(X)$ is the frequency of a secondary reference compound for the nuclide X and $\nu_{\text{TMS}}(^1\text{H})$ is the proton resonance frequency in tetramethylsilane at the same magnetic field. $\Xi(^{63}\text{Cu})$ is given in [Har08] for the secondary reference compound $[\text{Cu}(\text{CH}_3\text{CN})_4][\text{ClO}_4]$:

$$\Xi(^{63}\text{Cu}) = 26.515473 \ . \tag{B.3}$$

We compute the secondary reference frequency $\nu_{\text{sec. ref.}}(^{63}\text{Cu})$ in $[\text{Cu}(\text{CH}_3\text{CN})_4][\text{ClO}_4]$ from the measured $\nu_{\text{metal}}(^{63}\text{Cu})$. For this purpose we need the chemical shifts in metallic copper (-3820 [Lut78a]) and $[\text{Cu}(\text{CH}_3\text{CN})_4][\text{ClO}_4]$ (-1820 [Lut78b]). We attain

$$\nu_{\text{sec. ref.}}(^{63}\text{Cu}) = \nu_{\text{metal}}(^{63}\text{Cu}) \ \frac{\delta_{\text{sec. ref.}}(^{63}\text{Cu}) \cdot 10^{-6} + 1}{\delta_{\text{metal}}(^{63}\text{Cu}) \cdot 10^{-6} + 1} = 0.99800761 \ \nu_{\text{metal}}(^{63}\text{Cu}) \ . \tag{B.4}$$

Then $\nu_{\text{TMS}}(^1\text{H})$ is calculated using (B.2), (B.3) and (B.4) as follows:

$$\nu_{\text{TMS}}(^1\text{H}) = \frac{0.99800761 \ \nu_{\text{metal}}(^{63}\text{Cu})}{\Xi(^{63}\text{Cu})} \cdot 10^2 \qquad = 3.76386878 \ \nu_{\text{metal}}(^{63}\text{Cu}) \ . \tag{B.5}$$

Now for the nuclide of interest Y we can obtain the frequency of its secondary reference using (B.2) and (B.5):

$$\nu_{\text{sec. ref.}}(Y) = 0.0376386878 \; \nu_{\text{metal}}(^{63}\text{Cu}) \; \Xi(Y) \; , \tag{B.6}$$

and taking the value of $\Xi(Y)$ from [Har08].

Finally, we can calculate the wanted chemical shift $\delta_{\text{sample}}(Y)$ for the sample under investigation. For this we apply (B.4) to the isotope Y and rearrange it as follows:

$$\delta_{\text{sample}}(Y) = \left[\frac{\nu_{\text{sample}}(Y)}{\nu_{\text{sec. ref.}}(Y)} (\delta_{\text{sec. ref.}}(Y) \cdot 10^{-6} + 1) - 1 \right] \cdot 10^6 \; . \tag{B.7}$$

We substitute $\nu_{\text{sec. ref.}}(Y)$ from (B.6) and eventually obtain the expression (??), where $\nu_{\text{sample}}(Y)$ and $\nu_{\text{metal}}(^{63}\text{Cu})$ are resonance frequencies measured in the same magnetic field, $\Xi(Y)$ is given in [Har08], and $\delta_{\text{sec. ref.}}(Y)$ has to be found in the literature:

$$\delta_{\text{sample}}(Y) = \left[\frac{\nu_{\text{sample}}(Y)}{0.0376386878 \; \nu_{\text{metal}}(^{63}\text{Cu}) \; \Xi(Y)} (\delta_{\text{sec. ref.}}(Y) \cdot 10^{-6} + 1) - 1 \right] \cdot 10^6 \; . \tag{B.8}$$

In the case of $\text{Cu}_x\text{Bi}_2\text{Se}_3$, the isotope of interest is ^{77}Se and we use the reported value for the secondary reference compound $(\text{CH}_3)_2\text{Se}$, also written as Me_2Se, $\Xi(^{77}\text{Se}) = 19.071513$ [Har08]. The chemical shift in Me_2Se $\delta_{\text{Me}_2\text{Se}}(^{77}\text{Se}) = 0.0$ was given by Nakanishi et al. [Nak07].

Appendix C

Studying the origin of Q-factors in Bi_2Se_3 single crystals

All studied samples reduce the quality factor of the NMR probe when being placed in the coil. Remembering the known expression $Q = \omega L/r$, for a fixed angular frequency ω, a change in the quality factor can be due to a change in the induction L of the coil or a changed resistance r. Of course, the coil resistance cannot be influenced by the sample, but the energy losses per cycle can. In order to find the origin of the Q-factor reduction due to the sample, we have performed the following experiment.

First, we measure the resonance frequency and the quality factor of the empty coil in a matched probe, $\omega_{\text{e.c.}}$ and $Q_{\text{e.c.}}$, respectively:

$$\omega_{\text{e.c.}} = \frac{1}{\sqrt{L_{\text{e.c.}}C}} \qquad \text{and} \qquad Q_{\text{e.c.}} = \frac{\omega_{\text{e.c.}}L_{\text{e.c.}}}{r_{\text{e.c.}}}.$$

Keeping the capacity C constant, we then place the sample into the coil and measure a different (non-matched) resonance frequency ω'_{sample}:

$$\omega'_{\text{sample}} = \frac{1}{\sqrt{L_{\text{sample}}C}},$$

and, using the above equations, we are now able to determine the ratio of the inductances of the full and the empty coil:

$$\frac{L_{\text{sample}}}{L_{\text{e.c.}}} = \left(\frac{\omega_{\text{e.c.}}}{\omega'_{\text{sample}}}\right)^2. \tag{C.1}$$

Now we can match the probe and measure the (matched) resonance frequency and the quality factor of the full coil, ω_{sample} and Q_{sample}, respectively. Using that

$$Q_{\text{sample}} = \frac{\omega_{\text{sample}}L_{\text{sample}}}{r_{\text{sample}}}$$

and the ratio from Eq. C.1 we can now calculate the resistance ratio of the full and the

empty coil:

$$\frac{r_{\text{sample}}}{r_{\text{e.c.}}} = \frac{Q_{\text{e.c.}}}{Q_{\text{sample}}} \frac{\omega_{\text{sample}}}{\omega_{\text{e.c.}}} \left(\frac{\omega_{\text{e.c.}}}{\omega'_{\text{sample}}} \right)^2. \tag{C.2}$$

This experiment has been performed for the Bi$_2$Se$_3$ single crystal yielding

$$\frac{L_{\text{Bi}_2\text{Se}_3}}{L_{\text{e.c.}}} = 0.96 \qquad \text{and} \qquad \frac{r_{\text{Bi}_2\text{Se}_3}}{r_{\text{e.c.}}} = 4.7.$$

For comparison, the experiment has been repeated using the same setup and a piece of copper metal as a sample yielding the following results:

$$\frac{L_{\text{Cu}}}{L_{\text{e.c.}}} = 0.81 \qquad \text{and} \qquad \frac{r_{\text{Cu}}}{r_{\text{e.c.}}} = 1.2.$$

Following is a summary of the data.

Measured values for Bi$_2$Se$_3$:

$$\frac{\omega_{\text{e.c.}}}{2\pi} = 100.211\,\text{MHz} \qquad\qquad Q_{\text{e.c.}} = 190$$

$$\frac{\omega'_{\text{Bi}_2\text{Se}_3}}{2\pi} = 100.320\,\text{MHz}$$

$$\frac{\omega_{\text{Bi}_2\text{Se}_3}}{2\pi} = 95.688\,\text{MHz} \qquad\qquad Q_{\text{Bi}_2\text{Se}_3} = 37$$

Measured values for copper:

$$\frac{\omega_{\text{e.c.}}}{2\pi} = 100.270\,\text{MHz} \qquad\qquad Q_{\text{e.c.}} = 190$$

$$\frac{\omega'_{\text{Cu}}}{2\pi} = 111.534\,\text{MHz}$$

$$\frac{\omega_{\text{Cu}}}{2\pi} = 110.616\,\text{MHz} \qquad\qquad Q_{\text{Cu}} = 140$$

Appendix D

Temperature-dependent ^{77}Se NMR spectra

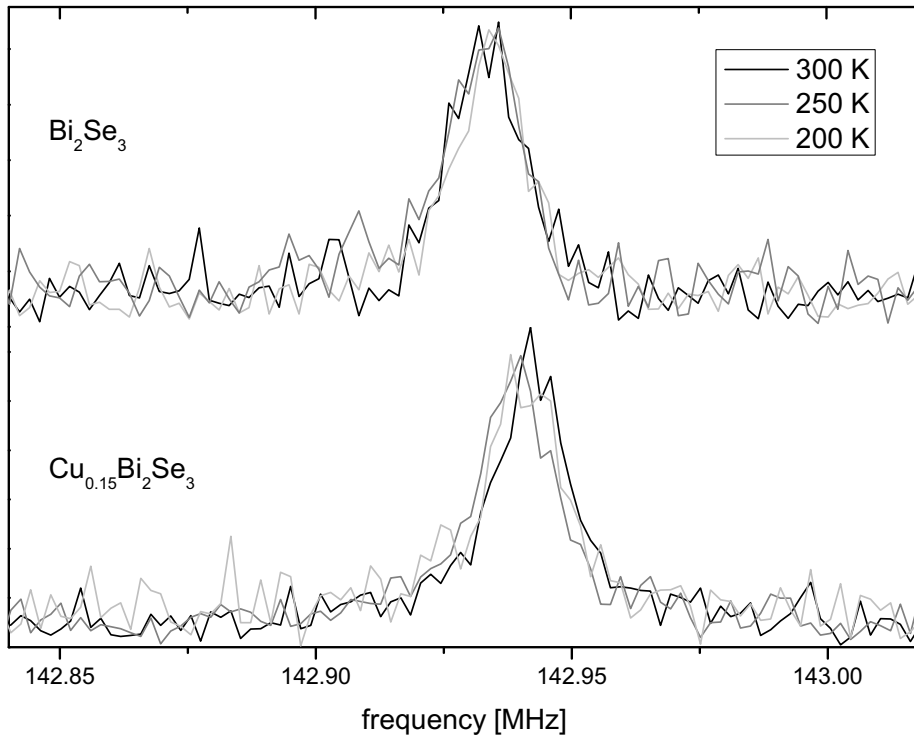**Figure D.1:** ^{77}Se NMR spectra (normalized magnitude) of Bi_2Se_3 and (non-aged) $Cu_{0.15}Bi_2Se_3$ single crystals oriented as $c \parallel B_0$ acquired at 17.6 T and three different temperatures (see legend).

Appendix E

CW EPR of the $Cu_{0.15}Bi_2Se_3$ single crystal

No signals from paramagnetic Cu^{2+} impurities have been found in the continuous wave (CW) electron paramagnetic resonance (EPR) spectrum of the non-aged $Cu_{0.15}Bi_2Se_3$ single crystal, cf. Fig. E.1.
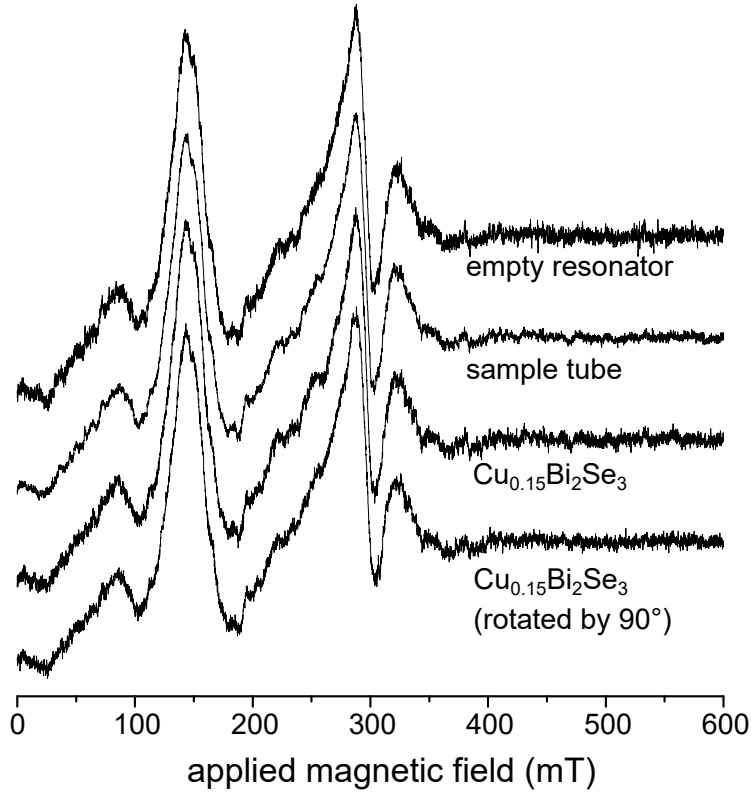

Figure E.1: CW EPR spectra (normalized and baseline corrected) acquired with a conventional Bruker EMX X-band spectrometer at 9.141(02) GHz microwave frequency for (from top to bottom) the empty resonator, an empty sample tube, and a sample tube filled with the (non-aged) $Cu_{0.15}Bi_2Se_3$ single crystal with two orthogonal orientations.

Appendix F

MAS experiment on mortar-ground Bi_2Se_3 powder

Magic angle spinning (MAS) at a spinning rate of 10 kHz leads to no significant narrowing of the Se_{out} powder spectrum of mortar-ground (MG) Bi_2Se_3, and moreover, no appearance of side bands, cf. Fig. F.1. The position of the maximum in the MAS spectrum (~ 235 ppm) agrees well with the isotropic shift of Se_{out} (K_{iso}^{out}), determined from the single crystal data. Hence, the spectral shape changes upon MAS can be explained with the shift anisotropy being averaged out upon spinning.
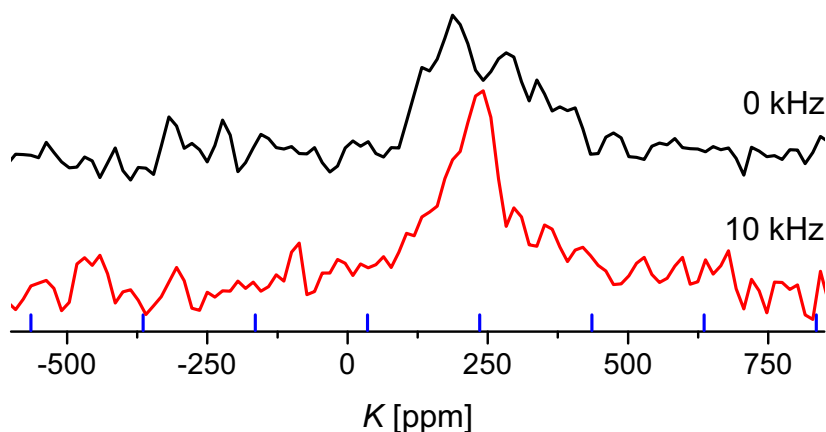

Figure F.1: ^{77}Se NMR spectra of mortar-ground (MG) Bi_2Se_3 powder acquired at ambient conditions and 17.6 T, and at magic angle spinning rates of 0 kHz (static, black solid line) and 10 kHz (red solid line). Blue dashes mark the expected positions of sidebands. Shifts are given with respect to $(CH_3)_2Se$.

Experimental details
The MG Bi_2Se_3 powder was diluted with Al_2O_3 powder (otherwise the rotor was too heavy to spin properly) and measured with a commercial 4-mm MAS probe by Bruker.

Appendix G

Calculation of linewidths due to dipole-dipole coupling

Dipole-dipole coupling leads to line broadening and spin-echo decay. For an NMR line $i = \text{Se}_{\text{in}}/\text{Se}_{\text{out}}$, the dipolar-coupling-induced full width at half maximum $\Lambda_{\text{dip,i}}$ can be computed as

$$\Lambda^i_{\text{dip}} = \frac{\sqrt{\ln 4}}{\pi} \sqrt{\langle \Delta \omega^2 \rangle_i^{\text{unlike}} + \langle \Delta \omega^2 \rangle_i^{\text{like}}} \tag{G.1}$$

and the spin-echo decay constant $T^i_{\text{2G,dip}}$ is given by

$$T^i_{\text{2G,dip}} = \frac{1}{\sqrt{\langle \Delta \omega^2 \rangle_i^{\text{like}}}}. \tag{G.2}$$

Here, $\langle \Delta \omega^2 \rangle_i^{\text{like}}$ and $\langle \Delta \omega^2 \rangle_i^{\text{unlike}}$ are the second moments due to homonuclear and heteronuclear dipolar coupling, respectively, that have been defined in Chap. 3. Here, we repeat the definitions:

$$\langle \Delta \omega^2 \rangle_i^{\text{like}} = \frac{3}{4} \gamma_i^4 \left(\frac{\mu_0}{4\pi} \right)^2 \hbar^2 I_i (I_i + 1) \sum_j \frac{\left(1 - 3\cos^2 \theta_{ij} \right)^2}{r_{ij}^6} \tag{G.3}$$

and

$$\langle \Delta \omega^2 \rangle_i^{\text{unlike}} = \frac{1}{3} \gamma_i^2 \gamma_j^2 \left(\frac{\mu_0}{4\pi} \right)^2 \hbar^2 I_j (I_j + 1) \sum_j \frac{\left(1 - 3\cos^2 \theta_{ij} \right)^2}{r_{ij}^6}. \tag{G.4}$$

The sums in Eqs. G.3 and G.4 have been computed for $0 < r_{ij} \le 40\,\text{Å}$ and with j depending on i and on whether the homonuclear or the heteronuclear case is considered, as follows:

- for $\langle \Delta \omega^2 \rangle_{\text{in/out}}^{\text{like}}$, $j = \text{Se}_{\text{in}}/\text{Se}_{\text{out}}$ and
- for $\langle \Delta \omega^2 \rangle_{\text{in/out}}^{\text{unlike}}$, $j = \text{Se}_{\text{out}}/\text{Se}_{\text{in}}$ or ^{209}Bi.